Model Order Reduction of Wind Farms

Husni Rois Ali

Submitted in partial fulfilment of the requirements for the degree of

Doctor of Philosophy

Imperial College London
Department of Electrical and Electronic Engineering
Control and Power Research Group
September 2019

Dedicated to my family, especially ...

to my parents, Hamtoyo and Nur Widayati;

to my wife, Anisah;

and to our children, Luqman Hakim & Maryam Humaira

Declaration of Originality

I hereby declare that all the work in the thesis is my own. The work of others has been properly acknowledged.

Husni Rois Ali
Department of Electrical and Electronic Engineering
Imperial College London, London, U.K.
September 2019

Declaration of Copyright

Abstract

Despite its rapid increase, large-scale wind farm to grid integration remains a technically challenging issue. A detailed or full order model (FOM) of wind farm plays a key role in understanding this problem and finding appropriate solutions. However, the detailed model is extremely complex and not convenient for large-scale simulation. This thesis aims to develop a simple, accurate, and manageable reduced order model (ROM) of wind farm.

In the first part of the thesis, linear model order reduction (MOR) of wind farm which can capture oscillatory dynamics of FOM during a small disturbance is considered. Effectiveness of five linear MOR techniques, namely balanced truncation (BT), alternating direction implicit (ADI)-based BT, rational Krylov (RK), iterative rational Krylov algorithm (IRKA), and subspace accelerated multi-input multi-output (MIMO) dominant pole (SAMDP) algorithm, are investigated on practical-sized wind farms with 90, 120, and 210 type-3 or doubly-fed induction generators (DFIGs). Merits and demerits of each method are discussed in detail. The ROM of wind farm is validated against the FOM in term of frequency domain indices and waveform agreement at the point of common coupling (PCC). Further, the use of IRKA method is extended to perform MOR of a multi-terminal direct current (MTDC) system connected to two large-scale wind farms with each having 48 DFIGs.

The second part of the thesis presents a method to develop a computationally efficient dynamic model of wind farm suitable for a large disturbance simulation. The method based on a trajectory piecewise linear (TPWL) approximation uses single and multiple training trajectories to develop a nonlinear ROM. Simulation results using a small demonstration wind farm system with 2 DFIGs and a large practical wind farm system with 120 DFIGs are discussed to demonstrate the effectiveness of the model in capturing dynamic behaviour of wind farm following large disturbances.

Acknowledgements

All praise due to *Allah*, the Lord of the worlds, the Most Beneficent and the Most Merciful, for granting me the capability to complete this thesis. During 4 years of this work, I received huge supports and assistances from many people and I want to acknowledge them.

First of all, I would like to express my sincere gratitude to my supervisor Prof. Bikash C. Pal for his continuous advice, guidance, and technical and financial supports throughout my Ph.D. It is a dream come true for me to work under him. He has been an excellent supervisor and at the same time a wonderful person. He gave me freedom to work from home, which allows me to balance academic and family life in particular during the birth of my daughter.

I would like also to thank Dr. Linash Kunjumuhammed, who has been my unofficial second supervisor. I have benefited enormously from his knowledge and willingness to help any time throughout these four years.

I am deeply thankful to my examiners: Prof. Jovica V. Milanovic and Dr. Adriè Junyent-Ferré, for positive suggestions to enhance the quality of this work. I also really appreciate the valuable comments and suggestions from Dr. Imad Jaimoukha in particular during my Early Stage Review and Late State Review. I wish to thank Dr. N. Martins of CEPEL for helping me on the SAMDP method and Dr. Dmitry M Vasilyev of Massachusetts Institute of Technology (MIT) for providing technical discussion on the TPWL method. I really appreciate Dr. Andrzej G. Adamczyk and Dr. Konstantin Vershinin of GE's Grid Solutions for providing technical discussions to improve this work.

I would take this opportunity to thank my colleagues in Control and Power Research Group, who have created supportive environment: Firdous Ul Nazir, Dr. Onyema Nduka, Dr. Bulat Khusainov, Dr. Ankur Majumdar, Dr. Stefanie Kuenzel, Dr. Luxin Zhang, Nicolas Cifuentes, Dr. Abhinav Kumar, Dr. Georgios Anagnostou, Dr. Efstratios Batzelis, Jerome Nsengiyaremye, Dr. Alexandre Moreira, Dr. James Wylie, Dr. Yousef Pipelzadeh, Dr. Hossein Ameli, Nathalie Beaufond, Joan Marc Rodriguez, and Jochen Cremer. I am also grateful to my Indonesian and other reseach fellows at Imperial, and Nansen neighbours.

My most profound gratitude must go to my wife: Anisah, my son: Luqman Hakim, and my daughter: Maryam Humaira, who was born during the last stage of my Ph.D, for their unconditional love, praying, understanding, support and patience. They had to spend majority of their time without me and make invaluable sacrifice for this work. May *Allah* reward them all with something better in return.

I also owe my biggest gratitude to my parents: Hamtoyo and Nur Widayati, my brother: Ibnu Farhatani, my sister: Putri Alya Wulandari, my grandparents: Mr. Mudo Sihono, who passed away during my Ph.D time and Mrs. Mudo Sihono, Mr. and Mrs. Muh Giyanto, and my parents in law: Slamet Suripto and Lina Pariatin. Without their love, praying, and support, I would not have been able to complete my study.

Finally, I acknowledge my full gratitude to LPDP (Indonesia Endowment Fund for Education) for providing my PhD scholarship under grant KEP-161/LPDP/2014.

'...Allah will raise those who have believed among you and those who were given knowledge, by degrees.'

The Quran 58:11

Contents

List of Tables

List of Figures

List of Abbreviations

AC	alternating current.
ADI	alternating direction implicit.
BT	balanced truncation.
CSC	current source converter.
DARMA	deterministic autoregressive moving average.
DC	direct current.
DFIG	doubly-fed induction generator.
DFIGs	doubly-fed induction generators.
ERCOT	Electric Reliability Council of Texas.
FCM	fuzzy C-means.
FDNE	frequency-dependent network equivalent.
FOM	full order model.
GA	genetic algorithm.
GSC	grid side converter.
GTM	geometric template matching.
HSV	Hankel singular values.
HVAC	high voltage alternating current.
HVC	high voltage cable.
HVCs	high voltage cables.
HVDC	high voltage direct current.
IGA	improved genetic algorithm.
IRKA	iterative rational Krylov algorithm.
LCOE	levelized cost of energy.
LVRT	low voltage ride through.
MIMO	multi-input multi-output.
MMC	modular multi-level converter.
MOR	model order reduction.
MSE	mean squared error.
MTDC	multi-terminal direct current.
MVMO	mean variance mapping optimization.
PCC	point of common coupling.
PLL	phase-locked loop.
PMSG	permanent magnet synchronous generator.
PMU	phasor measurement unit.
RK	rational Krylov.
ROM	reduced order model.
ROMs	reduced order models.
RSC	rotor side converter.
SADPA	subspace acceleration dominant poles algorithm.
SAMDP	subspace accelerated MIMO dominant pole.

SCIG	squirrel-cage induction generator.
SCR	short circuit ratio.
SISO	single-input single-output.
SMA	selective modal analysis.
SVC	support vector clustering.
SVD	singular value decomposition.
TPWL	trajectory piecewise linear.
VSC	voltage source converter.
WF	wind farm.
WFT	wind farm transformer.
WTG	wind turbine generator.
WTGs	wind turbine generators.

List of Symbols

α_i	subsystem weights in TPWL method
β	pitch angle of a DFIG in deg.
$\Delta\hat{u}(t)$	$= \hat{u}(t) - \hat{u}(0)$, reduced order input vector centered about $\hat{u}(0)$
$\Delta\hat{x}(t)$	$= \hat{x}(t) - \hat{x}(0)$, reduced order state vector centered about $\hat{x}(0)$
$\Delta\hat{y}(t)$	$= \hat{y}(t) - \hat{y}(0)$, reduced order output vector centered about $\hat{y}(0)$
$\Delta u(t)$	$= u(t) - u(0)$, full order input vector centered about $u(0)$
$\Delta x(t)$	$= x(t) - x(0)$, full order state vector centered about $x(0)$
$\Delta y(t)$	$= y(t) - y(0)$, full order output vector centered about $y(0)$
δ_s	stator or grid voltage angle in rad
δ_{pll}	PLL phase angle in rad
$\hat{A}$	reduced order system matrix
$\hat{B}$	reduced order input matrix
$\hat{C}$	reduced order output matrix
$\hat{D}$	reduced order feedforward matrix
$\hat{G}(s)$	reduced order transfer function
$\hat{m}_i(\sigma)$	i^{th} moment of $\hat{G}(s)$ at σ
$\hat{u}(t)$	reduced order input vector
$\hat{x}(t)$	reduced order state vector
$\hat{y}(t)$	reduced order output vector
$\Lambda(A)$	spectrum of A
λ_{TSR}	tip speed ratio of a DFIG
$\mathcal{K}$	Krylov subspace
$\mathcal{S},\ \mathcal{S}_+,\ \mathcal{S}_-$	Ritz values
ω_r	rotor speed of a DFIG in p.u.
ω_s	synchronous speed in p.u.
ω_t	turbine speed of a DFIG in p.u.
ω_{elB}	electrical speed base in rad/s
ω_{pll}	PLL frequency angle in rad/s
ρ	air density in kg/m^3
σ_i	interpolation points
$\sigma_{H,i}$	Hankel singular values
θ_{tw}	twist angle of drive train of a DFIG in rad
$\tilde{G}(s)$	balanced transfer function
A	full order system matrix
A_{shaded}	area of intersection between downstream turbine and the wake in m^2
A_{turb}	turbine span area in m^2
B	full order input matrix
C	full order output matrix
c	drive train damping coefficient of a DFIG in p.u.$\times$s/el.rad

C_f	filter-side LCL-filter capacitor in p.u.
C_p	turbine performance coefficientof a DFIG
C_Γ	shunt capacitance of Γ-section in p.u.
C_{DC}	capacitance of back-to-back converter in p.u.
C_{dc}	DC-link capacitor of MTDC grid in p.u.
C_{trust}	trust coefficient of a turbine
D	full order feedforward matrix
$D(x)$	wake diameter in m
D_b	$=2 \times R_b$, turbine diameter in m
E	$= [\eta_1, ..., \eta_J]$, ADI shift parameters
$e_s^{'}$	internal voltage of a DFIG in p.u.
$f(\cdot)$	full order nonlinear system equations
$g(\cdot)$	full order nonlinear output equations
$G(s)$	full order transfer matrix
G_i	$\triangleq (A_i,\ B_i,\ C_i,\ D_i)$, linear system corresponding to x_i
H_g	generator inertia of a DFIG in s
H_t	turbine inertia of a DFIG in s
i_c	converter-side LCL-filter inductor current in p.u.
i_f	RL filter current in p.u.
i_g	grid-side LCL-filter inductor current in p.u.
i_L	current through series inductance of Γ-section in p.u.
i_{cc}	DC line current of MTDC grid in p.u.
i_{dc}	DC terminal current of MTDC grid in p.u.
i_s	stator current of a DFIG in p.u.
K	Krylov matrix
k	drive train shaft stiffness of a DFIG in p.u./el.rad
$k_+,\ k_-$	number of Arnoldi iterations
k_d	decay factor of wake model
$L_s^{'}$	$= L_{ss} - L_m K_{mrr}$
L_c	converter-side LCL-filter inductor in p.u.
L_f	RL filter inductor in p.u.
L_g	grid-side LCL-filter inductor in p.u.
l_i	left tangent directions
L_Γ	series inductance of Γ-section in p.u.
L_{dc}	DC cable inductor of MTDC grid in p.u.
$m_i(\sigma)$	i^{th} moment of $G(s)$ at σ
P	controllability Gramian
P_c	GSC active power of a DFIG in p.u.
P_r	rotor active power of a DFIG in p.u.
P_t	turbine power of a DFIG in p.u.
P_{cov}	converter power of MTDC grid in p.u.
P_{dc}	DC power of MTDC grid in p.u.
P_s	stator or grid active power in p.u.
Q	observability Gramian
Q_s	stator or grid reactive power in p.u.
R	Cholesky factors of P
R_1	$R_s + R_2$
R_2	$= K_{mrr}^2 R_r$
R_b	blade length/radius in m
R_c	converter-side LCL-filter resistor in p.u.
R_f	RL filter resistance in p.u.

R_g	grid-side LCL-filter resistor in p.u.
r_i	right tangent directions
R_r	rotor resistance of a DFIG in p.u.
R_s	stator resistance of a DFIG in p.u.
R_{cf}	filter-side LCL-filter resistor in p.u.
R_{dc}	DC cable resistor of MTDC grid in p.u.
T	$= [0\ 1; -1\ 0]$
T_r	L_{rr}/R_r
T_t	turbine power of a DFIG in p.u.
$u(t)$	full order input vector
u_t	wake due to an upstream turbine
u_{tot}	total wake due to multiple turbines
V, W	transformation matrices
v_{dc}^m	DC-link voltage of MTDC grid in p.u.
v_c	GSC voltage in p.u.
v_r	rotor voltage of a DFIG in p.u.
v_s	stator or grid voltage in p.u.
v_w	wind speed in m/s
v_{cf}	filter-side LCL-filter capacitor voltage in p.u.
v_{DC}	DC capacitor voltage of back-to-back converter in p.u.
v_{rec}	receiving-end voltage of Γ-section in p.u.
v_{send}	sending-end voltage of Γ-section in p.u.
v_{wd}	wind speed at downstream turbines in m/s
$x(t)$	full order state vector
$y(t)$	full order output vector
λ_i, x_i^u, y_i^u	eigentriplet of A

Chapter 1

Introduction

1.1 Background and motivation

Driven by economic and environmental concerns, installed capacity of wind turbines has undergone a significant increase worldwide in the last two decades. Starting from only 7.6 GW in 1997, the figure has reached a considerable level of 591 GW by the end of 2018, which accounts for more than twice of the total capacity of the year 2012 (see Fig. 1.1 [1]). Specifically, China shares the highest proportion with 210 GW, which makes up to 36% of total installed capacity worldwide. It is followed by the USA and Germany with 96 GW (16%) and 58 GW (10%), respectively. India, Spain, the UK, and France have a cumulative capacity of 93 GW (15%). This trend is set to continue in the future. In addition, there also has been a rapid progress in the turbine technology in term of size and capacity as revealed in Fig. 1.2 [2]. During the period of 1980-1990, the average wind turbine capacity was merely around 50-500 kW with a diameter of 15-40 meters. Currently, the latest technology of wind turbine has a capacity in the range of 10 MW and a diameter of 190 meters [3]. This has resulted in reduction of levelized cost of energy (LCOE).

Despite this positive trend, integration of large-scale wind farms to grids remains a technically challenging problem. In the USA, the Electric Reliability Council of Texas (ERCOT) system experienced growing sub-synchronous oscillations between a wind farm and a series compensated line at the frequency around 20 Hz in 2009 [4], causing the oscillation current to exceed

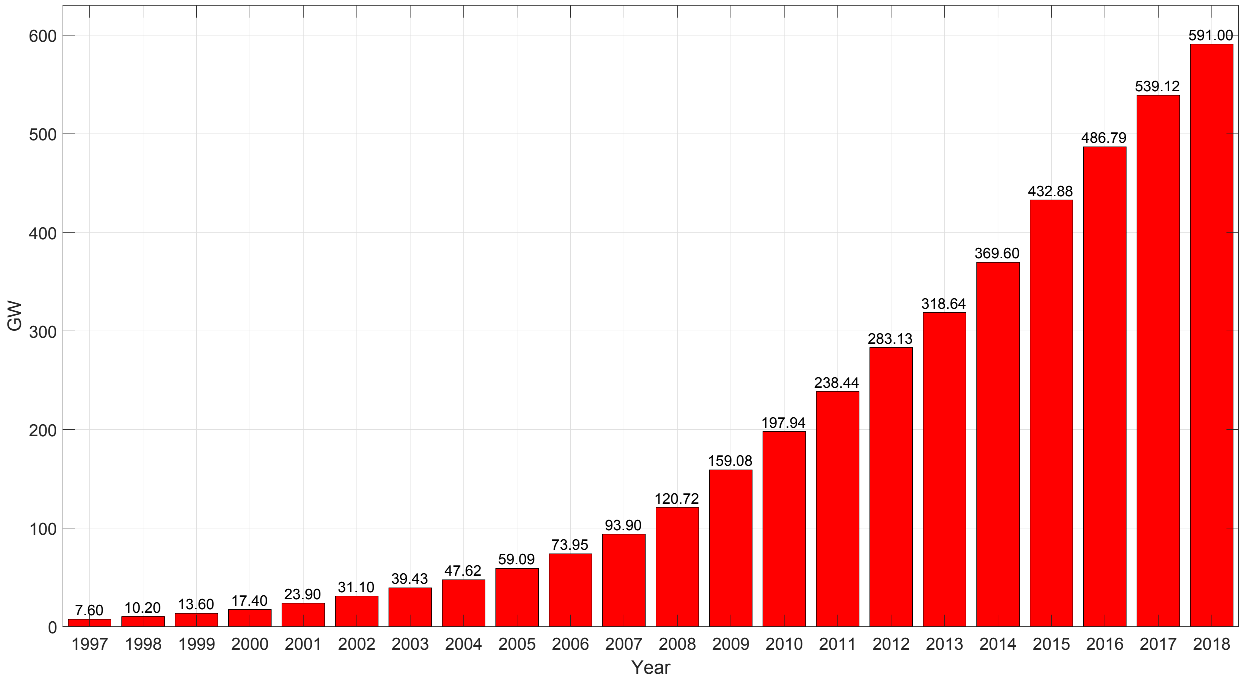

Figure 1.1: Cumulative capacity by December 2018 [1]

4 p.u for 400 milliseconds after a fault occurred. A low frequency interaction for a few seconds at 4 Hz was also reported in the same system by [5] when the short circuit ratio (SCR) was low. In China, a total energy of ten billion kilowatt-hours was unused in 2011 because parts of the grid were too weak for wind farm connection [6], leading to sustained oscillations at 30 Hz for around a second [7]. In Germany, it was reported in [8] that BorWin1, the world first HVDC-based offshore wind farm, experienced harmonic interactions in 2013, leading to shut-down of the HVDC system. The Bard-1 also experienced transmission problems after a couple of unplanned trips occurred in 2014 [9]. Understanding these problems and finding appropriate solutions may necessitate a detailed or full order model (FOM) of wind farm for integration study.

Unlike synchronous machines, the FOM of a typical wind turbine generator (WTG) can be described using about 22 differential equations. Inevitably, representation of a large-scale wind farm with 250 WTGs in power system study requires thousands of differential equations. With the inclusion of collector system dynamics such as cables and transformers, the overall model order grows further up. Hence, this complex representation will pose computational burden for typical power system simulation software, causing stability study of a wind farm connected to a grid virtually infeasible. It is also envisaged that future power systems will be connected to

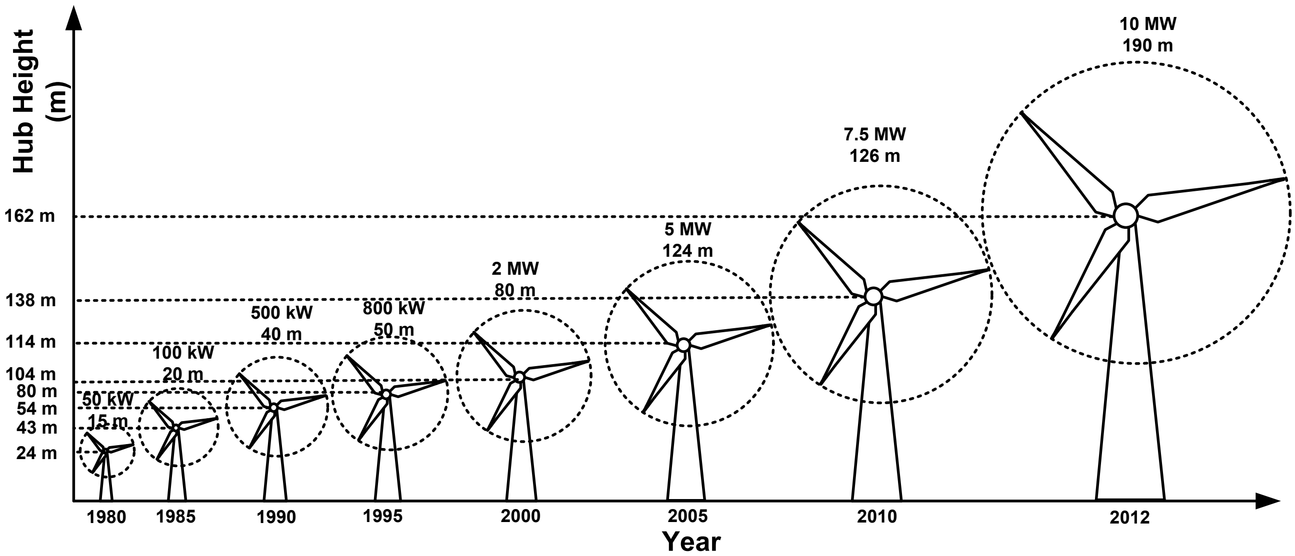

Figure 1.2: Wind turbine technology evolution [2]

multiple wind farms or other asynchronous alternating current (AC) grids to configure a MTDC system, which further exacerbates model complexity and scale, and hence computationally very challenging. In this context, a ROM of wind farm which can capture important dynamics of the FOM is necessary for wind farm integration study. With the ROM, compatibility with the current modelling and analysis framework of power systems where synchronous machines are represented along with network can be maintained, which allows a fast and manageable stability assessment of the whole system through efficient time- and frequency-domain analysis in particular for near real-time applications where only short-time window is available. In addition, reducing dynamic models of complex systems has become an integral part of controller design [10]. Not only does a complex model lead to a complex controller design, but also a high cost and poor reliability controller [11]. This is particularly true when designing the $\mathcal{H}_\infty$ or μ synthesis controllers for example using Youla parameterization approach [12]. Using the low-order wind farm model, a simple controller design can be easily pursued and implemented. For developers and WTG manufacturers, the ROM of wind farm is also useful to demonstrate and validate stability of their system and equipment, while at the same time safeguard their intellectual properties [13].

With regard to the above-mentioned problems, this thesis aims to develop a simple, accurate, and manageable ROM of large-scale wind farm being able to provide a faster assessment of

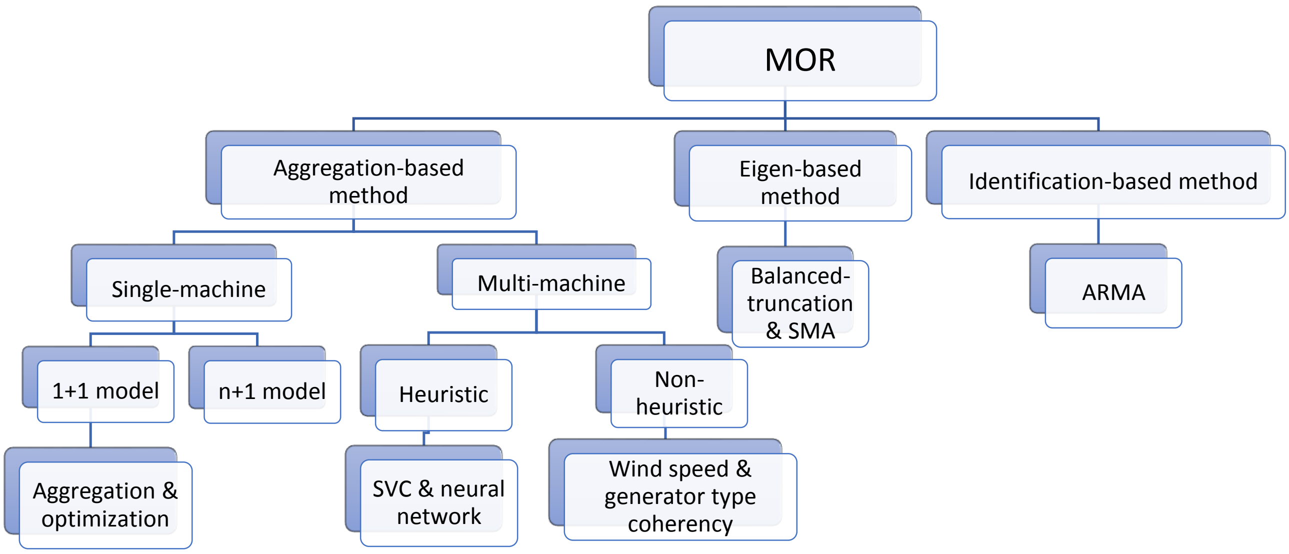

Figure 1.3: Classification of MOR in wind farms

power system stability.

1.2 Brief literature review

A number of methods to obtain model order reduction (MOR) of wind farms have been reported in the literature. According to their characteristics and functional structures, this thesis categorizes the MOR techniques into three general classes, namely aggregation-, eigen-, and identification-based methods. Fig. 1.3 shows the detailed classification.

1.2.1 Aggregation-based method

An early application of aggregation-based method to power systems was introduced to identify and simplify model of a coherent group of synchronous generators. Examples of this include time-response coherency [14] and weak-link coherency [15]. In wind farm study, the aggregation-based method is by far the most popular approach to obtain a simplified model of wind farm. This method can be further divided into a single- and multiple-machine aggregation as indicated in Fig. 1.3. The former assumes that all WTGs within a wind farm operate uniformly

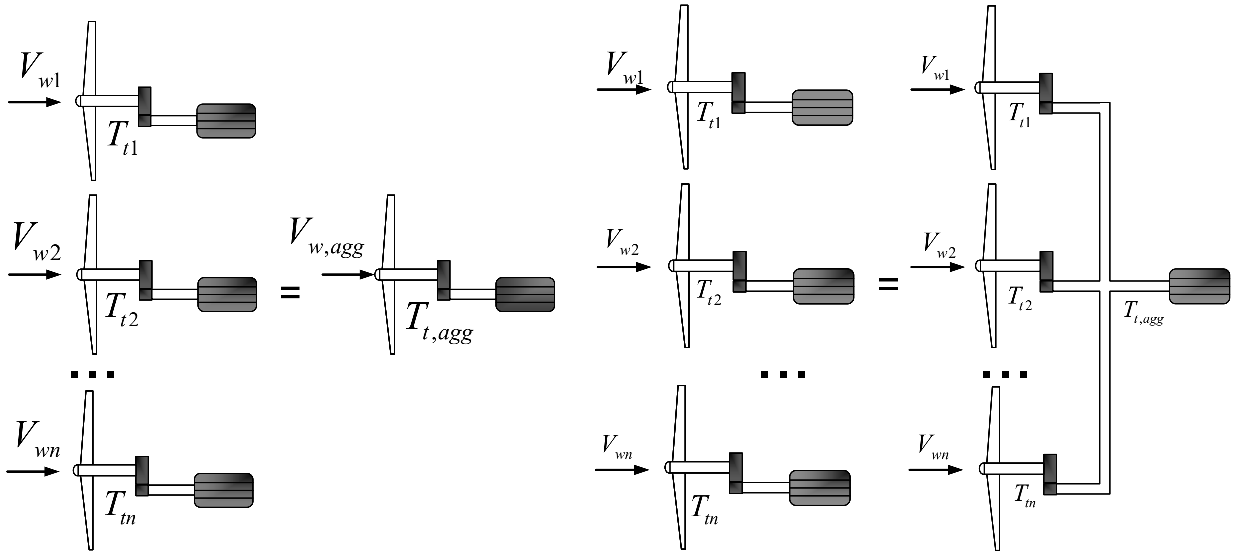

(a) 1+1 model (b) n+1 model

Figure 1.4: Single-machine aggregation

in wind speed and power output terms; thus an aggregated model is sufficient to represent the dynamics of the wind farm. Since a wind farm is normally situated across a very large area, this assumption can be hardly fulfilled, and hence the single-machine aggregation cannot accurately represent the wind farm dynamics [16]. To overcome this problem, the multi-machine representation is used. In this method, the WTGs are grouped according to the similarity of operating condition, which is known as a coherent group. Afterwards, the coherent group of generators is represented with an equivalent model. The subsequent discussion aims to elaborate this classification in more detail.

1.2.1.1 Single-machine aggregation

The single-machine aggregation represents all WTGs within a wind farm using an equivalent generator. This is carried out by a proper scaling up of a WTG capacity proportional to the number of generators in a wind farm. Reference [17] has further classified the single-machine aggregation into a 1+1 and n+1 models. As shown in Fig. 1.4, the former represents a wind farm using a generator driven by an equivalent mechanical system, while in the latter, the wind farm is represented using n mechanical systems driving a generator.

In the 1+1 model, the operating condition of a wind farm determined by the incoming wind speed to all WTGs is assumed to be uniform as such an aggregated generator driven by a turbine is a sufficient representation of wind farm dynamics [18]. Furthermore, the parameters of equivalent WTG can be obtained using two different approaches. First, they are analytically derived from parameters of all WTGs within a wind farm [19–27]. For instance, the converter rating and inertia are scaled up from the corresponding parameters of all WTGs. In [19], an aggregated 1+1 model for constant-speed WTG have been derived for transient stability studies. However, the proposed method has neglected the cable impedance in the collector system, which leads to the ROM valid only for a narrow frequency spectrum between 0.1 to 10 Hz. This work has been extended by Dalia et al. [20, 21] who have proposed wide-band ROMs of wind farms consisting of DFIGs and PMSGs suitable for electromagnetic transient stability studies. The proposed ROMs consist of an equivalent WTG and a frequency-dependent network equivalent (FDNE) element constructed using a vector fitting method to capture the frequency response of passive components within the wind farms. These models have led to a reduction in simulation time by a factor more than 200, while the responses of the FOMs have been accurately reproduced. The difficulty of this approach comes from the implementation of FDNE where the frequency response of the wind farm when all WTGs are disconnected is needed. An aggregation model in the frequency-domain considering spatial factors of wind farm such as wake effect and tower shadow has been established in [22]. The frequency-domain model of wind farm has been obtained by transforming the time-series data of incoming wind speed and output power into frequency-domain using the Fourier transform. Nevertheless, the proposed method assumes that the wind farm is not connected to any power system and simply converts wind energy into electric power. In order to improve the accuracy, Reference [23] has identified that error sources of the 1+1 model mainly come from the discrepancy of the starting recovery power and recovery rates between a wind farm and the 1+1 model. Based on this, an analytical expression to modify rotor side converter (RSC) power command has been derived to enhance the accuracy of ROM. Nonetheless, in order to derive the correction term, responses of all WTGs to a disturbance and their corresponding operating conditions should be known, which are not always practically feasible. Reference [24] has also improved the accuracy of the 1+1 model by introducing a mechanical torque compensating factor (MTCF) which is a scaling factor based on a fuzzy-logic method to adjust the equivalent mechanical torque in the traditional aggregation. The results demonstrated that the MTCF leads to more accurate model outcomes than the conventional 1+1 model by factors of 8.7% and 12.5% for the point of common coupling (PCC) real and reactive power waveforms, respectively, but membership functions for the fuzzy sets requires some trial-and-error process which strongly depends on the operating condition, and hence it can be time-consuming. References [25, 26] have also compared the performance of a 1+1 model to other methods, namely n+1 and multi-machine aggregation, in terms of accuracy and computational complexity. The papers have observed that the 1+1 model has led to a significant reduction in computational time, but the accuracy was lower when the incoming wind speed to all WTGs significantly differed. Further, Perdana et al. [27] have also compared effectiveness of the 1+1 model with actual measurements from a 5 × 600 kW fixed-speed based wind farm. Although the results have shown a high degree of similarity between simulation and measurement, the test has only been performed during a high wind speed condition, where all WTGs within the wind farm are expected to operate uniformly.

The analytical derivation of equivalent parameters of the 1+1 model above strongly depends on the accuracy of individual WTG parameters. Also, it is only applicable to a wind farm with identical WTGs. These assumptions can be hardly fulfilled in practice. In order to resolve these obstacles, the problem of finding the parameters of 1+1 model can also be formulated as an optimization problem [13,28–32]. The common objective is to tune the parameters of the ROM to minimize the waveform discrepancy between FOM and ROM. The real and reactive power, and voltage at the point of common coupling (PCC) are commonly used for the formulation. However, this approach might suffer from excessive computational requirement to solve the optimization problem. In [28], an aggregated model of wind farm with a technology mix of squirrel-cage induction generator (SCIG) and doubly-fed induction generator (DFIG) has been introduced. Using the genetic algorithm (GA), the parameters for 1+1 model have been selected in order to minimize real and reactive power discrepancies at the PCC. It is to be noted that each WTG technology in [28] is represented using a 1+1 model, and hence two 1+1 models are required for a wind farm with a mix of SCIGs and DFIGs. Despite the fact that quite accurate results can be attained, the proposed method only considers steady-state parameters of WTGs, while transient parameters have been excluded from the optimization problem formulation. Parameters of a wind farm with generic model of WTGs have been calibrated using a heuristic technique called mean variance mapping optimization (MVMO) in [29]. The equivalent WTG is represented by two first-order time-delays and a voltage source behind an internal impedance (Thevenin model) controlled by two PI regulators. Using system responses shortly after a disturbance, the MVMO method optimizes these parameters until error of ROM is sufficiently small. In this study, the effectiveness of the proposed method has only been demonstrated on a small-scale wind farm with 18 DFIGs. Due to the fact that the number of parameters involved in the optimization problem can be extremely large, Reference [13] has come up with a concept of trajectory sensitivity to quantify the importance of parameters to the observed waveforms at the PCC. The paper concludes that some parameters do not significantly affect the PCC waveforms, and hence they can be excluded from the optimization variables, leading to a better convergence of the corresponding optimization problem. It has also been shown that different faults often lead to different values of trajectory sensitivity. This result is in line with Wang et al. [30] where an improved genetic algorithm (IGA) has been used to optimize the sensitive parameters of a 1+1 model of a 20×1.5 MW wind farm. In [32], it has been assumed that a phasor measurement unit (PMU) is installed at a WTG bus to measure active and reactive power, and voltage angle and magnitude. Given these measurements, the external system can be reduced using a hybrid simulation technique. The key or sensitive parameters are subsequently identified and optimized using a stochastic optimization method. Nonetheless, the effectiveness of this method is only demonstrated on a wind farm system with 2 WTGs. Note that, in order to use the trajectory sensitivity in these papers, a Jacobian function representing the sensitivity of a certain parameter to wind farm output should be constructed, which can be burdensome. To improve the convergence in finding parameters of a 1+1 model, Zhou et al. [31] have proposed a hybrid improved-particle swarm optimization genetic algorithm (PSO-GA). The paper has also demonstrated the robustness of the proposed ROM under different operating conditions and wake effect, nevertheless computational aspect of the algorithm has not been discussed.

The wind speed across the wind farm is generally different; thus, representation of a wind farm using 1+1 model can create significant errors. In order to enhance the accuracy of ROM, Slootweg et al. [19] have pointed out the importance of representing the mechanical system of a variable-speed WTG individually. The turbine model is initially simplified and the output of mechanical power from all WTGs is then aggregated to drive an equivalent generator. This approach is known as the n+1 model shown in Fig. 1.4b. Although this concept is rather trivial, the implementation in some power system software might not be straight-forward. This approach has been further extended in [33] and [34] by respectively incorporating the pitch controller and two-mass model of drive train dynamics to all WTGs, however this means that the order of aggregated model is still reasonably high. The application of this method on a permanent magnet synchronous generator (PMSG)-based wind farm has been given in [35] for a transient stability study, nevertheless it has only been tested on a small wind farm with 6 WTGs.

1.2.1.2 Multi-machine aggregation

While the operating condition of WTGs within a wind farm may significantly differ, some generators usually exhibit a similar operating condition or operate coherently. In such a case, these coherent generators can be represented using an equivalent WTG as illustrated in Fig. 1.5. Therefore, a key step to this approach is accurate and efficient identification of coherent groups of WTGs. In [36,37], the clusters are found according to wind speed and direction. All possible wind speeds and directions are considered and the influence of wind farm layout and wake effect has been taken into account. Turbines receiving the same incoming wind speed from the same direction are assigned to the same cluster. The effectiveness of this method has been demonstrated on a 80 DFIG-based wind farm. Despite being able to produce accurate responses, the aggregated WTG needs to be recalculated for every possible combination of wind speed and direction, making this approach not practical for power system stability study. An error absolute value of output current between the detailed and aggregated model has been utilized to cluster WTGs in [38]. The aim is to minimize this particular metric, which has been shown in the paper that it is equivalent to clustering the WTGs according to wind speed regions, namely low-, medium-, and high-speed. A very similar clustering approach according to operating regimes of WTGs has been proposed in [39], resulting in a four-machine equivalent model to represent a low voltage ride through (LVRT) behaviour of a wind farm. However, members of a cluster should be updated whenever the operating condition of the wind farms changes. Another important factor to aggregate WTGs is control strategies since they determine the dynamic response of a WTG following disturbances; thus, grouping of variable speed WTGs can be carried out based on them [40]. Nevertheless, the detailed controller structure of a WTG

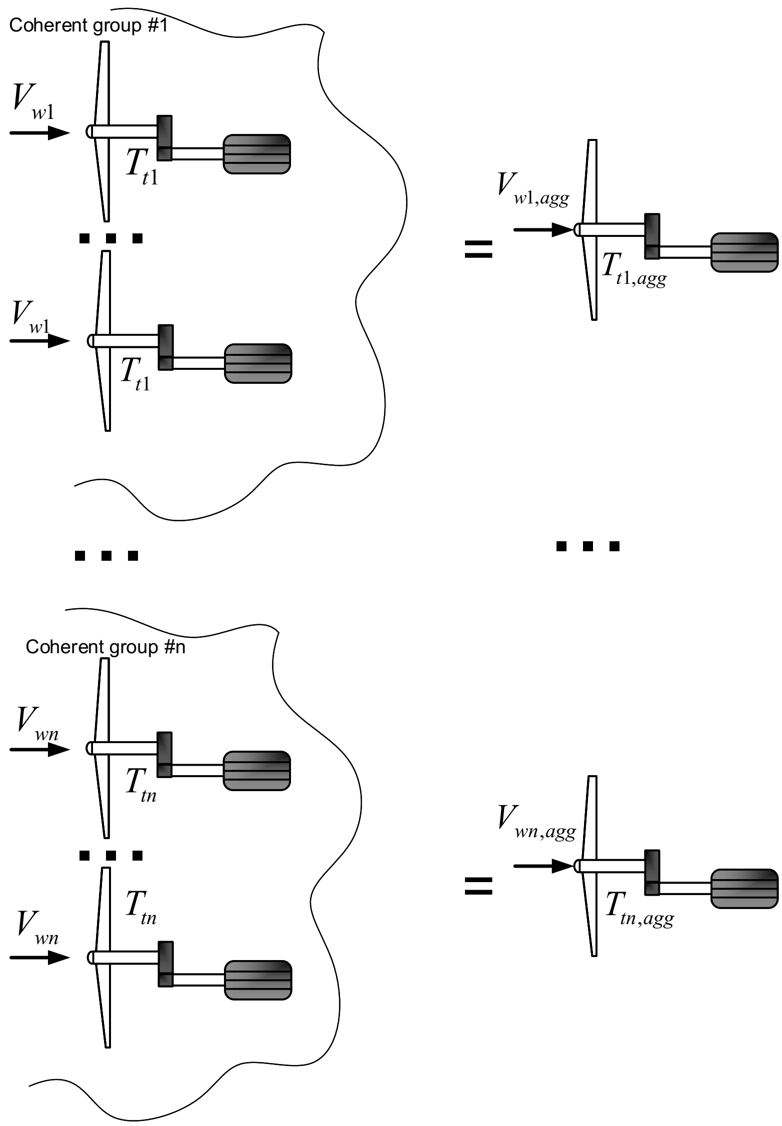

Figure 1.5: Multi-machine aggregation

is often unknown, making this approach difficult to implement in practice.

With the aim to more accurately cluster generators, mathematical tools such as heuristic and spectral methods can be employed. They may, however, suffer from an extensive requirement of training data, which is not always readily available, or expensive computational requirement. In [41, 42], a support vector clustering (SVC) has been used to cluster a wind farm consisting of 49 DFIGs according to wind speed and direction for the whole year. In contrast to [36, 37], here the aggregated WTG is only formed for the most likely coherent group of generators. It, however, requires a further investigation when applied to a wind farm with mixed-type WTGs. In such a case, two different types of WTGs may be clustered into the same group due to receiving the same incoming wind speed and direction, but their dynamic behaviours can be completely different; hence potentially degrades performance of the method. In a variable-speed WTG, wind speed is not the only parameter to characterize its operating condition, and hence Reference [43] has utilized wind speed, slip, q-axis of stator current, and active power to obtain a more accurate clustering of a 16 DFIG-based wind farm using fuzzy C-means (FCM), but these parameters are very difficult to obtain in practice. Teng et al. [44] have used a spanning tree method to cluster a mixed-type wind farm. Although some good results have been demonstrated, computational aspects of the spanning tree method have been mostly overlooked. In order to further enhance accuracy of the multi-machine aggregation, the parameters of each cluster can be found using optimization approach as in the 1+1 model. In [45], the clusters of WTGs are initially found using a geometric template matching (GTM) method. Subsequently, the parameters of each cluster are found using a multi-objective optimization technique. However, the computational burden can scale up easily for a case with a large number of clusters.

1.2.2 Eigen-based method

Unlike the aggregation-based method, the eigen-based method eliminates the need to find a coherent group of generators and relies completely on mathematical techniques [46–54]. In principle, the method identifies important dynamics such as modes strongly participating in the input-output behaviour to be retained in the ROM. On the other hand, less important dynamics can be simplified or even omitted. The main disadvantage of eigen-based method is that it relies on accurate knowledge of a model. If the model is inaccurate, the eigen-based method only reduces order of the inaccurate FOM. The eigen-based method covers a wide range of techniques, such as balanced truncation (BT) and selective modal analysis (SMA); however, its application to obtain MOR of wind farms remains restricted due to for examples expensive computation and stability preservation problems.

Eigen-based method has initially gained attention from researchers to simplify model of large-scale power systems and later been extended to wind farms. Huang et al. [46] have divided a power system into two areas, namely *study-area* and *external-area*. The interaction between these subsystems is represented by voltage and current vectors at the adjacent or partitioned buses. It is always assumed that the main interest is to investigate the *study-area*, hence the MOR is only performed to the *external-area*. The *external-area* is initially linearized and the order is reduced using BT method. The BT method performs a coordinate transformation on the original system and subsequently ranks the states based on their energy through Hankel singular values (HSV). During these processes, two Lyapunov equations need to be solved, which is computationally very expensive for large-scale systems. The states with high energy are preserved in the ROM, while the remaining states can be eliminated. The *study-area*, on the other hand, continues using a nonlinear model. In order to investigate the ROM performance, the two subsystems are reconnected and a fault is performed at the *study-area*. From simulation results, the ROM gives an excellent estimate of FOM responses despite the fact that the order has been reduced to a great extent. The extension of BT method to MOR of wind farms has been given in [51, 52]. The method is successfully able to simplify wind farm models. However, the paper has only considered a simplified model of WTG with a single time-constant to describe input-output behaviour between wind speed and real power, and the computational time of BT method also has not been discussed. With the aim to reduce computational complexity of BT method, a cross-Gramian via a real Schur-form decomposition has been adopted in [49]. In cross-Gramian BT, there is only one Lyapunov equation to be solved and the real Schur-form decomposition allows construction of the ROM without balancing, leading to an overall more efficient process. The performance of this method has demonstrated some satisfactory results such as accurate waveforms and efficient computational time to obtain the ROMs, but dynamics of the collector systems have not been considered. Reference [50] has used a singular perturbation theory in order to perform MOR on a squirrel-cage induction generator (SCIG)-based wind farm. This technique follows the principle of time-scale separation, where the dynamics of a system can often be divided into fast and slow phenomenon. The slow phenomenon is normally related to mechanical variables, such as rotor speed and angle, while the fast phenomenon is related to electric variables, such as voltage and current. In power system stability study, the latter can often be neglected. Nevertheless, instead of fully neglecting the fast phenomenon, its effect can be reintroduced as a correction term, which leads to a static gain correction, and hence improves the performance at low-frequency ranges. The paper, however, has only considered a very simplified model of wind farm with 1 WTG. A selective modal analysis (SMA) has been utilised to perform MOR of a wind farm in [47, 48, 53]. The first step in SMA technique is selecting dominant eigenvalues and state variables of FOM with the help of modal analysis. Using the modal analysis, one can measure the participation of state variables in a mode through participation factor. Next, the SMA retains these dominant modes and state variables in the ROM, whereas less dominant modes and state variables are simplified. However in these papers, only a very simple model of wind farm with 1 WTG has been considered. Applying this method on a large-scale wind farm model is likely to face a tremendous challenge since all eigenvalues of the FOM together with left and right eigenvectors initially are required to be calculated in order to perform modal analysis.

1.2.3 Identification-based method

From the previous discussions, aggregation- and eigen-based methods need accurate knowledge of model and/or parameters to ensure a satisfactory performance of ROMs, which is in general difficult to fulfil in practice. On the other hand, identification-based method offers a new approach where a ROM of wind farm can be developed directly from measurements. While system identification is a matured field, it has only received little attention for simplifying wind farm models. There are several challenges to adopting this method in wind farm application, such as strong nonlinearity and extremely high order of wind farm models, and high degree of uncertainty due to WTG switching.

In [55], the wind farm model valid for the frequency around 2 Hz has been identified using a deterministic autoregressive moving average (DARMA) model. The identification process requires measurements of incoming wind speed to all WTGs, and voltage and power at the PCC. The identified model is recursively updated to follow operating condition of the wind farm. However, the frequency range of the identified model coincides with the electromechanical modes which mostly do not pose a stability problem for wind farms. The measurement is also assumed noiseless in the study. Furthermore, this technique requires data of incoming wind speed to all WTGs within the wind farm, which might not be readily available. In [56], using a Levenberg-Marquardt method, measurements of active and reactive power at PCC following a disturbance have been used to identify parameters of an equivalent model of a wind farm, nonetheless the paper has only considered a very simplistic model of wind farm with 9 WTGs.

1.3 Research objectives

Following the previous discussions on the complexity of wind farm models and state of the art methods to simplify them, this thesis intends to further explore appropriate methodology of reducing high fidelity wind farm models. In particular, the objectives of this research are:

1. To develop a linear ROM of large-scale wind farm which can capture oscillatory dynamics of FOM during a small disturbance.
2. To develop a nonlinear ROM of large-scale wind farm suitable for a transient or large disturbance stability study of power systems.

1.4 Contributions

The contributions of the thesis are summarized as follows:

1. *Improving the understanding of Gramian-based methods to obtain linear ROMs of large-scale wind farms.* Although the BT method has been used in the existing literature to develop low-order models of wind farms, the wind farms are often represented with simple models. Also, the computation complexity of this method has been mostly neglected. In this thesis, the BT method is applied to complex and large-scale models of wind farms. It will be shown that the use of BT method becomes increasingly prohibitive as the size of wind farms increases, which is attributed to solving the Lyapunov equations. To alleviate this problem, an ADI-based BT method is adopted to solve the Lyapunov equations in an iterative manner.
2. *Investigation of the effectiveness of Krylov-based methods to obtain linear low-order models of wind farms.* From the available methods presented in Section 1.2, it is obvious that MOR of wind farms using Krylov-based techniques has not been addressed. These methods offer a very efficient computation process based on Arnoldi or Lanczos iterations suitable to perform MOR on large-scale systems. In particular, this thesis investigates

accuracy and numerical properties of RK and IRKA methods to obtain linear reduced order models (ROMs) of wind farms. The RK method preserves moments of the FOM of wind farm at pre-specified interpolation points which affect both accuracy and stability of the ROM. This becomes increasingly more difficult as the order of wind farm increases. The IRKA methods eases this problem by optimizing the interpolation points to minimize the error between FOM and ROM.

3. *Investigation of the effectiveness of SAMDP method to obtain ROMs of wind farms.* Using SAMDP method, important eigenvalues of FOMs of wind farms are extracted in an iterative manner and preserved in the ROM. The thesis shows that eigenvalue preconditioning is necessary to enhance convergence of the method. Furthermore, it is also found that SAMDP method always leads to a much higher dimension of ROM than those from other methods. A hybrid SAMPD-BT technique is adopted to ease this problem.
4. *Proposing an approach to reduce order of MTDC systems.* The proposed approach uses the IRKA technique to perform MOR of an MTDC system connected to two large-scale wind farms. The model of each wind farm is linearized and subsequently the orders are individually reduced, which makes the proposed approach modular, and thus can be extended to any number of wind farm connections. Different control strategies for the MTDC system are considered to investigate the robustness of the proposed method.
5. *Proposing a method to obtain nonlinear ROMs of wind farms.* The method is based on the TPWL approach which captures nonlinear oscillatory behaviours of wind farms using a weighed combination of linear ROMs. The thesis has established the extent to which the single TPWL-based ROM maintains accurate results. Based on this, an improved multiple TPWL method has been proposed to enhance the accuracy of single TPWL method in a more general scenario.
6. *Developing practical-sized wind farm models and a MTDC system connected large-scale wind farms.* The wind farm models comprising of 90, 120, and 210 WTGs have been modelled in a great detail using Matlab/simulink®. The original wind farm model in [57] has been modified to take into account the dynamics of back-to-back converter, LCL filter, and phase-locked loop (PLL). Incoming wind speed to all WTGs within the wind farms is properly calculated using the wake effect model proposed in [58] to represent a more realistic operating condition of wind farms. Further, a four-terminal MTDC

system connected to two large-scale wind farms with each having 48 WTGs has also been developed. The effectiveness of the above-mentioned methods is demonstrated on these test systems.

1.5 List of publications

During the course of this thesis, the following papers have been written:

1. **H. R. Ali**, L. P. Kunjumuhammed, B. C. Pal, Adamczyk, and K. Vershinin, "Model order reduction of wind farms: Linear approach", *IEEE Transactions on Sustainable Energy*, vol. 10, no. 3, pp. 1194-1205, 2019. DOI: 10.1109/TSTE.2018.2863569.
2. **H. R. Ali**, L. P. Kunjumuhammed, B. C. Pal, Adamczyk, and K. Vershinin, "A Trajectory Piecewise Linear Approach to Nonlinear Model Order Reduction of Wind Farm", *IEEE Transactions on Sustainable Energy*, pp. 1-1, 2019. DOI: 10.1109/TSTE.2019.2912037.
3. **H. R. Ali**, and B. C. Pal, "Model order reduction of multi-terminal direct-current grid systems", invited for the full paper submission on "Special section on Hybrid AC/DC Transmission Grids-TPWRD&TPWRS" to *IEEE Transactions on Power Systems*.
4. **H. R. Ali**, L. P. Kunjumuhammed, B. C. Pal, Adamczyk, and K. Vershinin, "Model order reduction of wind farms: Linear approach", *2019 IEEE Power and Energy Society General Meeting (PES GM)*, Atlanta, GA, pp. 1-1, 2019.

1.6 Thesis outline

Following this introduction, the remainder of the thesis is organized as follows. In **Chapter 2**, models for system used in this thesis, namely wind farm, MTDC, and wake effect, are presented. **Chapter 3** discusses various linear MOR methods of large-scale wind farms, which are valid for a small disturbance. The effectiveness of five different methods, namely BT, ADI-based BT, RK, IRKA, and SADPA, are demonstrated on practical-sized wind farm models. **Chapter 4** extends the use of IRKA method to an MTDC system connected to two large-scale wind farms. Different control strategies for MTDC system are considered to demonstrate the effectiveness of the proposed method. **Chapter 5** presents a method to develop computationally efficient dynamic models of wind farms suitable for a large disturbance simulation using a TPWL approach. Finally, a summary of key findings and list of future work are given in **Chapter 6**.

Chapter 2

System modelling

A typical wind farm is different from conventional power plants in term of construction, size, and operation. It contains tens to hundreds of WTGs and covers a very large geographical area. The capacity ranges from several hundreds MWs up to a GW. A wind farm is always constructed at the best site to effectively harness wind energy, but is often located far away from the main grid. These particular factors lead to the requirement of building network infrastructure for strong integration. Future technology vision also suggests several offshore wind farms will be connected through a MTDC grid. In this context, proper representations of wind farms and MTDC grids are crucial for system stability studies.

This chapter presents a brief introduction to the models of system used in this research. The models rely on the assumption that the power system is balanced. To facilitate the discussion, they are divided into three main categories, namely wind farm, MTDC grid, and wake effect model. The models of wind farms and MTDC grids are given in Section 2.1 and Section 2.2, respectively. Furthermore, to accurately represent a nonuniform operating condition in a wind farm, this chapter presents a wake effect model in Section 2.3, which represents a phenomenon of wind speed drops after passing upstream turbines.

2.1 Wind farm model

2.1.1 Wind turbine generator

The present thesis considers only a DFIG-based WTG. In general, the mathematical model of a DFIG includes dynamic representations of generator, turbine, rotor side converter (RSC) and grid side converter (GSC) controller, back-to-back converter, LCL filter, and phase-locked loop (PLL). The following discussion introduces the detailed models of these components.

2.1.1.1 Generator

The generator model of a DFIG is categorized into electric and mechanical parts. The differential equations governing the electric part in the dq-axis of a synchronous rotating frame are [59]:

$$\frac{L_s^{'}}{\omega_{elB}}\frac{di_s}{dt} = -R_1 i_s + \omega_s L_s^{'} T i_s + \frac{\omega_r e_s^{'}}{\omega_s} + \frac{T e_s^{'}}{\omega_s T_r} - v_s + K_{mrr} v_r \tag{2.1}$$

$$\frac{1}{\omega_s \omega_{elB}}\frac{de_s^{'}}{dt} = R_2 T i_s - \frac{T e_s^{'}}{\omega_s T_r} + (1 - \frac{\omega_r}{\omega_s}) T e_s^{'} - K_{mrr} v_r \tag{2.2}$$

$$i_r = -(\frac{1}{L_m}) T e_s^{'} - K_{mrr} i_s \tag{2.3}$$

where $i_s = [i_{qs}\ i_{ds}]^{'}$, $i_r = [i_{qr}\ i_{dr}]^{'}$, $e_s^{'} = [e_{qs}^{'}\ e_{ds}^{'}]^{'}$, $v_s = [v_{qs}\ v_{ds}]^{'}$, $v_r = [v_{qr}\ v_{dr}]^{'}$, and $T = [0\ \ 1; -1\ \ 0]$. The stator and rotor variables are indicated by subscripts s and r, respectively. i_s and i_r indicate the stator and rotor current, respectively. $e_s^{'}$, v_s, and v_r are the equivalent voltage source behind the transient impedance, terminal voltage, and rotor voltage, respectively. ω_r, ω_s, and ω_{elB} are the rotor, synchronous, and base speeds, i.e. $\omega_{elB} = 2\pi f$, respectively. Other variables are defined as follows:

$$R_1 = R_s + R_2 \tag{2.4}$$

$$R_2 = K_{mrr}^2 R_r \tag{2.5}$$

$$K_{mrr} = \frac{L_m}{L_{rr}} \tag{2.6}$$

$$L_s^{'} = L_{ss} - L_m K_{mrr} \tag{2.7}$$

where R_s and R_r denote the stator and rotor resistance, respectively. L_m, L_{ss} and L_{rr} are the mutual, stator, and rotor inductance, respectively. The q-axis is aligned with the infinite bus voltage with d-axis leading the q-axis by 90° [60].

Furthermore, the mechanical part is modelled using the two-mass model of a drive train to more accurately capture transient behaviour:

$$\frac{d\omega_r}{dt} = \frac{1}{2H_g}(k\theta_{tw} + c\frac{d\theta_{tw}}{dt} - T_e) \tag{2.8}$$

$$\frac{d\omega_t}{dt} = \frac{1}{2H_t}(T_t - k\theta_{tw} - c\frac{d\theta_{tw}}{dt}) \tag{2.9}$$

$$\frac{d\theta_{tw}}{dt} = \omega_{elB}(\omega_t - \omega_r) \tag{2.10}$$

$$T_e = L_m(i_{qs}i_{dr} - i_{ds}i_{qr}) \tag{2.11}$$

where ω_t, and θ_{tw} are the turbine speed and equivalent twist angle of drive train shaft, respectively. T_e and T_m denote the electrical and mechanical torque, respectively. v_s and v_r are the stator and rotor voltage, respectively. c and k respectively indicate the damping and shaft stiffness of the drive train. It is to be noted that a simpler lumped-mass model is sometimes used in the literature.

2.1.1.2 Turbine

A turbine converts the kinetic energy of wind moving at speed v_w into turbine mechanical power P_t or torque T_t. The conversion is described by the following algebraic equations:

$$P_t = 0.5\rho\pi R_b^2 C_p\left(\lambda_{\text{TSR}}, \beta\right) v_w^3 \tag{2.12}$$

$$T_t = P_t/\omega_t \tag{2.13}$$

The symbols ρ and R_b denote the air density and blade length, respectively. $C_p\left(\lambda_{\text{TSR}}, \beta\right)$ is the performance coefficient of a turbine and is a function of the tip speed ratio λ_{TSR} and pitch

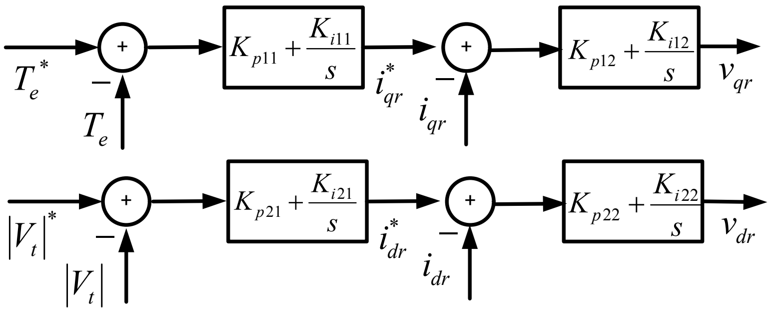

(a) Rotor-side converter controller

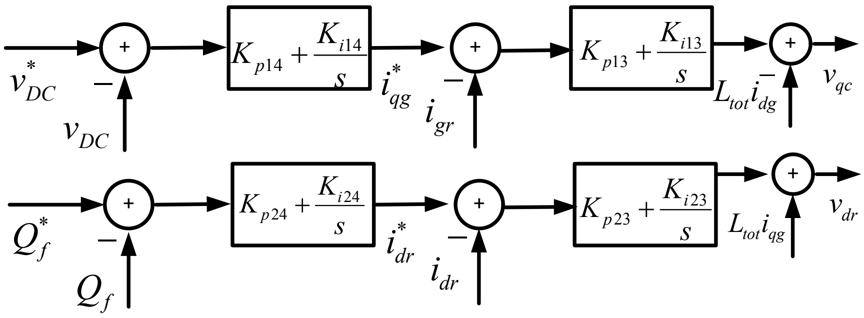

(b) Grid-side converter controller

Figure 2.1: Back-to-back converter controllers

angle β described as follows:

$$\begin{aligned} C_p(\lambda_{\mathrm{TSR}}, \beta) = & c_1(c_2/(\lambda_{\mathrm{TSR}} + c_8\beta) - c_2c_9/(\beta^3+1) \quad - c_3\beta - c_4\beta^{c_5} - c_6) \times \\ & \exp(-c_7/(\lambda_{\mathrm{TSR}} + c_8\beta) \quad + c_7c_9/(\beta^3+1)) + c_{10}\lambda_{\mathrm{TSR}} \end{aligned} \tag{2.14}$$

with $\lambda_{\mathrm{TSR}} = \omega_t R_b / v_w$. $c_1 = 0.5176$, $c_2 = 116$, $c_3 = 0.4$, $c_4 = c_5 = 0$, $c_6 = 5$, $c_7 = 21$, $c_8 = 0.08$, $c_9 = 0.035$, and $c_{10} = 0.0068$ [59].

2.1.1.3 GSC and RSC control model

The GSC and RSC controllers are implemented using a vector control strategy to allow an independent control of active power and torque, and reactive power and terminal voltage of a DFIG. Fig. 2.1 shows the controller implementations of both the RSC and GSC. For the RSC controller, a synchronously reference frame whose the q-axis is aligned with the DFIG terminal voltage v_s is adopted. In this condition, the terminal voltage v_s and torque T_e can be controlled using v_{dr} and v_{qr}, respectively. T_e^* is set to follow the maximum power point curve during sub-rated condition according to [59]:

$$\begin{aligned} T_e^* &= K_{opt}\omega_r^2 \\ K_{opt} &= 0.5\rho\pi R_b^5 C_{pmax}/\lambda_{TSR,opt}^3 \end{aligned} \tag{2.15}$$

where $C_{pmax} = 0.48$ is the maximum value of C_p at $\lambda_{\mathrm{TSR,opt}} = 8.1$ and $\beta = 0$.

Similarly, in the GSC controller, the q-axis of the synchronously rotating frame is aligned with the terminal voltage v_s allowing the DC voltage of a back-to-back converter v_{DC} and GSC reactive power Q_f independently regulated using v_{qc} and v_{dc}, respectively. In this study, the GSC reactive power reference Q_f^* is always set to zero.

2.1.1.4 DC-link capacitor dynamic

A DC-link capacitor is used as a short-term energy storage in a back-to-back converter. Assuming a lossless converter, the capacitor voltage dynamic is governed by the balance between rotor power P_r and GSC power P_c as follows:

$$\frac{dv_{DC}}{dt} = \frac{\omega_{elB}}{C_{DC}}(P_r - P_c) \tag{2.16}$$

where v_{DC} denotes the capacitor voltage and C_{DC} is the back-to-back converter capacitance. During steady-state condition, P_r is equal to P_c, and hence v_{DC} remains constant.

2.1.1.5 LCL filter

An LCL filter is used to reduce voltage ripples and filter out high frequency harmonics due to fast converter switching operations. In a DFIG, it is normally installed between GSC and the grid. Fig. 2.2 illustrates the schematic circuit of the LCL filter whose dynamic model in the

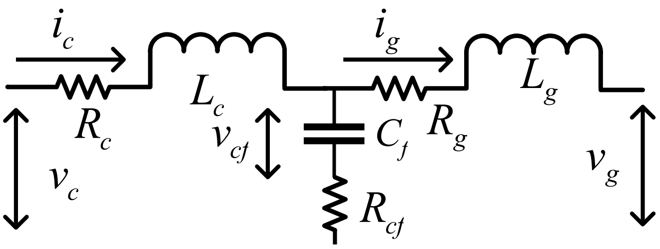

Figure 2.2: LCL filter

dq-axis of a synchronous rotating frame is represented as follows [61]:

$$\frac{L_c}{\omega_{elB}}\frac{di_c}{dt} = v_c - v_{cf} - (R_c + R_{cf})i_c + T\omega_s L_c i_c + R_{cf} i_g \tag{2.17}$$

$$\frac{L_g}{\omega_{elB}}\frac{di_g}{dt} = v_{cf} - v_s - (R_g + R_{cf})i_g + T\omega_s L_g i_g + R_{cf} i_c \tag{2.18}$$

$$\frac{C_f}{\omega_{elB}}\frac{dv_{cf}}{dt} = i_c - i_g - T\omega_s C_f v_{cf} \tag{2.19}$$

where $i_c = [i_{qc}\ \ i_{dc}]'$, $v_c = [v_{qc}\ \ v_{dc}]'$, $v_{cf} = [v_{qf}\ \ v_{df}]'$, $i_g = [i_{qg}\ \ i_{dg}]'$, and $v_s = [v_{qs}\ \ v_{ds}]'$. Subscripts c, s, and cf indicate that corresponding variables and parameters are associated with converter-, grid-, filter-side components, respectively.

2.1.1.6 Phase-locked loop

A phase-locked loop is a device used to synchronize a DFIG with the electrical grid. Here, a simple model of PLL is considered as follows:

$$\begin{aligned} \frac{d\delta_{pll}}{dt} &= \omega_{pll} \\ \omega_{pll} &= (kp_{pll} + \frac{ki_{pll}}{s})(0 - v_{ds}) \end{aligned} \tag{2.20}$$

where δ_{pll} and ω_{pll} are the phase-angle and frequency of v_s detected by the PLL, respectively. kp_{pll} and ki_{pll} represent the proportion and integral constant of PLL controller, respectively.

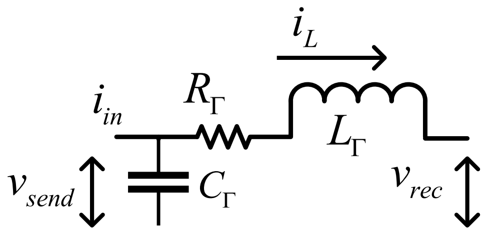

Figure 2.3: Collector systems

2.1.2 Collector systems

The collector system of a wind farm may consist of transformers, cables, and transmission lines. Although these particular components are physically distinctive, in term of mathematical model they can equally be represented as RLC Π-sections. Upon the interconnection, these components can equivalently be considered as many Γ-sections connected in series representing transformers, cables, and transmission lines (see Fig. 2.3) [57]. The vertical element represents the admittance at a sending-end node (C_Γ) and the horizontal section represents the series impedance between sending- and receiving-end nodes (R_Γ and L_Γ). The differential equations governing the Γ-section in the dq-axis of a synchronous rotating frame are given as follows:

$$\begin{aligned}
\frac{L_\Gamma}{\omega_{elB}}\frac{di_L}{dt} &= v_{send} - v_{rec} - R_\Gamma i_L + T\omega_s L_\Gamma i_L \\
\frac{C_\Gamma}{\omega_{elB}}\frac{dv_{send}}{dt} &= i_{in} - i_L - T\omega_s C_\Gamma v_{send}
\end{aligned} \tag{2.21}$$

where $i_{in} = [i_{qin} \quad i_{din}]'$ and $i_L = [i_{qL} \quad i_{dL}]'$ denotes the input current to the Γ-section and the current flowing through the series impedance between two nodes, respectively. $v_{send} = [v_{qsend} \quad i_{dsend}]'$ and $v_{rec} = [v_{qrec} \quad i_{drec}]'$ are the sending-end and receiving-end voltages of the Γ-section, respectively.

2.2 Multi-terminal direct current model

A model of voltage source converter (VSC)-based MTDC grid used in this work is adopted from [62, 63], where the two-level model of converter was used. Although this model is simple, it is commonly used in power system stability studies where converter switching is neglected [64,65]. For other type os study such as harmonic [66], the modular multi-level converter (MMC) is

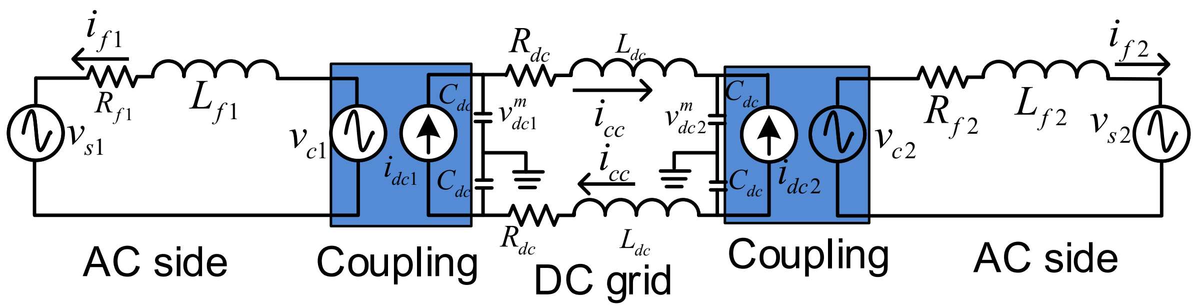

Figure 2.4: Schematic circuit of a VSC with two converters

more preferred.

The schematic circuit of a VSC with two converter terminals is given in Fig. 2.4. As can be noticed, the model of a VSC in general consists of three main parts: alternating current (AC) side model, direct current (DC) grid model, and coupling equations. The AC side model represents dynamic behaviour of RL filters, whereas the DC grid model constitutes dynamic equations of DC-link capacitors and DC cables. The coupling equations, as indicated in the shaded area in Fig. 2.4, represent energy transfer between AC and DC system, and hence ensure a consistent model of AC and DC system.

2.2.1 RL filter

An RL filter connects the converter terminal to the grid and is used to filter out high frequency harmonics. The dynamic equations of this component in the dq-axis of a synchronous rotating frame are given as follows:

$$\begin{aligned}\frac{di_{qf}}{dt} &= \frac{\omega_{elB}}{L_f}(v_{qc} - v_{qs}) + \omega_s i_{fd} - \frac{\omega_{elB} R_f}{L_f} i_{qf} \\ \frac{di_{df}}{dt} &= \frac{\omega_{elB}}{L_f}(v_{dc} - v_{ds}) - \omega_s i_{qf} - \frac{\omega_{elB} R_f}{L_f} i_{df}\end{aligned} \tag{2.22}$$

with ω is the speed of synchronous rotating frame. R_f and L_f are the filter resistance and inductor, respectively. i_f refers to the filter current. v_c and v_s denote the converter and grid voltage, respectively. The subscripts d and q indicate components of variables expressed in the d- and q-axis, respectively.

2.2.2 Direct current grid

The model of a DC grid represents the dynamic equations of DC cables and DC-link voltage. Specifically, the basic equations of the VSC model with two converters as in Fig. 2.4 are as follows:

$$\begin{aligned}\frac{di_{cc}}{dt} &= \frac{\omega_{elB}}{L_{dc}}(v_{dc1}^m - v_{dc2}^m - R_{dc}i_{dc}) \\ \frac{dv_{dc1}^m}{dt} &= \frac{\omega_{elB}}{C_{dc}}(i_{dc1} - i_{cc}) \\ \frac{dv_{dc2}^m}{dt} &= \frac{\omega_{elB}}{C_{dc}}(i_{dc1} + i_{cc})\end{aligned} \tag{2.23}$$

where C_{dc} represents the DC-link capacitor. R_{dc} and L_{dc} are the resistor and inductor of a DC cable, respectively. v_{dc}^m and i_{cc} represent the DC-link voltage and DC line current, respectively. The sign of i_{cc} is assumed to be positive when the current flows from a lower to a higher number of converter, e.g. from converter-1 to -2. It is to be noted that although (2.23) is merely the representation of a VSC with two converter terminals, it can be easily extended to a more general case of multi-terminal VSC model as demonstrated in [62, 63].

2.2.3 Inner-loop control

In order to achieve a decouple control of the RL filter current in (2.22), a vector control strategy using a synchronous rotating frame is adopted. To do this, the speed of the rotating frame ω is obtained from PLL given in Subsection 2.1.1.6, while the q-axis needs to be aligned with the grid voltage v_s. Fig. 2.5 shows the realization of the controller consisting of two parallel proportional and integral (PI) regulators and cross-coupling terms to improve dynamic performances. The physical model shown in Fig. 2.5 represents the dynamic model of the RL filter in (2.22). The current references, i_{qf}^* and i_{df}^*, are obtained from outer-loop controllers which will be discussed in next subsection.

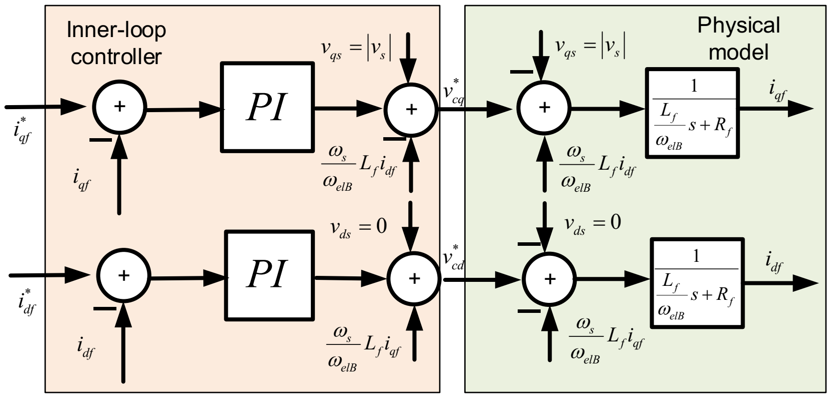

Figure 2.5: Inner-loop controller of VSC

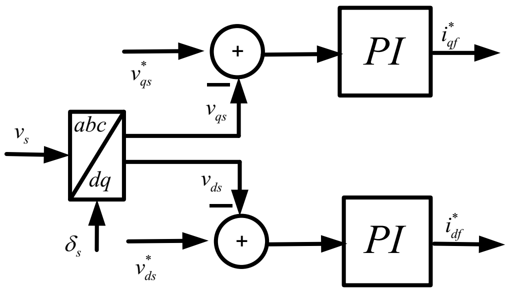

Figure 2.6: Outer-loop controller for offshore converters

2.2.4 Outer-loop control

2.2.4.1 Offshore converter

If a converter is connected to an offshore wind farm, then it should be able to transfer any power generated by the wind farm to the DC grid and at the same time also regulate the offshore grid voltage. In this way, this particular converter acts as an infinite bus for the offshore grid. Realization of the offshore converter controller is given in Fig. 2.6. The voltage references, v_{qs}^* and v_{ds}^*, are obtained from the load flow study and kept constant during the simulation.

2.2.4.2 Slack converter

In an MTDC system, it is common to assign one onshore converter as a slack, which maintains the power balance in the DC grid to regulate the DC voltage. The slack acts like a bi-directional power flow controller being able to export and import power to the DC grid depending on a specific condition. The controller of a slack converter used in this research is given in Fig. 2.7.

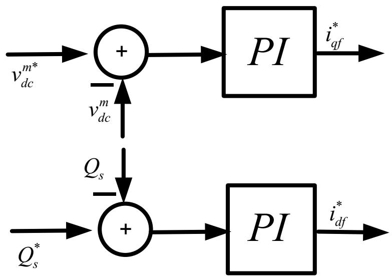

Figure 2.7: Outer-loop controller for slack converter

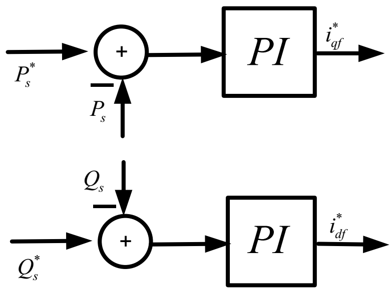

Figure 2.8: Outer-loop controller for onshore converters

It is obvious that i^*_{qf} and i^*_{df} are derived from the measurement of v^m_{dc} and Q_s, respectively.

2.2.4.3 Onshore converter

After assigning an onshore converter as the slack, the rest of onshore converters can perform an independent control of P_s and Q_s by aligning the $q-$ axis of the synchronous rotating frame with the grid voltage v_s. The controller of onshore converters for this purpose is illustrated in Fig. 2.8. The current references i^*_{qf} and i^*_{df} are derived from the measurement of P_s and Q_s, respectively.

2.2.5 Coupling AC and DC system

So far the set of AC and DC equations have been separately presented. The model of AC circuit consists of the RL filter dynamics in Subsections 2.2.1, and the inner and outer-loop controller in Subsection 2.2.3 and 2.2.4, respectively, whereas Subsection 2.2.2 discusses the dynamic model of DC grid. These models need to be coupled in order to have a consistent set of AC and DC equations. The coupling equations represent the shaded area in Fig. 2.4.

Assuming that the power transfer between the AC and DC grid is lossless, i.e. the converter does not dissipate power, the equations of AC and DC system are coupled using:

$$\begin{aligned} P_{dc} &= -P_{cov} \\ 2v_{dc}^{m} i_{dc} &= -(v_{qc} i_{qf} + v_{dc} i_{df}) \\ i_{dc} &= -\frac{(v_{qc} i_{qf} + v_{dc} i_{df})}{2v_{dc}^{m}} \end{aligned} \tag{2.24}$$

where P_{dc} and P_{cov} are the DC and converter power, respectively. i_{dc} denotes the DC terminal current. Furthermore, the $q-$axis component of reference current at the slack bus is obtained using:

$$i_{cq}^{*} = -\frac{(2v_{dc}^{m} i_{dc} + v_{cd} i_{cd})}{v_{cq}} \tag{2.25}$$

Eqn. (2.24) and (2.25) provide a complete link between the AC and DC dynamical system.

2.3 Wake effect model

The dynamic study of a wind farm often relies on the assumption that all WTGs receive identical incoming wind speed. In such a condition, the wind farm is considered to operate at a uniform operating condition, and hence is often represented using an aggregated WTG. Nevertheless this assumption is proven invalid due to the fact that wind speed slows down after passing upstream wind turbines. The turbines extract part of wind kinetic energy, which leads to slowing down the wind speed for downstream turbines. This phenomena is known as wake effect and has a profound influence on the operating condition of a wind farm [67].

In the literature, the wake effect can be modelled using complex calculations of fluid dynamics such as in [68, 69]. Although accurate results can be attained, this particular approach is computationally demanding for power system studies. To ease calculations, a simpler wake effect model proposed by Jensen [58] is adopted in this work. According to this model, the wake shape introduced by an upstream turbine grows in such a way similar to the shape of a cone whose the diameter is calculated according to:

$$D(x) = D_b + 2k_d x \tag{2.26}$$

where $D(x)$ is the wake diameter at a distance x behind an upstream turbine and $D_b = 2 \times R_b$ is the diameter of the turbine, which is equal to 80 m (see (2.12)). k_d denotes the decay factor and is set to 0.0497.

The wake due to the influence of an upstream turbine is therefore given by:

$$u_t = \frac{1 - \sqrt{1 - C_{trust}}}{(1 + (2k_d x/D_b))^2} \tag{2.27}$$

where C_{trust} is the trust coefficient of a turbine which depends on the incoming wind speed to the corresponding turbine v_w. Here, it is approximated using $C_{trust} = (7 \text{ m/s})/v_w$. If a downstream turbine is influenced by multiple wakes produced by several upstream turbines, then the following approach proposed in [70] is considered to calculate the total wake:

$$u_{tot} = \sqrt{\sum \left(\frac{A_{shade}}{A_{turb}} u_t\right)^2} \tag{2.28}$$

where u_{tot} is the total wake effect, A_{shaded} denotes the area of intersection between downstream turbine and the wake, and A_{turb} is the turbine span area, i.e. $A_{turb} = 2\pi R_b^2$.

If the free wind speed entering a wind farm is denoted as v_w, the wind speed at downstream turbines v_{wd} is calculated according to:

$$v_{wd} = v_w - u_{tot} v_w \tag{2.29}$$

Chapter 3

Linear model order reduction of wind farms

This chapter addresses the first objective of the thesis: *To develop a linear ROM of large-scale wind farm which can capture oscillatory dynamics of FOM during a small disturbance.* As previously indicated, the aggregation-based method, namely single- and multi-machine aggregations, is the most widely-used technique to obtain low-order model of wind farms. Despite its popularity in the literature, this method has several obvious weaknesses: 1) a wind farm often operates nonuniformly and hence the single-machine is not satisfactory to capture its dynamics, 2) the operating condition of a wind farm is continuously changing, as a result a coherent group of WTGs in multi-machine aggregation may contain different set of generators, 3) unlike synchronous generators where the concept of coherent group is well defined using the rotor angle, in WTGs, this is difficult due to a weak connection between rotor angle and output power of WTGs.

To address these problems, this chapter demonstrates the application of linear ROM techniques on practical-sized wind farm models [57]. The methods include BT [71], ADI-based BT [72–74], RK [72, 75], IRKA [76, 77] and SAMDP methods [78]. Applicability and effectiveness of these five methods are compared and contrasted. The ROMs are validated by comparing their eigenvalues, bode plots, and dynamic response waveform with those from the FOMs. This chapter is organized as follows. In Section 3.1, discussions on a wind farm model used in this chapter and approach to carry out MOR are given. Section 3.2 provides concise theories of these five methods and their performances to simplify the large-scale wind farm model. The influence of system order on the performances of MOR methods is given in Section 3.3. Finally, the conclusions are drawn in Section 3.4. The results given in this chapter have been published in the IEEE Transactions on Sustainable Energy with the title: *Model order reduction of wind farms: Linear approach* [79].

3.1 Wind farm model and MOR approach

The basic layout of a 120×5 MW wind farm used in this chapter is shown in Fig. 3.1. As indicated, the system is divided into two wind farms, namely Wind Farm 1 and 2. Each wind farm has several strings of WTGs connected to a wind farm transformer (WFT). The WFTs are subsequently connected to a VSC-based high voltage direct current (HVDC) using three high voltage cables (HVCs). Each triangle represents a DFIG-type WTG. The DC-link of the HVDC connecting the wind farm to the main grid is not considered here. The dynamic model of a DFIG is formulated using the 22^{nd} order model as given in Subsection 2.1.1, and the RSC and GSC controllers adopt the vector control strategy given in Subsection 2.1.1.3 to allow a decouple control between active and reactive quantities [61]. Each collector system component is represented using the fourth order Γ-section model in Subsection 2.1.2. Finally, all system parameters are given in Appendix C.

To determine operating condition of the wind farm, the Jensen model discussed in Section 2.3 is used to simulate the wake effect. The inputs for this simulation are the free wind speed and its corresponding direction, while the output is the wind speed profile in the wind farm. Fig. 3.2 shows the geographical distribution of wind turbines within the wind farm to calculate the wake effect. The shape of the wind farm is assumed to be rectangular and the turbines are arranged as such the distances between adjacent turbines are seven times the turbine diameter. In the simulation, only three wind directions, namely 0°, 45°, and 90°, are considered since other wind directions can be easily found by considering the wind farm symmetrical structure. The free wind speed is simulated between 12 m/s and 20 m/s. The results of the simulation are given in Fig. 3.3. As can be clearly seen, the largest wind speed drop occurs between the

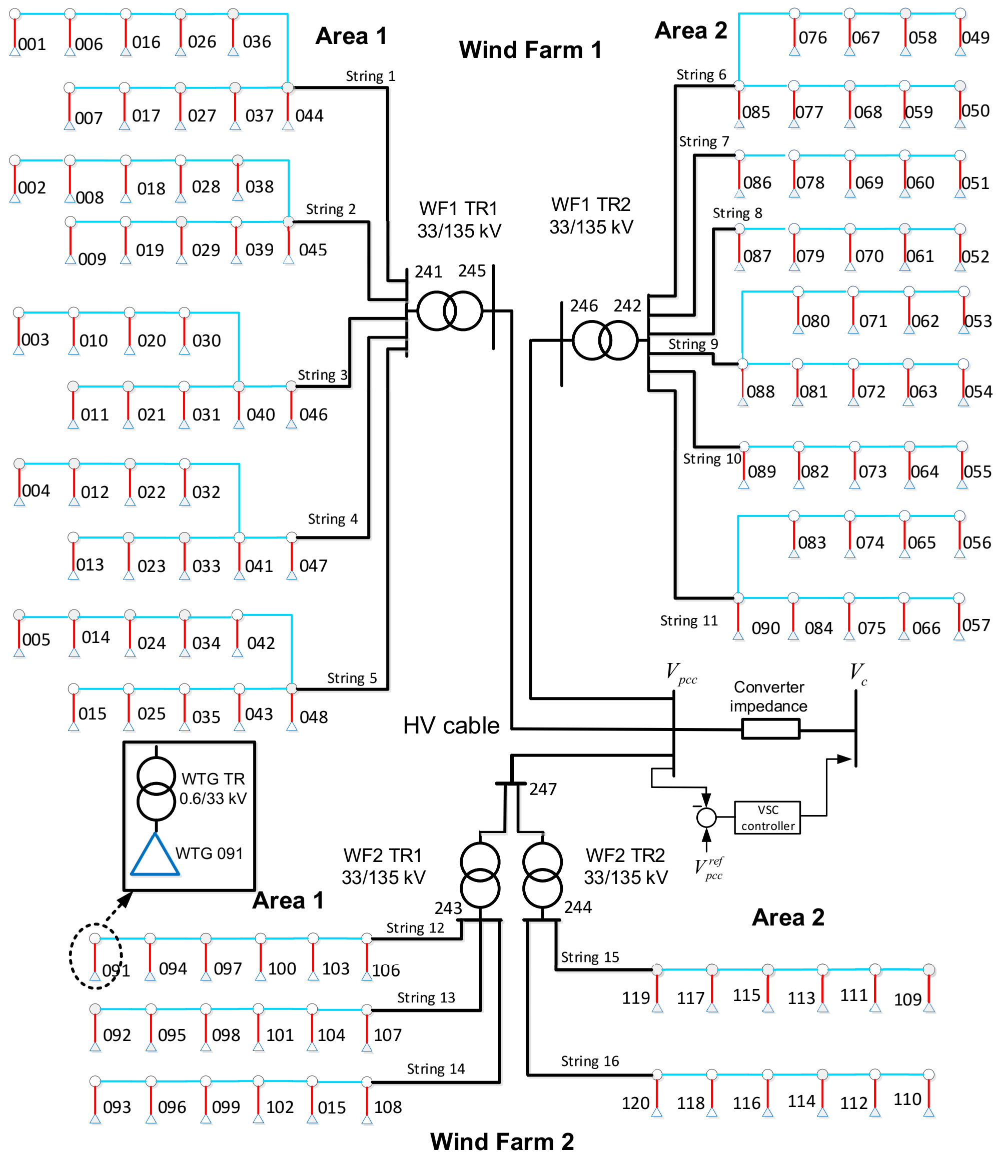

Figure 3.1: Wind farm with 120 DFIGs connected to VSC

first and second row in all cases. After the first two rows, the wind speed drops level off. For further analysis, the condition with free wind speed of 14 m/s and direction of 0° is considered.

Having calculated the wind speed profile, the nonlinear dynamic model of the wind farm is modelled using Matlab/Simulink®. The nonlinear state-space equation for this model can be written as:

$$\begin{aligned} \dot{x}(t) &= f(x(t), u(t)) \\ y(t) &= g(x(t), u(t)) \end{aligned} \tag{3.1}$$

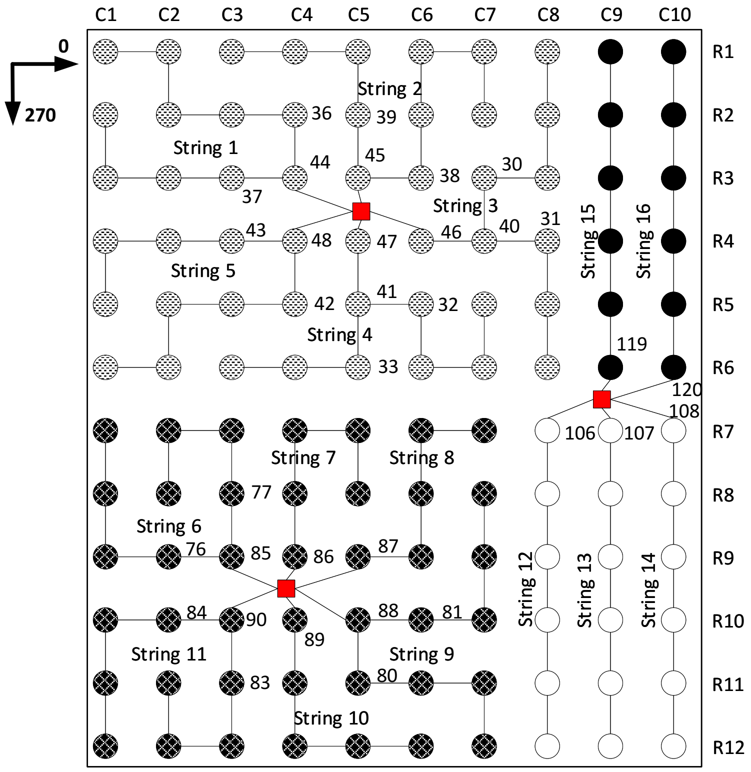

Figure 3.2: Wind farm geographical distribution

where $f(\cdot)$ and $g(\cdot)$ denote the nonlinear system and output equations, respectively. $u(t) \in R^m, x(t) \in R^n$ and $y(t) \in R^k$ are the input, state, and output vectors, respectively. However, the methods presented in this chapter assume that the wind farm model is linear. To obtain a linearized model of the wind farm, numerical linearization using *linearize* command in Matlab® is utilized [80]. It calculates the elements of A_i, B_i, C_i, and D_i by perturbing the states and inputs around an operating condition x_i and u_i according to:

$$
\begin{aligned}
A_i(:,m) &= \frac{f(x(t),u(t))\big|_{\substack{x(t)=xp_i^m \\ u(t)=u_i}} - f(x(t),u(t))\big|_{\substack{x(t)=x_i \\ u(t)=u_i}}}{xp_i^m - x_i} \\
B_i(:,m) &= \frac{f(x(t),u(t))\big|_{\substack{x(t)=x_i \\ u(t)=up_i^m}} - f(x(t),u(t))\big|_{\substack{x(t)=x_i \\ u(t)=u_i}}}{up_i^m - u_i} \\
C_i(:,m) &= \frac{g(x(t),u(t))\big|_{\substack{x(t)=xp_i^m \\ u(t)=u_i}} - g(x(t),u(t))\big|_{\substack{x(t)=x_i \\ u(t)=u_i}}}{xp_i^m - x_i} \\
D_i(:,m) &= \frac{g(x(t),u(t))\big|_{\substack{x(t)=x_i \\ u(t)=up_i^m}} - g(x(t),u(t))\big|_{\substack{x(t)=x_i \\ u(t)=u_i}}}{up_i^m - u_i}
\end{aligned}
\tag{3.2}
$$

where xp_i^m and up_i^m are respectively the state and input vector whose the m^{th} component is

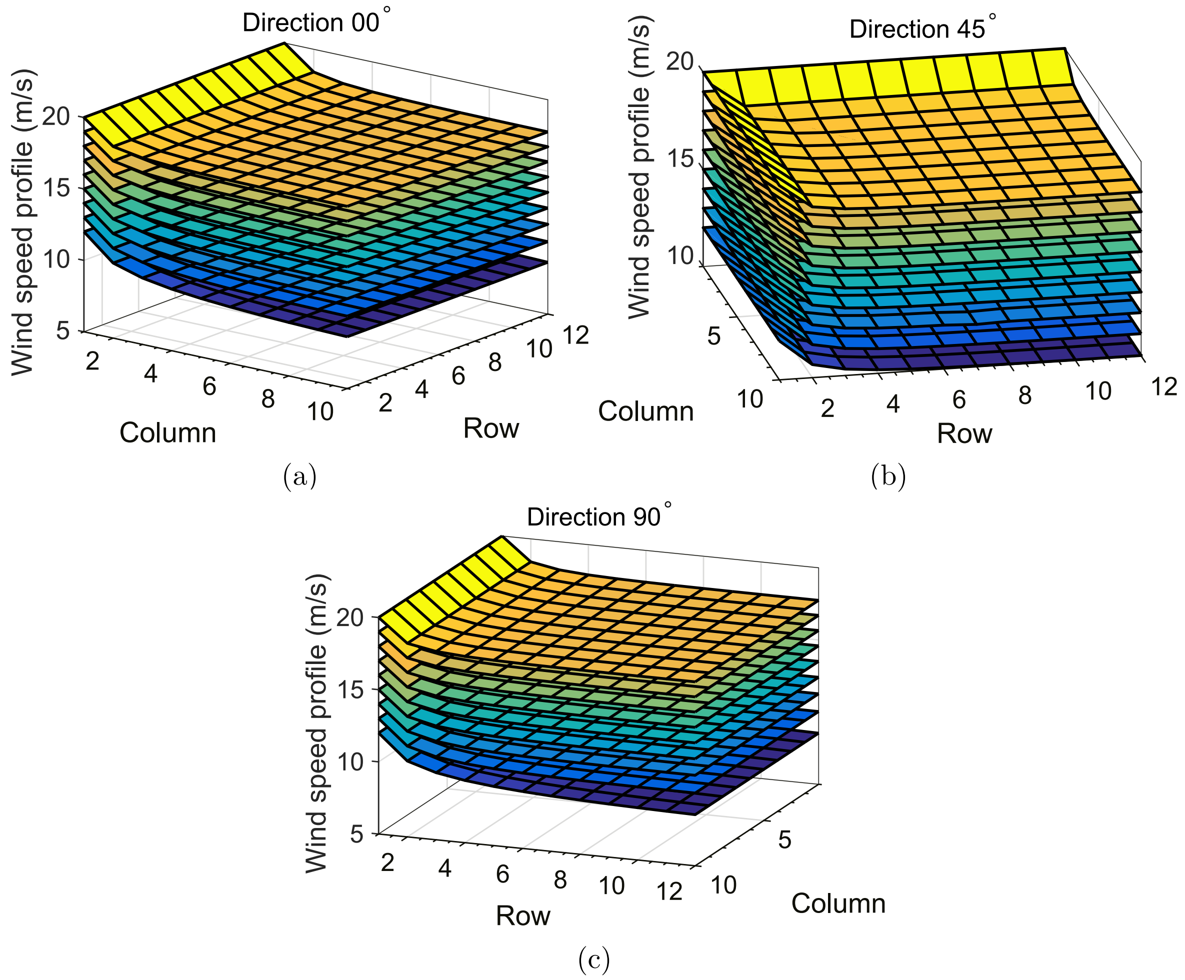

Figure 3.3: Wind speed profile from wake-effect simulation

perturbed from the operating condition. x_i and u_i in this chapter correspond to the stationary operating condition. The perturbations should be sufficiently small such that the system still behaves linearly. Note that (3.2) uses the matrix indexing in Matlab. Analytic linearization is extremely cumbersome to carry out due to the fact that the wind farm model is extremely large.

The above process yields the linearized wind farm model with an order of 3874 whose 1673 eigenvalues are complex conjugate. The frequency of the modes ranges from 1.7 Hz to 3.5×10^4 Hz. The lower frequency modes are related to the DFIG mechanical system, while the higher frequency modes are mostly due to a capacitor-inductor combination in the collector system. The wind farm also contains four critical modes mostly related to collector system components as listed in Table 3.1. Using the $q-$axis of PCC voltage and $d-$axis of converter voltage as the input and output, respectively, these modes are evident as significant peaks in the Bode

Table 3.1: Critical modes of full order system

Mode	Frequency (Hz)	Damping (%)	Dominant states
M1	315	2.9	V_{PCC}, I_{VSC}, V_{HVC}, I_{WFT}
M2	220	5.1	V_{PCC}, I_{VSC}, V_{HVC}, I_{WFT}
M3	49.36	2.6	I_{VSC}
M4	10.33	4.2	I_{VSC}, I_{WFT}, V_{PCC}, VSC controller states

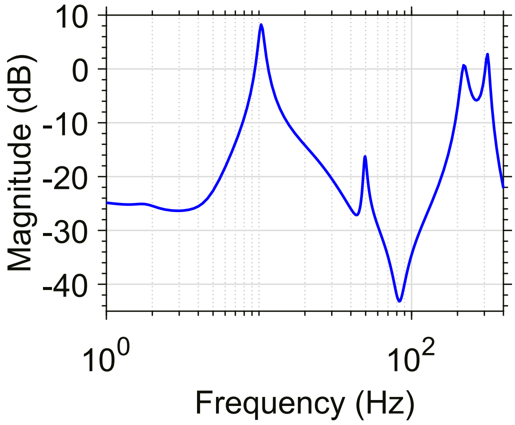

Figure 3.4: Bode magnitude plot for full order model of the wind farm

magnitude plot given in Fig. 3.4. Further, a nonlinear time-domain simulation is also performed by applying a 1% step change in the PCC reference voltage at $t = 0.3$ s. Fig. 3.5 shows the responses of PCC active power and voltage following the disturbance, which are clearly dominated by the critical modes.

To perform MOR, the wind farm system is partitioned into two areas, namely *study-area* and *external-area* as illustrated in Fig. 3.6 [81]. The wind farm with the collector system is considered as the *external-area*, and the *study-area* includes only the dynamic models of VSC controller and impedance. The *external-area* is linearized and subsequently reduced using the five different methods presented in Section 3.2, whereas the *study-area* continues using the nonlinear model. In order to study its accuracy, the ROM of the *external-area* is reconnected to the *study-area*, and this complete system is compared with FOM of the wind farm using the following three criteria:

1. The critical modes or eigenvalues of both systems are compared.
2. The Bode plots of both systems are compared specifically around the frequency of critical modes.

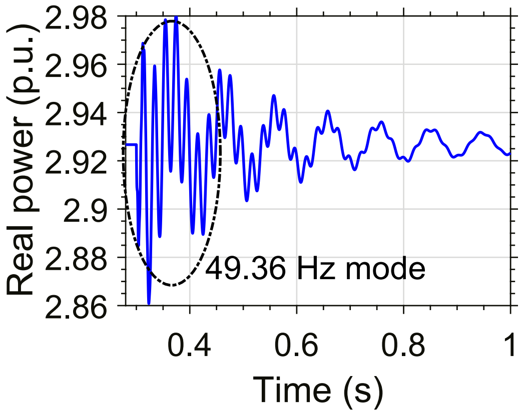

(a) Active power at PCC

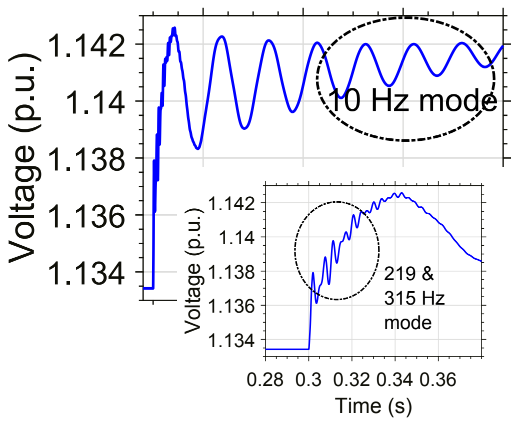

(b) Voltage at PCC

Figure 3.5: Response due to a fault at PCC voltage reference

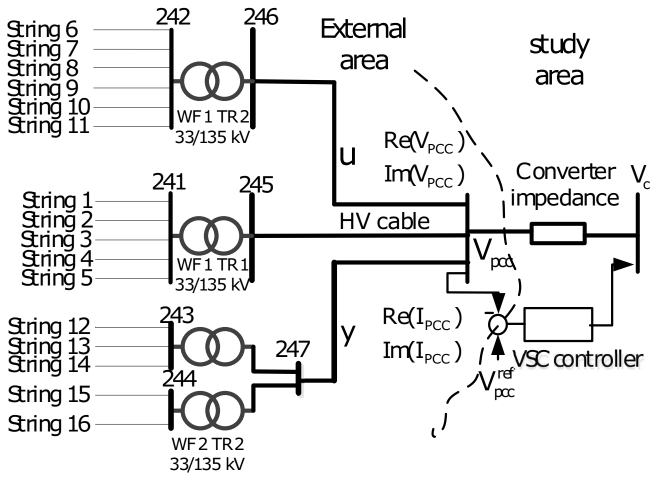

Figure 3.6: Model order reduction approach

3. The PCC power and voltage waveforms of both systems in response to a disturbance are compared using mean squared error (MSE):

$$\text{MSE} = \left(\sum_{n=1}^{N} \sum_{t=1}^{T} (y_{n,t} - \hat{y}_{n,t})^2 / NT \right)^{1/2} \tag{3.3}$$

where y and $\hat{y}$ denote the output of the FOM and ROM, respectively. N is the number of outputs to be compared, and T is the total number of time steps.

3.2 Model order reduction methods

After linearizing the wind farm model at the equilibrium point, namely $x_i = x_0 = x(0)$ and $u_i = u_0 = u(0)$, the state-space representation of the linear system is as follows:

$$\begin{aligned} \Delta\dot{x}(t) &= A\Delta x(t) + B\Delta u(t) \\ \Delta y(t) &= C\Delta x(t) + D\Delta u(t) \end{aligned} \tag{3.4}$$

where $A \in R^{n\times n}$, $B \in R^{n\times m}$, $C \in R^{k\times n}$, and $D \in R^{k\times m}$ are the state, input, output, and feed-forward matrices, respectively, while $x(t) \in R^n, y(t) \in R^k$, and $u(t) \in R^m$ denote state, output, and input vectors, respectively. $\Delta x(t) = x(t) - x(0)$, $\Delta y(t) = y(t) - y(0)$, and $\Delta u(t) = u(t) - u(0)$. For a wind farm system as it will be explained in Subsection 3.2.2, the feed-forward D is always zero for the selected input-output pair. The transfer function of (3.4) can be expressed as:

$$G(s) = \left[\begin{array}{c|c} A & B \\ \hline C & D \end{array}\right] = C(sI - A)^{-1}B + D \tag{3.5}$$

$G(s)$ is controllable if for an initial states $\Delta x(0)$, there is input $\Delta u(t)$ that brings the initial states $\Delta x(0)$ to any final state $\Delta x(t_f)$. This is equivalent to positive definiteness of the controllability Gramian P defined as:

$$P = \int_0^\infty e^{-At}BB^Te^{-A^Tt}dt \tag{3.6}$$

P is the solution to the Lyapunov equation:

$$AP + A^TP = -BB^T \tag{3.7}$$

Further by assuming that $\Delta x(0) = 0$, P can be related to the minimum energy to control states:

$$\|\Delta u(t)\|_2^2 = \Delta x(t_f)^TP^{-1}\Delta x(t_f) \tag{3.8}$$

If the SVD is performed on P, small singular values correspond to the states which are difficult to control.

Likewise, $G(s)$ is observable if given the values of $\Delta u(t)$ and $\Delta y(t)$ for any $t \geq 0$, it is possible to determine a unique initial state $\Delta x(0)$ [82]. This can be checked by using observability Gramian defined as:

$$Q = \int_0^\infty e^{A^T t} C^T C A^{At} dt \tag{3.9}$$

If Q is positive-definite, then the system is observable. Q is the solution to the Lyapunov equation:

$$A^T Q + QA = -C^T C \tag{3.10}$$

It is related to the energy observation of states. Suppose that an autonomous system is released from initial states $\Delta x(0)$, the maximum energy produced by observing $\Delta y(t)$ can be computed using:

$$\|\Delta y(t)\|_2^2 = \Delta x(0)^T Q \Delta x(0) \tag{3.11}$$

If SVD is performed on Q, small singular values are related to the states which are difficult to observe.

To obtain ROM of $G(s)$, the state variables $\Delta x(t) \in R^n$ are projected onto a lower order dimensional subspace R^r with $r << n$. It can be carried out using a transformation matrix $V \in R^{n \times r}$:

$$\Delta x(t) \approx V \Delta \hat{x}(t) \tag{3.12}$$

It is often imposed that the approximation error must be perpendicular to another subspace $W \in R^{n \times r}$, where $W^T V = I_r$. The ROM is obtained by substituting (3.12) into (3.4) and pre-multiplying the result by W^T as follows:

$$\begin{aligned} \Delta \dot{\hat{x}}(t) &= \hat{A} \Delta \hat{x}(t) + \hat{B} \Delta u(t) \\ \Delta y(t) &= \hat{C} \Delta \hat{x}(t) + \hat{D} \Delta u(t) \end{aligned} \tag{3.13}$$

where $\hat{A} = W^T AV$, $\hat{B} = W^T B$, $\hat{C} = CV$, $\hat{D} = D$. In the subsequent subsections, five different methods to obtain $\hat{G}(s)$ from $G(s)$ will be discussed. The methods generally differ on how V and W are actually constructed.

3.2.1 Balanced truncation

As previously stated, the small singular values of P and Q correspond to the states which are difficult to control and observe, respectively. These states do not participate significantly in the input-output behaviour, and as a result they can be eliminated. However, the states which are difficult to observe do not necessarily concur with the states which are difficult to control for most systems [12]. A coordinate transformation thus is required to transform $G(s)$ into $\tilde{G}(s)$ as follows:

$$\tilde{G}(s) = \left[\begin{array}{c|c} \tilde{A} & \tilde{B} \\ \hline \tilde{C} & \tilde{D} \end{array}\right] = \left[\begin{array}{c|c} T^{-1}AT & T^{-1}B \\ \hline CT & D \end{array}\right] \tag{3.14}$$

In this new coordinate system, the controllability and observability Gramian are equivalent as given by:

$$\begin{aligned} &TPT^T = T^{-T}QT^{-1} \\ &\tilde{P} = \tilde{Q} = \Sigma_H = \text{diag}(\sigma_1, \ \cdots \ \sigma_n), \ \sigma_1 \geq \ \cdots \geq \ \sigma_n \end{aligned} \tag{3.15}$$

$\tilde{G}(s)$ is often known as the balanced system. The terms σ_i are known as Hankel singular values (HSV) representing the energy of states. They are normally arranged in descending order. The transformation matrix T and its inverse T^{-1} used in (3.14) are given by:

$$T = R^T U \Sigma^{1/2}, \ T^{-1} = RU\Sigma^{-1/2} \tag{3.16}$$

where R is the Cholesky factor of P and Σ is the singular values of RQR^T given by:

$$P = R^T R, \ RQR^T = U\Sigma^2 U^T \tag{3.17}$$

$\tilde{G}(s)$ can be partitioned according to the partition of Σ_H as follows:

$$\Sigma_H = \left[\begin{array}{c|c} \Sigma_{H1} & \\ \hline & \Sigma_{H2} \end{array}\right] \tag{3.18}$$

where Σ_{H1} represents HSVs with significantly large magnitudes. This partition yields:

$$\tilde{G}(s) = \left[\begin{array}{cc|c} \tilde{A}_{11} & \tilde{A}_{12} & \tilde{B}_1 \\ \tilde{A}_{21} & \tilde{A}_{22} & \tilde{B}_2 \\ \hline \tilde{C}_1 & \tilde{C}_2 & \tilde{D} \end{array}\right] \tag{3.19}$$

The ROM $\hat{G}(s)$ is obtained by preserving sub-matrices in (3.19) as follows:

$$\hat{G}(s) = \left[\begin{array}{c|c} \tilde{A}_{11} & \tilde{B}_1 \\ \hline \tilde{C}_1 & \tilde{D} \end{array}\right] \tag{3.20}$$

It has been shown in [12] that if Σ_{H1} and Σ_{H2} have no common terms or entries, then (3.20) is always stable with the error bound expressed by:

$$\left\|G(s) - \hat{G}(s)\right\|_{\infty} \leq 2(\sigma_{H,r+1}\ \sigma_{H,r+1} \cdots \sigma_{H,n}) \tag{3.21}$$

This is known as *the twice sum of a tail rule* [83], which states that accuracy of the ROM in (3.20) increases when more HSVs are included.

Algorithm 3 in Appendix A illustrates the steps of obtaining a reduced order model using balanced truncation.

3.2.2 Case study using balanced truncation

Prior to reducing the wind farm model using BT method, the *external-area* needs to be linearized with *linearize* command in Matlab/Simulink® as briefly discussed in Section 3.1. This produces a linear system with an order of 3868. Furthermore, it has two inputs ($\mathrm{Vq}_{\mathrm{pcc}}^{\mathrm{ref}}$ and $\mathrm{Vd}_{\mathrm{pcc}}^{\mathrm{ref}}$) and also two outputs ($\mathrm{Iq}_{\mathrm{pcc}}$ and $\mathrm{Id}_{\mathrm{pcc}}$). The *study-area*, by contrast, is retained using the nonlinear model with the opposite variables used as the inputs ($\mathrm{Iq}_{\mathrm{pcc}}$ and $\mathrm{Id}_{\mathrm{pcc}}$) and outputs ($\mathrm{Vq}_{\mathrm{pcc}}^{\mathrm{ref}}$ and $\mathrm{Vd}_{\mathrm{pcc}}^{\mathrm{ref}}$).

The order of reduced model is easily determined through inspection of HSV plot shown in Fig. 3.7. There are significant drops in the magnitudes after the 6$^{\mathrm{th}}$, 18$^{\mathrm{th}}$ and 33$^{\mathrm{rd}}$ HSV, which

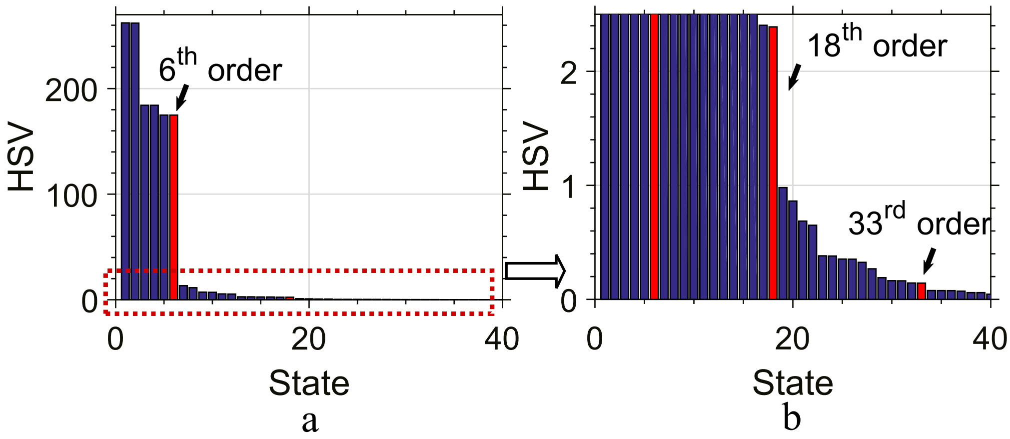

Figure 3.7: a. HSV plot of external area using BT, b. Zoomed version

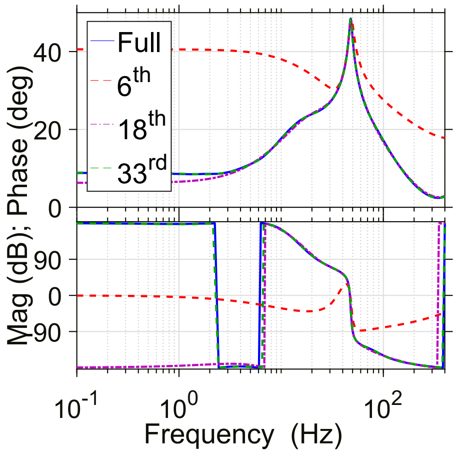

Figure 3.8: Bode plot of *external-area* from $\mathrm{Vq}_{\mathrm{pcc}}^{\mathrm{ref}}$ to $\mathrm{Id}_{\mathrm{pcc}}$: FOM vs. ROM using BT

indicate appropriate orders of the ROMs. The Bode plots from $\mathrm{Vq}_{\mathrm{pcc}}^{\mathrm{ref}}$ to $\mathrm{Id}_{\mathrm{pcc}}$ for these three ROMs are compared with that of the FOM of *external-area* in Fig. 3.8. It is evident that the 6^{th} order system is able to capture the peak at frequency 47.9 Hz, whereas it performs very poorly for other frequency ranges. Increasing order to 18^{th} and further to 33^{rd} can significantly enhance the accuracy of ROM. This observation is consistent with the theory of *the twice sum of the tail rule* of BT method in (3.21).

It is also important to investigate stability preservation of BT method. As previously discussed, the ROM obtained from BT preserves stability of the FOM if Σ_{H1} and Σ_{H2} in (3.18) have no common terms or entries. In other words, the stability is always preserved when the HSVs are distinct. It can be observed that in case of the wind farm model used in this study, the HSVs are always unique. Although Fig. 3.7 shows that some HSVs appear to have the same

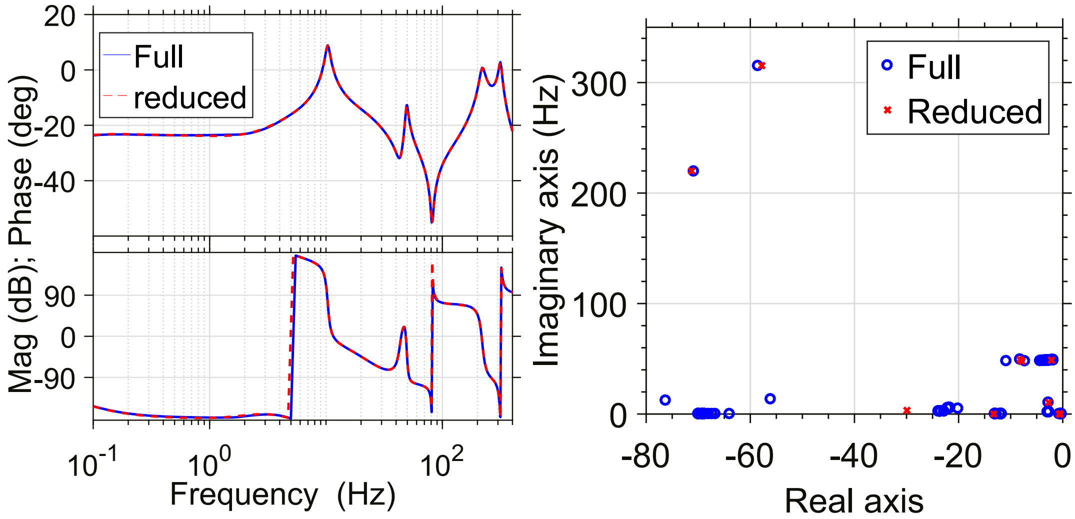

(a) Bode plot from Vd_{pcc}^{ref} to Vq_{pcc} (b) Eigenvalue plot

Figure 3.9: Frequency domain comparison of complete system: FOM vs. ROM using BT

magnitudes, they actually slightly differ. Hence, this makes it possible to always obtain a stable ROM of the wind farm model. This is also supported by a large number of experiments using different orders in which an unstable ROM has never been found. For further analysis, the 33$^{\text{rd}}$ order is selected.

In order to study the complete system, the 33$^{\text{rd}}$ order is reconnected to the *study-area* and the combined system is then compared with the FOM in terms of Bode plot, eigenvalue plot, and waveform agreement. The Bode plots from Vd_{pcc}^{ref} to Vq_{pcc} are given in Fig. 3.9a and it is obvious that they match very accurately over a wide range of frequency. The same information is also conveyed by the eigenvalue plot in Fig. 3.9b in which the four critical modes can be accurately retained in the ROM. Further, multiple modes of the FOM at the frequency close to 50 Hz are replaced with only two modes in the ROM.

To investigate waveform agreement at the PCC, the *study-area* is perturbed with a 1% step change in the PCC reference voltage at t = 0.3 s. The responses of power and voltage from both FOM and ROM are depicted in Fig. 3.10, which indicates the ROM is able to mimic the oscillations of FOM very accurately. The corresponding MSE values of both waveforms given in Table 3.2 also confirm the accuracy of the ROM. Table 3.2 also shows comparison of the elapsed time in order to perform a one-second simulation. As anticipated, for the same duration of simulation, the ROM only requires 0.27 s, while the nonlinear FOM and linear FOM require

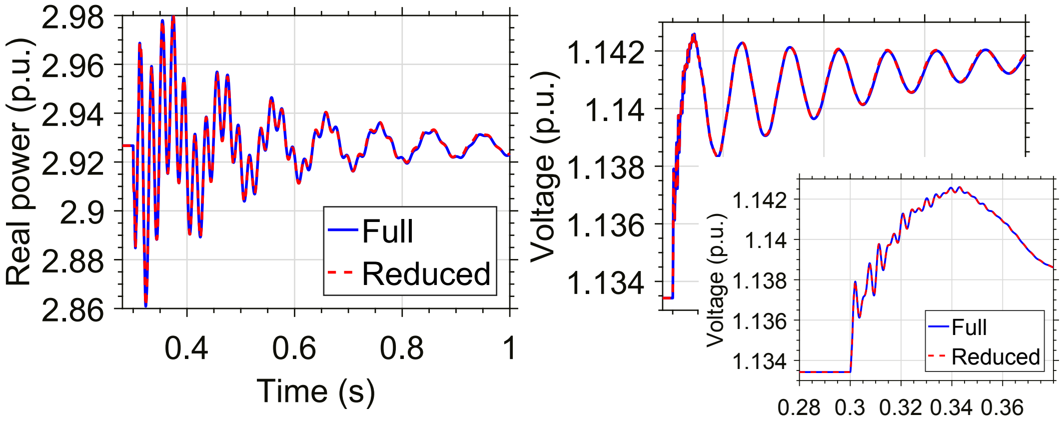

(a) Active power at PCC (b) Voltage at PCC

Figure 3.10: Time domain comparison of complete system: FOM vs. ROM using BT

Table 3.2: Performances of all methods for the wind farm with 120 WTGs

Model	Order	Elapsed time (s)	Extraction time(s)	MSE P_{PCC}	MSE V_{PCC}
Full nonlinear	3874	78.18	-	-	-
Full linear	3874	68.54	-	-	-
BT	39	0.27	433	3.77×10^{-4}	2.96×10^{-5}
ADI	39	0.30	19.18	4.80×10^{-5}	2.05×10^{-6}
RK	42	0.44	0.32	4.30×10^{-3}	9.90×10^{-4}
IRKA	42	0.23	7.41	1.45×10^{-5}	1.52×10^{-5}
SAMDP	307	5.10	31.17	2.42×10^{-4}	1.61×10^{-5}
Hybrid	46	0.52	38.98	3.10×10^{-4}	2.20×10^{-5}

78.18 s and 68.54 s, respectively.

Despite the excellent performance, solving the Lyapunov equations in the BT proves computationally prohibitive for the large-scale wind farm model. More specially, this computational cost is even more expensive than simulating the FOM for one second as given in Table 3.2. This demonstrates that a special method is required to solve the Lyapunov equation more efficiently, enabling extension of BT method to the high order model of wind farm.

3.2.3 Alternating directions implicit based balanced truncation

The BT method presented in the previous section has been widely used for reducing orders of dynamic systems. Unfortunately, as presented in Subsection 3.2.2, its application is not wellsuited for large-scale systems due to the fact that the costs of solving two Lyapunov equations in (3.7) and (3.10) are prohibitive. To deal with this problem, an ADI-based algorithm is adopted to perform an iterative procedure to solve the Lyapunov equation, and hence allows extension of BT method to large-scale wind farm models.

The ADI iteration was originally used to solve a system of linear equations as demonstrated in Appendix B. Notice that (B.3) can directly be applied to the Lyapunov equations in (3.7) and (3.10). Since these equations are dual, it will only be illustrated for (3.7). Using (B.3), the ADI iterative procedure for (3.7) is given as follows:

$$\begin{aligned} (A+\eta_i I_n)P_{i-\frac{1}{2}} &= -P_{i-1}(A^T-\eta_i I_n) - BB^T \\ (A+\eta_i I_n)P_i^T &= -P_{i-\frac{1}{2}}^T(A^T-\eta_i I_n) - BB^T \end{aligned} \tag{3.22}$$

η_i denotes the shift parameters. Combining both equations above into a single equation yields:

$$\begin{aligned} P_i = & (A+\eta_i I_n)^{-1}(A-\bar{\eta}_i I_n)P_{i-1}(A-\bar{\eta}_i I_n)^T(A+\eta_i I_n)^{-T} \\ & - 2\mathrm{Re}(\eta_i)(A+\eta_i I_n)^{-1}BB^T(A+\eta_i I_n)^{-T} \end{aligned} \tag{3.23}$$

Using (3.23) with the proper shift parameters η_i, P can be found efficiently. Further, realizing the fact that in BT method, the aim is not to directly calculate P, but rather the Cholesky factor of it, i.e. R as in (3.17), it is possible to modify (3.23) to directly calculate R [84, 85]. Assuming that $R_0 = 0$ and $R_i R_i^T = P_i$, then (3.23) can be rewritten as:

$$\begin{aligned} R_1 =& \sqrt{-2\mathrm{Re}(\eta_1)}(A+\eta_1 I_n)^{-1}B \\ R_i =& \Big[\sqrt{-2\mathrm{Re}(\eta_1)}(A+\eta_1 I_n)^{-1}B,\ (A+\eta_i I_n)^{-1}(A-\bar{\eta}_i I_n)R_{i-1}\Big] \end{aligned} \tag{3.24}$$

The shift parameters used in (3.22)-(3.24) are obtained from the solution of the following min-max problem:

$$E = [\eta_1, ..., \eta_J] = \underset{\substack{\eta_i \in \mathbb{C}_-, \\ i=1,...,J}}{\arg\min} \left(\max_{\lambda \in \Lambda(A)} \left| \prod_{i=1}^{J} \frac{\lambda - \bar{\eta}_i}{\lambda + \eta_i} \right| \right) \tag{3.25}$$

Several methods have been proposed to solve (3.25) [84–87]. The main challenge is to calculate the spectrum of A, i.e. $\Lambda(A)$, as for a large system calculating it is computationally expensive. This thesis uses a heuristic approach proposed in [86] which calculates the suboptimum ADI shift parameters $E = [\eta_1, ..., \eta_J]$ in (3.25). In this method, $\Lambda(A)$ is approximated by Ritz values $\mathcal{S}$ obtained using two Arnoldi iterations. The eigenvalues with large magnitudes $\mathcal{S}_+$ are approximated by running the Arnoldi process on A for k_+ iterations, while the approximation of eigenvalues with small magnitudes $\mathcal{S}_-$, i.e. near the origin, is carried out by running the Arnoldi process on A^{-1} for k_- iterations, and then calculating the inverse $1/\mathcal{S}_-$. The final approximation is the union from these two processes: $\mathcal{S} = \mathcal{S}_+ \cup 1/\mathcal{S}_-$ for $\mathcal{S} \in \mathbb{C}_-$. Following this, the suboptimum ADI shift parameters $E = [\eta_1, ..., \eta_J]$ are selected from elements of $\mathcal{S}$ based on the following steps. The first element of E is assigned from $\eta_i \in S$ which minimizes (3.25) over S. There are two possibilities, namely $E = \{\eta_i\}$ for real case or $E = \{\eta_i \; \bar{\eta}_i\}$ for complex case. More elements of $\mathcal{S}$ for which the maximum of the current (3.25) is reached are successfully added to E. In this respect, the suboptimum solution of (3.25) is found heuristically [85].

A complete procedure to obtain ROM of a wind farm using ADI-based BT technique is illustrated by Algorithm 4 in Appendix A.

3.2.4 Case study using alternating directions implicit

As previously discussed, the bottleneck of solving the Lyapunov equations in BT method can be overcome by using ADI iteration. Prior to executing the ADI iterative procedure, a set of shift parameters need to be carefully selected to ensure a satisfactory performance. In this work, the heuristic approach proposed in [86] is adopted due to its simplicity. Matlab implementation of the method is also provided in [88].

The first step to obtain the shift parameters is to calculate $\Lambda(A)$. Because calculating $\Lambda(A)$ is computationally prohibitive for large systems, it is estimated by Ritz values $\mathcal{S}$ obtained using the Arnoldi iterations as explained earlier. For the wind farm model in Fig. 3.1, the spectrum with large magnitudes $\mathcal{S}_+$ is determined by performing Arnoldi on A for $k_+ = 100$ iterations. Likewise, the spectrum with small magnitudes $\mathcal{S}_-$ is calculated by also running the same algorithm on A^{-1} for $k_- = 50$ iterations and then calculating inverse of the result, i.e. $1/\mathcal{S}_-$. The final spectrum $\mathcal{S}$ is the union of the results from these two processes, but only the values with negative real parts are chosen, i.e. $\mathcal{S} = \mathcal{S}_+ \cup 1/\mathcal{S}_-$ for $\mathcal{S} \in \mathbb{C}_-$. Finally, the supoptimum ADI shift parameters $E = [\eta_1, ..., \eta_J]$ are selected from $\mathcal{S}$ by solving (3.25)

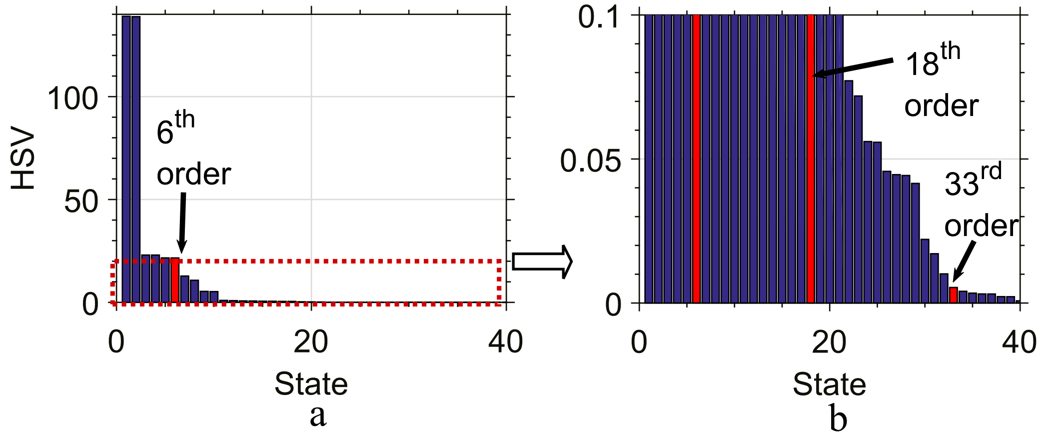

Figure 3.11: a. HSV plot of external area using ADI, b. Zoomed version

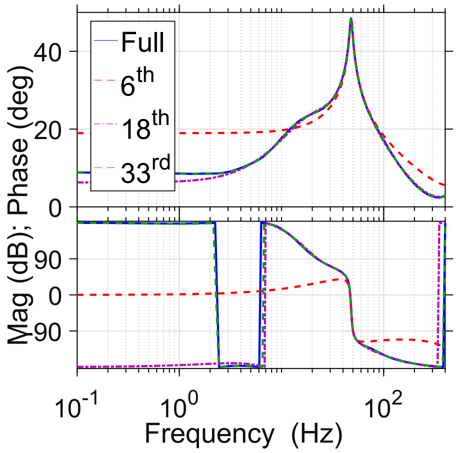

Figure 3.12: Bode plot of *external-area* from Vq_{pcc}^{ref} to Id_{pcc}: FOM vs. ROM using ADI

heuristically. The number of shift parameters J is set to 40.

Having obtained the shift parameters, the ADI algorithm is run for 500 iterations. Since there are fewer number of shift parameters than the number of iterations, the shift parameters are used in a cycle. The estimated HSV of the *external-area* is given in Fig. 3.11. Although the magnitude is different from the exact HSV in Fig. 3.7, the same orders as in the case of BT method, namely 6, 18, and 33, are selected for the sake of a fair comparison. The corresponding HSV are indicated in Fig. 3.11. The Bode plots from Vq_{pcc}^{ref} to Id_{pcc} for these three ROMs are compared with that of the FOM of *external-area* in Fig. 3.12. The 6^{th} order system is only able to capture the peak of full order system at frequency of 47.9 Hz. By increasing the order to 18 and 33, a more accurate result can be attained. The 33^{rd} ROM is reconnected to the *study-area* for further analysis.

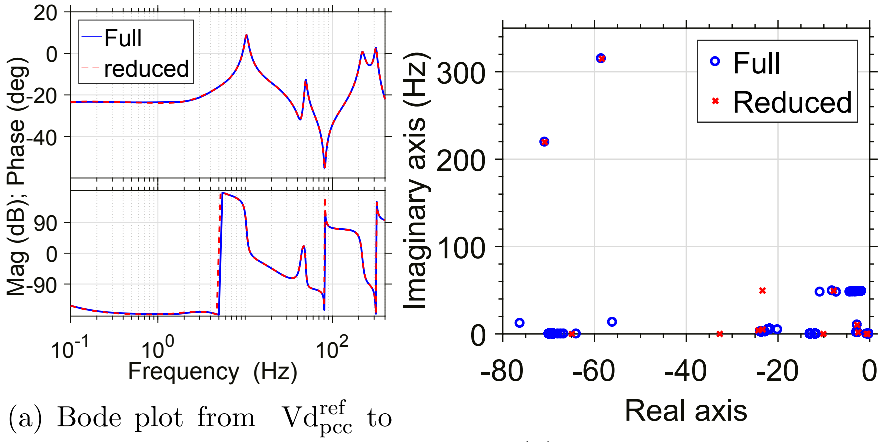

(a) Bode plot from Vd_{pcc}^{ref} to Vq_{pcc}

(b) Eigenvalue plot

Figure 3.13: Frequency domain comparison of complete system: FOM vs. ROM using ADI

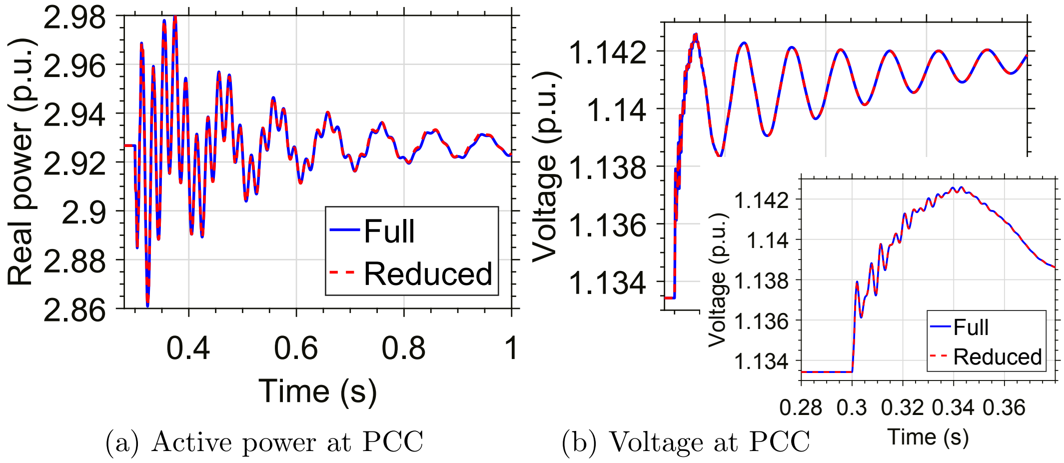

(a) Active power at PCC

(b) Voltage at PCC

Figure 3.14: Time domain comparison of complete system: FOM vs. ROM using ADI

The Bode and eigenvalue plots of the FOM and ROM are compared in Fig. 3.13 to investigate the accuracy of ROM. It is obvious that the frequency responses of both systems match very accurately over a wide range of frequency. The ROM is also able to preserve four critical modes of the FOM. These results are consistent with the time-domain simulation when the *study area* is perturbed using the fault used in the previous case. Fig. 3.14 shows that the ROM behaves very similar to the FOM. The MSE values for the corresponding PCC power and voltage as given in Table 3.2 are 4.80×10^{-5} and 2.05×10^{-6}, respectively.

The above performance comparisons clearly indicate that the ADI-based BT method is able to attain comparable accuracy to the original BT method. However, the main advantage of ADI iteration is the ability to solve Lyapunov equations efficiently for large-scale systems; thus giving rise to a significant reduction in the extraction time by a factor of around 22 as given in

Table 3.2.

Lastly, with regard to stability preservation of the ADI method, although to the knowledge of the author, there is no guarantee of it, an unstable ROM of the wind farm model has never been found. Even when small numbers of Arnoldi iterations and shift parameters are used, a stable ROM has always been obtained. For instance, when the numbers of Arnoldi iterations are set to $k_+ = 10$ and $k_- = 5$, while the number of ADI shift parameters is set to $J = 5$, the ROMs with orders 6, 18, and 33 are all stable.

3.2.5 Rational Krylov

Different from the previous approaches, the method presented in this subsection is based on moment matching via Krylov subspace known as RK. This means that the ROM preserves moments of the FOM at a set of interpolation points. As will be shown in Subsection 3.2.6, selecting these points, denoted as σ_i, is a crucial factor for the accuracy of RK method. They are often selected from the mirror image of dominant poles [77].

The basic principle of RK method is to carry out a Laurent series expansion to system transfer function in (3.5) at the points of interest. More specifically, given a single-input single-output (SISO) system, the transfer function can be expanded around infinity, i.e. $\sigma \approx \infty$:

$$G(s) = \sum_{i=1}^{\infty} m_i s^{-i}, \text{with } m_i = CA^{i-1}B \tag{3.26}$$

The term m_i is known as the i^{th} moment of the transfer function. In more general cases, $G(s)$ may be also expanded at $\sigma \neq \infty$ as follows:

$$\begin{aligned} G(s) &= \sum_{i=0}^{\infty} m_i (s-\sigma)^i \\ \text{with } m_i(\sigma) &= CA^{-(i+1)}B, \text{ for } \sigma = 0 \text{ or} \\ m_i(\sigma) &= C(\sigma I - A)^{-(i+1)}B, \text{ for } \sigma \neq 0 \text{ or } \infty \end{aligned} \tag{3.27}$$

In moment matching methods, $\hat{G}(s)$ is an approximation of $G(s)$ if it preserves k moments of the original system, namely $m_i = \hat{m}_i$, for $i = 1, 2, ...k$. The terms $\hat{m}_i$ denote the moments of $\hat{G}(s)$. In RK method, the moments, nevertheless, are not computed explicitly like in (3.26) or (3.27) to avoid the risk of numerical non-convergence because of ill-conditioning. The moment matching is instead performed using projection onto a Krylov subspace defined as:

$$\mathcal{K}_q(A, B) = \text{span}\left\{B, \quad AB, \quad A^2B, \quad \cdots, \quad A^{q-1}B\right\} \tag{3.28}$$

If V and W in (3.13) are selected to span a certain Kylov subspace, then the moments of FOM are automatically preserved in the ROM. The preservations are often selected from the following options [72, 75]:

1. If $\text{span}(V) = \mathcal{K}_{q1}(A, B)$ and $\text{span}(W) = \mathcal{K}_{q2}(A^T, C^T)$, then $\hat{G}(s)$ preserves $q1 + q2$ moments of $G(s)$ at infinity.
2. If $\text{span}(V) = \mathcal{K}_{q1}(A^{-1}, A^{-1}B)$ and $\text{span}(W) = \mathcal{K}_{q1}(A^{-T}, A^{-T}C^T)$, then $\hat{G}(s)$ preserves $q1 + q2$ moments of $G(s)$ at zero.
3. If $\text{span}(V) = \mathcal{K}_{q1}((A - \sigma I)^{-1}, (A - \sigma I)^{-1}B)$ and $\text{span}(W) = \mathcal{K}_{q1}((A - \sigma I)^{-T}, (A - \sigma I)^{-T}C^T)$, then $\hat{G}(s)$ preserves $q1 + q2$ moments of $G(s)$ at σ.
4. If σ in option 2) and 3) is multiple points, i.e. $\sigma = [\sigma_1, ..., \sigma_i]$, by taking V and W as the union of Krylov subspaces corresponding to each σ_i, i.e. $V = [V_1, ..., V_i]$ and $W = [W_1, ..., W_i]$, then $\hat{G}(s)$ preserves $q1 + q2$ moments of $G(s)$ at each σ_i. This is known as the generalized Krylov subspace.

Although the discussion above assumes that the system is SISO, it can be extended to MIMO systems by using a block Krylov subspace [89]. This approach is nonetheless only applicable for systems with minimum number of inputs and outputs since the number of moment matching is inversely proportional to the number of inputs and outputs. Furthermore, it is to be noted if the power of A is continuously multiplied by B as in (3.28), the resulting vectors will eventually converge to the dominant eigenspace of A. This condition is undesirable due to the fact that the new vector becomes closely parallel to the previous vectors, and consequently $\mathcal{K}_q$ becomes ill-conditioned. To deal with this problem, a Krylov vector is orthogonalised against previous vectors using Arnoldi or Lanczos methods [72, 90].

Algorithm 5 given in Appendix A shows the procedure to obtain ROM using RK algorithm.

Table 3.3: Interpolation point scenario for RK

Scenario	Order	Interpolation points
RK1	8	$8.17 \pm 310.17i$(MM1), $2.72 \pm 64.94i$(MM2)
RK2	20	$8.17 \pm 310.17i$(MM1), $2.72 \pm 64.94i$(MM2), $58.50 \pm 1979.16i$(MM3), $70.83 \pm 1379.46i$(MM4)
RK3	36	$0, \pm 1i$, $\pm 10i$, $\pm 40i$, $8.17 \pm 310.17i$(MM1), $2.72 \pm 64.94i$(MM2), $58.50 \pm 1979.16i$(MM3), $70.83 \pm 1379.46i$(MM4)

3.2.6 Case study using rational Krylov

As previously indicated, RK method necessitates users to provide a set of interpolation points where the moments of FOMs are to be retained. It has been suggested in [77] that one can choose these points from mirror image of the poles of $G(s)$, specially those with high residue. For the wind farm model used in this work, those poles are given in Table. 3.1.

Three scenarios of moment matching shown in Table. 3.3 are considered to examine the influence of interpolation points on the accuracy of RK method. The first scenario, RK1, aims to match the moments at mirror image of two critical modes, namely MM3 and MM4. Note that for easy reference, the letters M are added to the mode names. For instance, MM3 and MM4 refer to mirror image of M3 and M4, respectively. In the RK2, more points are added to match the moments of high order system at mirror image of all critical modes, namely MM1 to MM4. Finally in RK3, a similar scenario to RK2 is considered with some additional points, which are not the dominant modes, to enhance accuracy of the ROM at low frequencies. These three scenarios are carefully selected to preserve the stability of the *external-area* since it is well-established that RK method does not preserve stability. Although selecting interpolation points from mirror image of poles of $G(s)$ often produces a stable ROM in this work, this simple approach sometimes yields an unstable ROM. For example when the interpolation points are $2.72 \pm 64.94i$ (MM2) and $70.83 \pm 1379.46i$ (MM4), then the ROM has two unstable modes.

The Bode plots from $\mathrm{Vq}_{\mathrm{pcc}}^{\mathrm{ref}}$ to $\mathrm{Id}_{\mathrm{pcc}}$ of the RK1-RK3 are compared to that of the FOM of *external-area* in Fig. 3.15. Although both RK1 and RK2 are able to produce accurate Bode plots at the preselected points, they are more erroneous at low frequency range. With the incorporation of interpolation points at low frequency, RK3 produces much more accurate

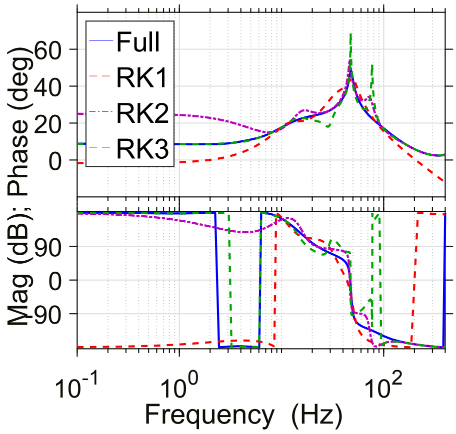

Figure 3.15: Bode plot of *external-area* from Vq_{pcc}^{ref} to Id_{pcc}: FOM vs. ROM using RK

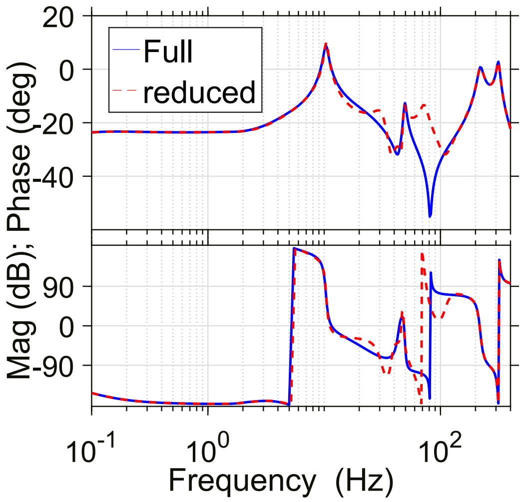

(a) Bode plot from Vd_{pcc}^{ref} to Vq_{pcc}

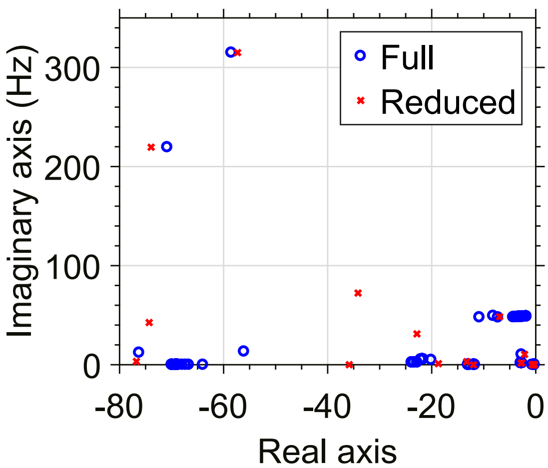

(b) Eigenvalue plot

Figure 3.16: Frequency domain comparison of complete system: FOM vs. ROM using RK

results. This finding shows that the choice of interpolation points has a profound influence on accuracy of the ROM. For further analysis, RK3 is selected.

The Bode and eigenvalue plots when the RK3 is reconnected to the *study-area* are shown in Fig. 3.16. Although small errors are noticed in the Bode and eigenvalue plots, the ROM is generally able to capture the critical modes of the FOM. Further, the time-domain simulation is performed by using the same scenario as used previouly for the fault. The responses of PCC power and voltage are given in Fig. 3.17. It is likely that the errors previously encountered in the frequency-domain might be attributed to the accuracy of the method in time-domain simulation. The MSE values for both PCC power and voltage are slightly larger than those in the previous cases as indicated in Table. 3.2. Finally, as also shown in Table 3.2, the main

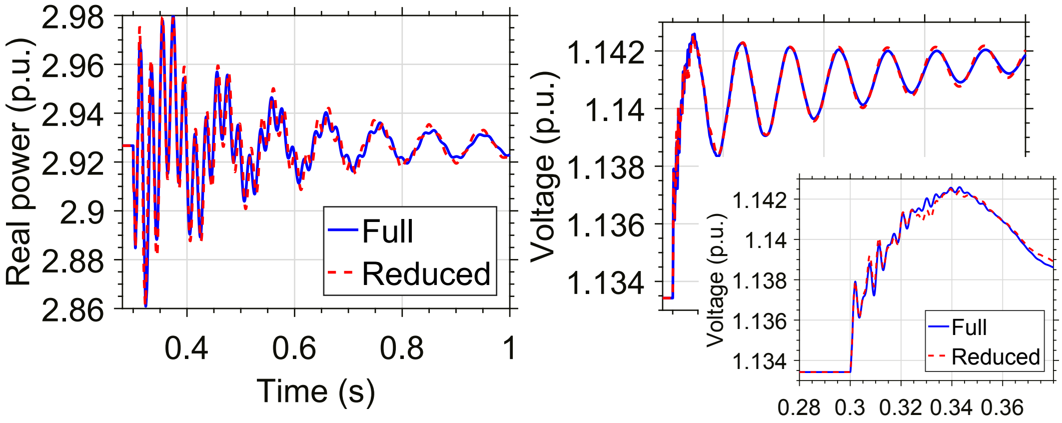

(a) Active power at PCC (b) Voltage at PCC

Figure 3.17: Time domain comparison of complete system: FOM vs. ROM using RK

advantage of RK is a significant reduction in the extraction time, which accounts only for 0.32 s.

3.2.7 Iterative rational Krylov algorithm

The operating condition of a system always continuously changes, which may accordingly alter its dominant modes. In this condition, interpolation point selection of RK method may become increasingly difficult. This subsection presents IRKA to overcome this problem. The IRKA method also uses a tangential interpolation technique proposed in [91] to handle MIMO systems. The details of IRKA method are as follows.

Suppose $G(s)$ is the transfer matrix of a MIMO system and a set of z interpolation points with associated right and left tangential directions $\{\sigma_i, r_i, l_i\}$, $i = 1, \ldots\ z$ are given. If V and W are constructed such that:

$$\begin{aligned} \text{span}(V) &= (\sigma_i I - A)^{-1} B r_i \\ \text{span}(W) &= (\sigma_i I - A)^{-1} C^T l_i \end{aligned} \tag{3.29}$$

then $\hat{G}(s)$ interpolates $G(s)$ tangentially at σ_i. Apart from that, the following conditions are also satisfied [91, 92]:

$$\begin{aligned}
&l_i^T G(\sigma_i) = l_i^T \hat{G}(\sigma_i) \\
&G(\sigma_i) r_i = \hat{G}(\sigma_i) r_i, \\
&l_i^T G^{'}(\sigma_i) r_i = l_i^T \hat{G}^{'}(\sigma_i) r_i, \ \forall i = 1, 2, \ldots, z
\end{aligned} \tag{3.30}$$

Eqn. (3.30) shows that the IRKA uses a more relaxed condition than RK method which uses the exact interpolation. The remaining problem is to appropriately select $\{\sigma_i, r_i, l_i\}$. In IRKA method, $\{\sigma_i, r_i, l_i\}$ are selected to minimise H_2 norm error between $G(s)$ and $\hat{G}(s)$:

$$\min \left\| G(s) - \hat{G}(s) \right\|_2^2 \tag{3.31}$$

Let $G(s)$ be expressed in terms of a pole-residue representation as follows:

$$G(s) = \sum_{i=1}^{n} \frac{c_i b_i^T}{s - \lambda_i} = \frac{R_i}{s - \lambda_i} \tag{3.32}$$

where $AX^v = X^v \mathrm{diag}(\lambda_1, ..., \lambda_n)$, $c_i = CX^v e_i$, and $b_i = (e_i^T Y^v B)^T$ with $Y^v = X^{v-1}$. Columns of X^v and Y^v are constructed from the right and left eigenvectors of λ_i, respectively. The triplet $\{\lambda_i, x_i^v, y_i^v\}$ is commonly referred as an eiganpair and R_i is known as the residue of λ_i. The IRKA performs an iterative procedure to find $\hat{G}(s)$:

$$\hat{G}(s) = \sum_{i=1}^{r} \frac{\hat{c}_i \hat{b}_i^T}{s - \hat{\lambda}_i} = \frac{\hat{R}_i}{s - \hat{\lambda}_i} \tag{3.33}$$

which satisfies (3.31). The first order optimality conditions for this problem is derived in [93]. If $\hat{G}(s)$ is the solution of (3.31), then the following conditions hold:

$$\begin{aligned}
&\hat{c}_i^T G(-\hat{\lambda}_i) = \hat{c}_i^T \hat{G}(-\hat{\lambda}_i) \\
&G(-\hat{\lambda}_i) \hat{b}_i = \hat{G}(-\hat{\lambda}_i) \hat{b}_i \\
&\hat{c}_i^T G^{'}(-\hat{\lambda}_i) \hat{b}_i = \hat{c}_i^T \hat{G}^{'}(-\hat{\lambda}_i) \hat{b}_i, \ \forall i = 1, \ldots, r
\end{aligned} \tag{3.34}$$

where $\hat{\lambda}_i$ are poles of $\hat{G}(s)$ with associated residues $\hat{c}_i, \hat{b}_i$. Therefore, Eqn. (3.34) suggests that the interpolations points should be selected from mirror image of the eigenvalues of ROM, while the corresponding tangential directions are selected from the associated left and right eigenvectors.

The complete procedure of MOR using IRKA method is given by Algorithm 6 in Appendix A.

3.2.8 Case study using iterative rational Krylov algorithm

The performance of RK method is determined by selection of the interpolation points, which is often difficult to do. This is exacerbated by the fact that the operating condition of wind farms continuously changes, which in turn affects the dominant modes. With the aim to overcome these difficulties, IRKA is adopted to reduce the wind farm model. In this way, a set of initial interpolation points with corresponding tangential directions are iterated until a suboptimum point solving (3.31) is found. Implementation of this method in Matlab given by [88] is used in this thesis.

To demonstrate effectiveness of IRKA method, three ROMs of the *external-area*, namely, IRKA1, IRKA2, and IRKA3, are considered. These models have the same order as RK1, RK2 and RK3, respectively. The initial interpolation points with the corresponding right and left tangential directions in all models are randomly selected. Using these random parameters, IRKA method is able to converge within 16, 81, and 23 iterations and requires elapsed time of 2.51 s, 19.41 s, and 7.41 s for IRKA1, IRKA2, and IRKA3, respectively. There are two stopping criteria adopted in this study, namely, the H_2-norm for interpolation point error and reduced system error (see Algorithm 6). If any of these criteria falls below a pre-specified tolerance, then the IRKA iteration stops. The final H_2-norm for the interpolation point error and reduced system error are 2.0×10^{-4} and 2.1×10^{-3} for IRKA1, 8.8×10^{-3} and 8.5×10^{-4} for IRKA2, and 2.6×10^{-4} and 8.7×10^{-4} for IRKA3. The Bode plots from $\mathrm{Vq}_{\mathrm{pcc}}^{\mathrm{ref}}$ to $\mathrm{Id}_{\mathrm{pcc}}$ for these ROMs are compared with that of the FOM of *external-area* in Fig. 3.18. It is obvious that the IRKA3 produces more accurate results than IRKA1 and IRKA2. Also, comparison between Fig. 3.15 and Fig. 3.18 demonstrates that in general the IRKA method has superior performances to the RK method. For further analysis, only the IRKA3 is considered.

To investigate the accuracy of IRKA method, the responses of complete ROM with IRKA3

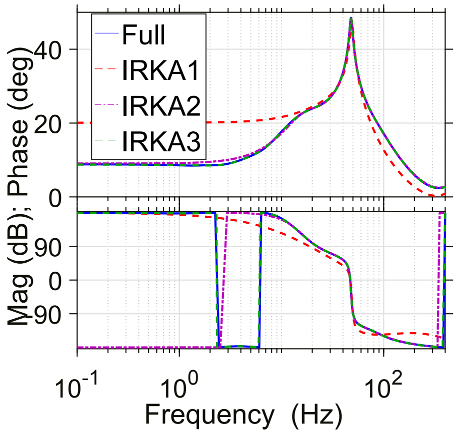

Figure 3.18: Bode plot of *external-area* from Vq_{pcc}^{ref} to Id_{pcc}: FOM vs. ROM using IRKA

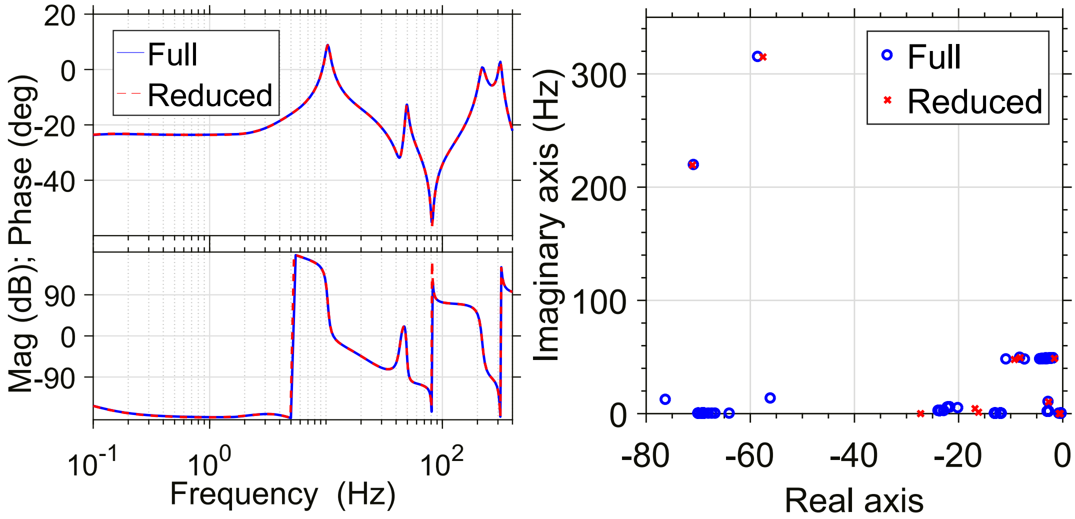

(a) Bode plot from Vd_{pcc}^{ref} to Vq_{pcc} (b) Eigenvalue plot

Figure 3.19: Frequency domain comparison of complete system: FOM vs. ROM using IRKA

are compared with those obtained from FOM. The Bode and eigenvalue plots are given in Fig. 3.19, which show generally excellent performances of IRKA method to resemble the FOM. These results are also consistent with the time-domain simulation outcomes given in Fig. 3.20. The corresponding MSE values for PCC power and voltage are respectively 1.45×10^{-5} and 1.52×10^{-5} as listed in Table 3.2, which are smaller than those from RK method.

It is to be noted that in term of stability preservation, to the knowledge of author, the IRKA essentially does not preserve stability of the FOM. This is observed from a large number of experiments in which unstable ROMs of the wind farms are sometimes generated. However, compared with RK method, IRKA method is by far less often to produce unstable ROMs.

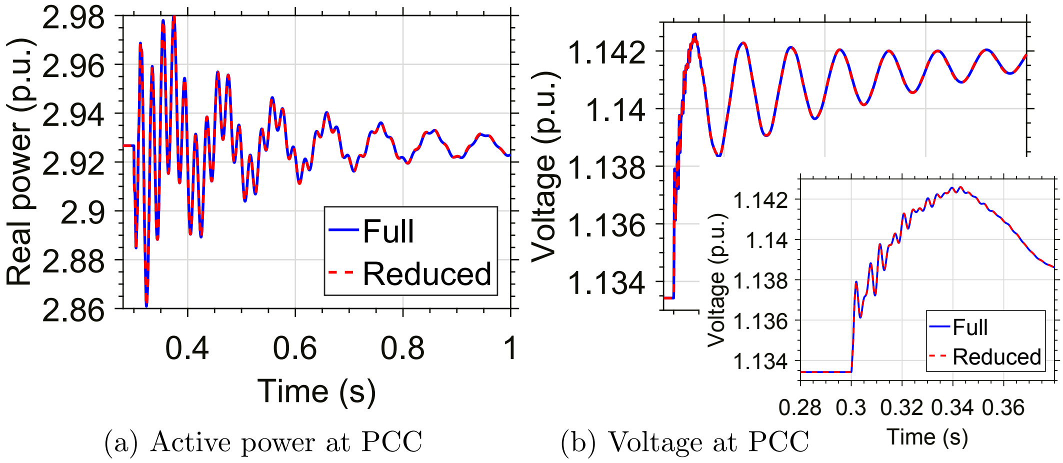

(a) Active power at PCC (b) Voltage at PCC

Figure 3.20: Time domain comparison of complete system: FOM vs. ROM using IRKA

3.2.9 Modal truncation

Subsection 3.2.7 shows that IRKA method seeks $\hat{R}_i$ and $\hat{\lambda}_i$ in (3.33), so that (3.31) is minimized. On the other hand, the modal truncation presented here constructs a ROM so that (3.33) preserves r most dominant modes of (3.32). In other words, the IRKA preserves moments of FOM, while the modal truncation method retains the modes of FOM. In this way, stability preservation is always guaranteed by the modal truncation method. One way to define dominant eigenvalues is using the corresponding residue R_i of λ_i. A mode λ_i is called dominant if it has a large ratio of $\|R_i\|_2 / |\mathrm{Re}(\lambda_i)|$; thus, the modal truncation selects r modes from the FOM with the r largest ratio.

When the method is applied to a large-scale system, the calculation of all eigenpairs $\{\lambda_i, x_i^v, y_i^v\}$ and then selection of dominant modes based on the ratio of $\|R_i\|_2 / |\mathrm{Re}(\lambda_i)|$ become extremely expensive. To overcome the problem, the eigenpairs $\{\lambda_i, x_i^v, y_i^v\}$ should be calculated one-at-a-time until r eigenpairs are found. In [78], a new method known as a SAMDP algorithm has been successfully used to extract dominant modes of large power system models. The method starts from an initial value of a pole and performs an iterative procedure until the pole with the largest ratio of $\|R_i\|_2 / |\mathrm{Re}(\lambda_i)|$ is found (see Algorithm 7 in Appendix A). During the iteration, the corresponding right and left eigenvectors are also calculated. Once this pole is found, it is deflated to prevent the iterations to converge to the same pole. This process is repeated until r eigenpairs are found. Having completed this process, the right and left eigenvectors are put into columns of V and W, respectively, as follows:

$$W = \begin{bmatrix} y_1^v & \bigg| & \cdots & \bigg| & y_r^v \end{bmatrix}, \quad V = \begin{bmatrix} x_1^v & \bigg| & \cdots & \bigg| & x_r^v \end{bmatrix} \tag{3.35}$$

The ROM is obtained by applying V and W to the FOM as in (5.2).

3.2.10 Case study using modal truncation

In this section, effectiveness of the SAMDP method to obtain ROM of the wind farm is investigated. Different from the previous methods, it is found that the SAMDP cannot be applied directly to the original linearized model of the *external-area*. It might be caused by the problem of eigenvalue conditioning, which can be studied using the condition number of the eigenvector matrix as follows:

$$\mathrm{cond}(X^v) = \|X^v\|_2 \left\|X^{v-1}\right\|_2 = \|X^v\|_2 \|Y^v\|_2 \tag{3.36}$$

The original system has this number at around 1250, which indicates that the eigenvalues are very sensitive to any changes in elements of A, for instance due to rounding-error. As the SAMDP method performs an explicit calculation of eigenpairs $\{\lambda_i, x_i, y_i\}$, it cannot converge unless $\mathrm{cond}(X^v)$ is reduced. To do this, a similarity transformation is performed as follows:

$$A_{\mathrm{sim}} = T^{-1}AT \tag{3.37}$$

where A_{sim} has equal row and column norm whenever possible. This is carried out by using a Matlab® command *balance*. Performing this step, $\mathrm{cond}(X^v)$ decreases significantly to 803.80, which in turn enables the SAMDP to converge. It is to be noted that A and A_{sim} have the same sets of eigenvalues since the similarity transformation always preserves eigenvalues of the original system.

Three scenarios are considered to study the performance of SAMDP, namely SAMDP1 (18 dominant modes), SAMDP2 (40 dominant modes), and SAMDP3 (180 dominant modes). The

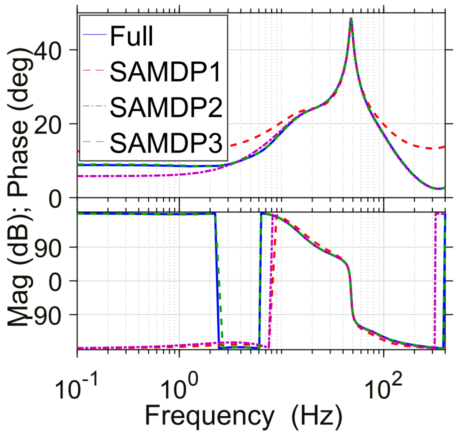

Figure 3.21: Bode plot of *external-area* from $\mathrm{Vq}_{\mathrm{pcc}}^{\mathrm{ref}}$ to $\mathrm{Id}_{\mathrm{pcc}}$: FOM vs. ROM using SAMDP

orders of these models are 36, 74, 301 for SAMDP1-SAMDP3, respectively. Also, an initial value of the pole is set to $1i$ in all cases. The Bode plots from $\mathrm{Vq}_{\mathrm{pcc}}^{\mathrm{ref}}$ to $\mathrm{Id}_{\mathrm{pcc}}$ for these models are compared with that of the FOM of *external-area* in Fig. 3.21. As can be noticed, higher number of poles needs to be incorporated to improve accuracy of SAMDP method. SAMDP method also requires significantly higher order than the other methods to achieve comparable accuracy. It might be due to the fact that the method gives a high priority to the modes whose ratios of $\|R_i\|_2 / |\mathrm{Re}(\lambda_i)|$ are high. However, these modes might not be always important for system dynamics; hence selecting them merely leads to a higher order ROM and does not improve accuracy of the ROM. Another reason might be rather than replacing multiple modes which are close to each other with an equivalent mode, the SAMDP method extracts all of them. The SAMDP3 is selected for further analysis.

Fig. 3.22 shows performance of the completed ROM with SAMDP3 in the frequency-domain. In terms of the Bode and eigenvalue plots, the ROM is able to produce accurate estimate of FOM responses over a wide range of frequency as well as to preserve the four critical modes. This translates into excellent time-domain performances as illustrated in Fig. 3.23, where very small errors are observed in the waveforms of PCC power and voltage. The values of MSE for these plots are given in Table 3.2. A further increase in the system order should be able to minimize the errors.

There are two important technical details to be discussed. Firstly, the SAMDP is able to efficiently extract 180 modes within only 31.17 s, see Table 3.2. Secondly, due to the fact that the SAMDP extracts the poles of FOM one-at-a-time, stability of ROM is always guaranteed

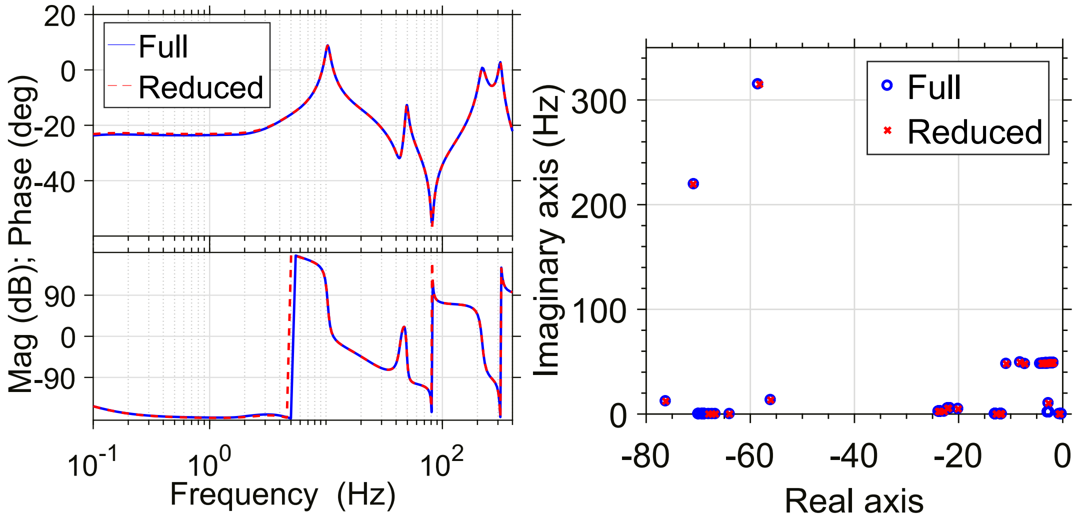

(a) Bode plot from Vd_{pcc}^{ref} to Vq_{pcc} (b) Eigenvalue plot

Figure 3.22: Frequency domain comparison of complete system: FOM vs. ROM using SAMDP

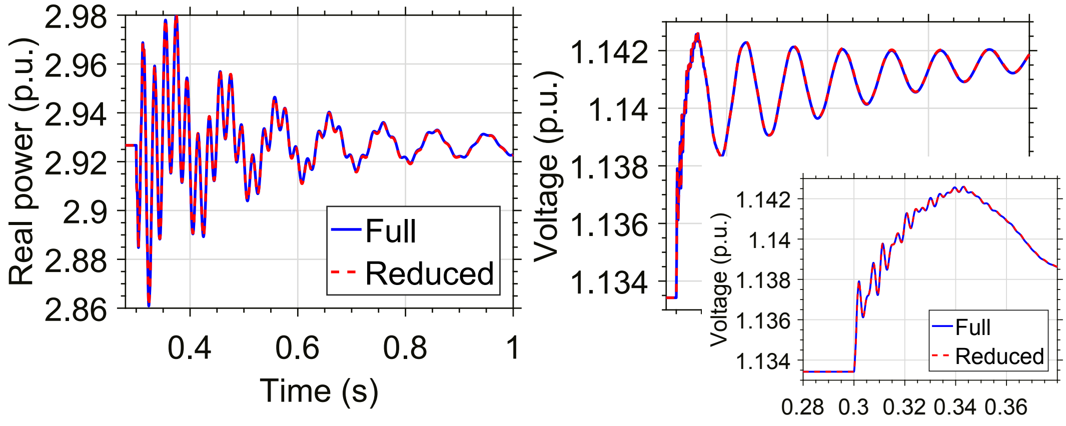

(a) Active power at PCC (b) Voltage at PCC

Figure 3.23: Time domain comparison of complete system: FOM vs. ROM using SAMDP

whenever the FOM is stable.

Since the SAMDP method always produces a much higher dimension of ROM than other methods, it is often suggested to use SAMDP method as an intermediate technique [94]. This means that in the first stage the FOM is reduced by using the SAMDP to obtain a medium-sized system with order of higher than 200. As previously found using SAMDP method, an appropriate size for the wind farms model is around 300-400. In the second stage, the medium-sized system can be further reduced using BT method to the size of around ten times smaller. The advantages of this hybrid method are at least threefold:

1. A significant order reduction than solely using SAMDP method.

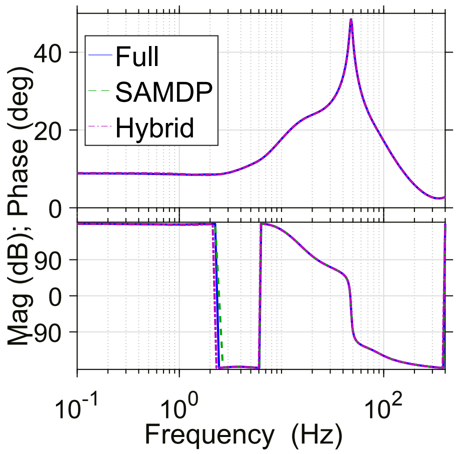

Figure 3.24: Bode plot of *external-area* from Vq_{pcc}^{ref} to Id_{pcc}: FOM, SAMDP, and Hybrid method

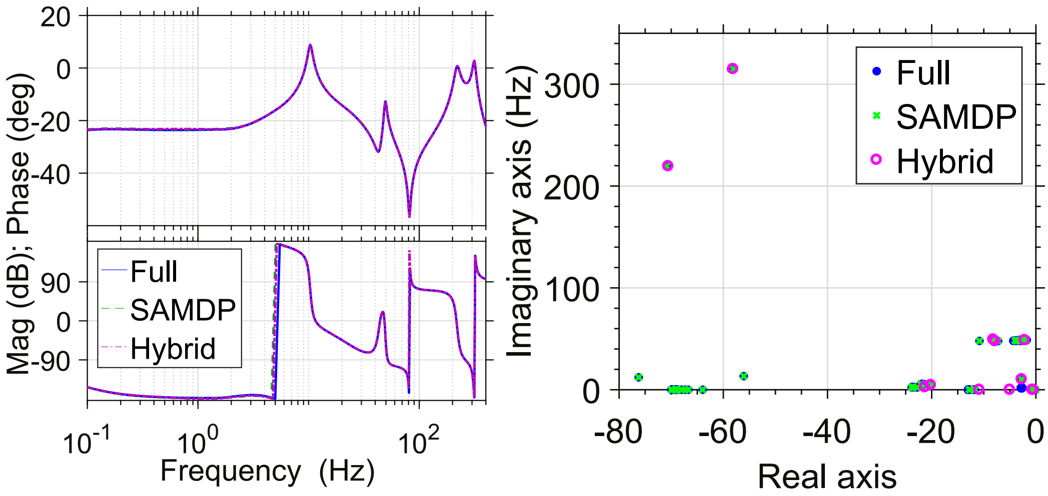

(a) Bode plot from Vd_{pcc}^{ref} to Vq_{pcc}

(b) Eigenvalue plot

Figure 3.25: Frequency domain comparison of complete system: FOM, SAMDP, and Hybrid method

2. A significant reduction in extraction time than solely using BT method.
3. Stability preservation. Because both the BT method and SAMDP method preserve the stability of FOM, then the hybrid method derived from these methods also preserves the stability.

The results of applying the hybrid method to the wind farm model are depicted in Figs. 3.24-3.26. The comparison is performed between the FOM, SAMDP, and hybrid method in the time- and frequency-domain (see also Table 3.2). The orders of models obtained using SAMDP and hybrid method are 307 and 46, respectively, and the extraction time for the hybrid method is 38.98 s, which accounts for 38.26 s for SAMDP method in the first stage and 0.72 s for

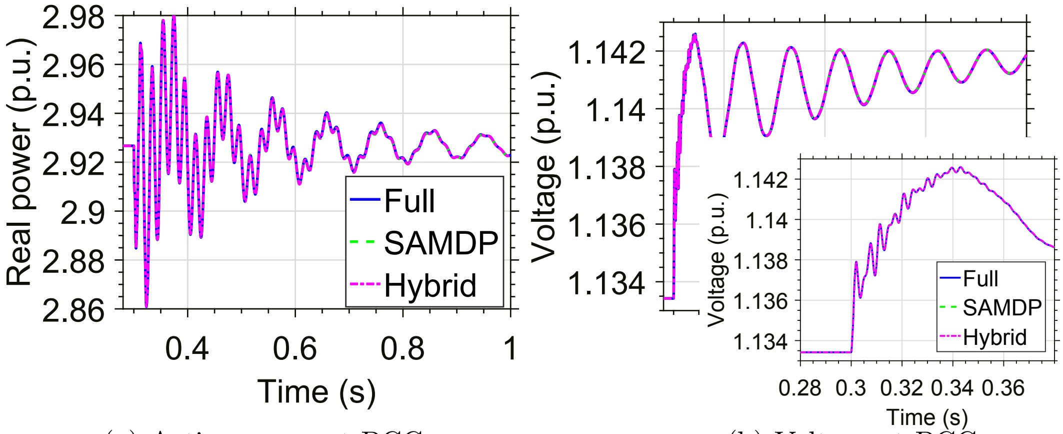

(a) Active power at PCC (b) Voltage at PCC

Figure 3.26: Time domain comparison of complete system: FOM, SAMDP, and Hybrid method

BT method in the second stage. This extraction time is much faster than solely using BT method, which is around 433 s. From Figs. 3.24-3.26, the hybrid method is able to produce very accurate responses of FOM both in the time- and frequency-domain at much lower order than the SAMDP.

3.3 Reduced order model of different orders of wind farm models

This section investigates the influence of wind farm model order on the performances of the MOR methods. To do this, two new wind farm models are obtained from the modifications of the previous wind farm model in Fig. 3.1. Firstly, the Wind Farm 2 in Fig. 3.1 is removed, which yields a new wind farm with an order of 2902. This wind farm has a total of 90 DFIGs and is referred as System 1. Secondly, the Wind Farm 1 in Fig. 3.1 is duplicated, resulting in a new system with a total of 210 DFIGs and an order of 6770. This system is termed as System 3. The original wind farm model consisting of 120 DFIGs is referred as System 2.

Table 3.4 shows performances of the five methods on the System 1, System 2, and System 3. Note that the results of System 2 are presented again here for the sake of clarity. It is obvious that the BT method consistently has the highest computation time in virtually all cases. The increase in computational time of BT is at a rate of around $\mathcal{O}(n^3)$, which stems from solving

Table 3.4: MOR on different wind farm models

Method	Performance	System 1 (2902)	System 2 (3874)	System 3 (6770)
BT	Order	39	39	51
	Extraction	186.42 s	433.00 s	2168.55 s
	MSE P_{PCC}	8.35×10^{-6}	3.77×10^{-4}	2.33×10^{-4}
	MSE V_{PCC}	1.39×10^{-6}	2.96×10^{-4}	1.14×10^{-5}
	MSE Bode	5.29×10^{-4}	8.10×10^{-3}	5.20×10^{-3}
ADI	Order	39	39	51
	Extraction	14.53 s	19.18 s	32.19 s
	MSE P_{PCC}	8.38×10^{-6}	4.80×10^{-5}	2.20×10^{-4}
	MSE V_{PCC}	1.40×10^{-6}	2.05×10^{-6}	1.14×10^{-5}
	MSE Bode	5.30×10^{-4}	6.14×10^{-4}	5.20×10^{-3}
RK	Order	38	42	28
	Extraction	0.23 s	0.32 s	0.31 s
	MSE P_{PCC}	4.02×10^{-4}	4.30×10^{-3}	3.60×10^{-2}
	MSE V_{PCC}	7.78×10^{-6}	9.90×10^{-4}	1.80×10^{-3}
	MSE Bode	2.90×10^{-2}	2.60×10^{-2}	2.50×10^{-1}
IRKA	Order	38	42	28
	Extraction	6.67 s	7.41 s	77.33 s
	MSE P_{PCC}	1.74×10^{-5}	1.45×10^{-5}	7.10×10^{-3}
	MSE V_{PCC}	1.80×10^{-6}	1.52×10^{-5}	4.20×10^{-3}
	MSE Bode	5.90×10^{-4}	2.20×10^{-3}	1.60×10^{-2}
SAMDP	Order	110	307	339
	Extraction	10.13 s	31.17 s	61.90 s
	MSE P_{PCC}	7.18×10^{-4}	2.42×10^{-4}	8.80×10^{-4}
	MSE V_{PCC}	2.54×10^{-5}	1.61×10^{-5}	6.03×10^{-5}
	MSE Bode	3.60×10^{-2}	1.30×10^{-3}	3.10×10^{-3}

the Lyapunov equations. This practically limits the use of BT for wind farm MOR in particular for near-real time applications. The introduction of ADI method reduces the computational time to approximately $\mathcal{O}(n)$ as evident from Table 3.4. The accuracy of ADI in all cases is practically similar to that of BT method. It is also confirmed that unstable ROMs calculated from ADI method are never found in all wind farm models.

On the whole, Table 3.4 also indicates that the IRKA outperforms the RK both in the time- and frequency-domain. However, the former requires significantly higher computational times. This observation is more pronounced as the system size increases. The computational time of RK by contrast remains less than 0.4 s for all test systems. It should also be noted that RK method often produces unstable ROMs and stability preservation becomes more difficult for higher order systems. More specially in System 3, after a large number of trial-and-errors, the RK method generally produces unstable ROMs in most trials. In IRKA method, stability of System 3 is also essentially not preserved, but the case with an unstable ROM is rarely found. Finally, in order to achieve comparable accuracy to other methods, the SAMDP constantly requires significantly higher orders than other methods and always produces stable ROMs in all cases. In addition, SAMDP method constantly requires eigenvalue preconditioning for all test systems.

3.4 Chapter summary

This chapter describes linear techniques, namely BT, ADI-based BT, RK, IRKA, and SAMDP methods, to obtain ROMs of wind farms during a small disturbance. The numerical advantages and disadvantages of each method have been analyzed on three large-scale wind farm systems with 90, 120, and 210 DFIGs. The accuracy of ROMs are investigated by the comparisons between FOM and ROM in terms of Bode plot, eigenvalue plot, and waveforms at the PCC. It is found that in general the ROMs are able to provide accurate estimate of the behaviours of the FOMs at much lower computational cost, which is particularly important if a fast assessment of the system stability is required for near real-time applications. The ROMs obtained from all methods are represented in the state-space model, hence it is relatively convenient to be implemented in industry-standard software packages.

Chapter 4

Linear model order reduction of MTDC systems

In the last decade, interest in grid connection of offshore wind farm power plants has been experiencing a significant increase due to more abundant and steadier wind energy potential in the middle of oceans. However, transporting the power to mainland using high voltage alternating current (HVAC) becomes more problematic since huge amount of reactive power is needed. The issue is more pronounced as the distance to mainland increases. To alleviate this problem, HVDC is often preferable.

There are currently two types of HVDC technologies used in offshore wind farm, namely current source converter (CSC) and VSC. While the former is a matured technology with a capacity up to 8000 MW, the latter seems to be more favourable in the context of offshore wind farm owing to advantageous operation with weak AC grids and low cost converter station [95]. The VSC HVDC is also conceptually expandable into a MTDC grid [96], which can potentially increase flexibility and reliability of system operation in the future. Although currently there have been only two VSC MTDC systems built in China, namely Nan'ao [97] and Zhoushan [98], other systems such as European super grid and DESERTEC [99] envisaged connecting several asynchronous AC grids, wind farms, and solar farms into a larger system [100] are also expected to be built in the future. In this context, stability study becomes very crucial to ensure a secure grid operation, and hence an accurate representation or modelling of MTDC system components is a vital aspect.

In this chapter, a method to develop a computationally efficient model of MTDC system is proposed. The method uses IRKA [88, 91] to individually reduce high order models of wind farms connected to a DC grid, while models of other components are retained using nonlinear equations. This, therefore, is a modular approach, and can be generalized to any number of wind farms. Simulation results using a four-terminal MTDC system with two large-scale wind farms and two asynchronous AC grids are discussed to demonstrate effectiveness of the proposed method. Different control strategies for the MTDC system are also considered. This chapter is organized as follows. The approach to ROM of the MTDC system is discussed in Section 4.1. It is followed by various study cases of different control strategies for the MTDC system in Section 4.2. Finally, conclusions are given in Section 4.3.

4.1 Approach to model order reduction

Fig. 4.1 shows the layout of an MTDC system used in this research. As can be seen, the model consists of four converter terminals, namely converter-1, -2, -3, and -4. The converter-1 and -3 are connected to two large-scale wind farms. These converters are in voltage control strategy as described in Subsection 2.2.4.1. Each wind farm consists of 48 DFIGs, which are modelled using 22 differential equations. The wind farms are taken from the Area 1 of Wind Farm 1 in Fig. 3.1. The operating conditions of both the wind farms are assumed to be the same and the incoming wind speed to each generator is calculated using the Jensen's wake effect model (see Section 3.1) [58]. In addition, the converter-2 is connected to the two-area system. This converter is set as the slack converter, which regulates the voltage in the DC grid as discussed in Subsection 2.2.4.2. All synchronous generators in the two-area system are represented using the transient model with only the G_4 equipped with a governor to regulate the system frequency. Lastly, converter-4 is connected to another onshore AC grid, which is modelled as an infinite bus. This converter is set to have an independent control of P_s and Q_s (see Subsection 2.2.4.3). All parameters are provided in Appendix C.

The system is modelled using Matlab/Simulink®. The order of overall model is 2929. The load

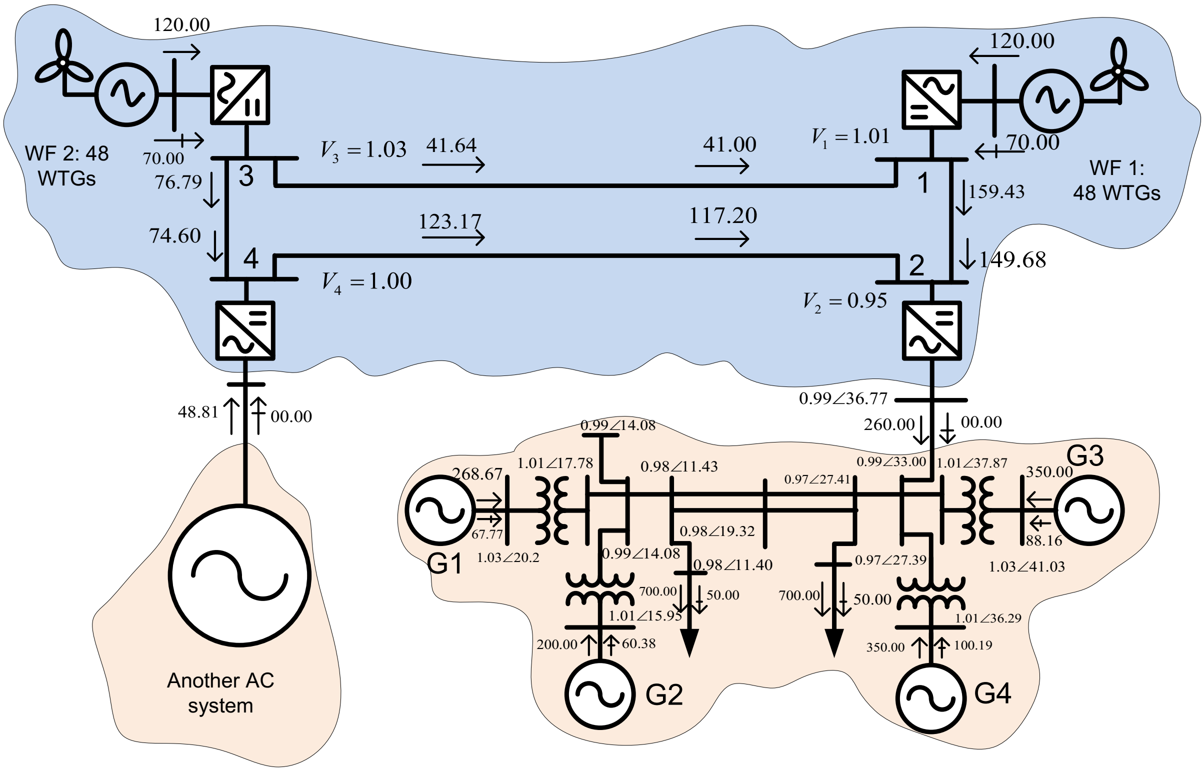

Figure 4.1: MTDC system with four terminals

flow condition is calculated using a sequential AC/DC power flow method [101, 102] and the result is also displayed in Fig. 4.1. In order to perform model order reduction of the MTDC system, it is divided into *study-area* and *external-area*. The wind farms are considered as the *external-area*, whereas the *study-area* comprises of the converters, DC grid, and onshore AC grids. The input and output for *external-area* is the current of RL filter i_f and the grid voltage v_s at offshore converter stations, respectively. For a consistent set of equations, the opposite variables, namely v_s and i_f, are respectively used as the input and output pair for the *study-area*.

Following this, model of the *external-area* is linearized using the Matlab® command *linearize*. The IRKA method is subsequently used to reduce order of the linearized system. Successful implementation of IRKA is a critical factor for the accuracy of final ROM. Once the reduced model of the *external-area* is completed, it is reconnected to the *study-area*. Note that at this point, the model of *study-area* is retained using nonlinear equations.

The performance of reduced system is investigated by comparing its responses with those of the nonlinear FOM in response to disturbances in the *study-area*. Accuracy of the waveforms is measured using MSE as given in (3.3).

4.2 Case study

4.2.1 Basic control strategy

This subsection analyses MOR of the four-terminal MTDC system adopting the basic control strategy discussed in Subsections 2.2.3 and 2.2.4. This means that the offshore converter stations are connected to wind farms control grid voltages, v_s, and an onshore converter station is assigned to regulate the DC grid voltage. The remaining onshore converter stations can perform an independent control of grid's real and reactive power, P_s and Q_s. In the context of the MTDC system given in Fig. 4.1, the converter-1 and -2 control the grid voltage of the wind farm 1 and 2. The DC voltage control is assigned to the converter-3 and the converter-4 regulates the grid power P_s and Q_s.

As discussed previously in Section 4.1, the first step to perform MOR is to linearize the wind farm model using the Matlab command *linearize*. Each wind farm in Fig. 4.1 has an order of 1402. Using the IRKA method, the order is significantly reduced to 36. It is found that this order is sufficient to capture the dynamics of FOM. The IRKA converges in 48 and 35 iterations for the wind farm 1 and 2, respectively. Finally, the last step is to reconnect the ROMs of wind farms to the *study-area*, resulting in the ROM of whole MTDC model with an overall order of 197.

With the aim to examine accuracy of the ROM, two scenarios are considered. In the first scenario, CB-1, the mechanical input of G_3 drops by 1 p.u., whereas the second scenario, CB-2, considers a drop in P_s reference of converter-4 by 1 p.u. The time-domain responses of both FOM and ROM are shown in Fig. 4.2. In addition, the more detailed results are summarized in Table 4.1.

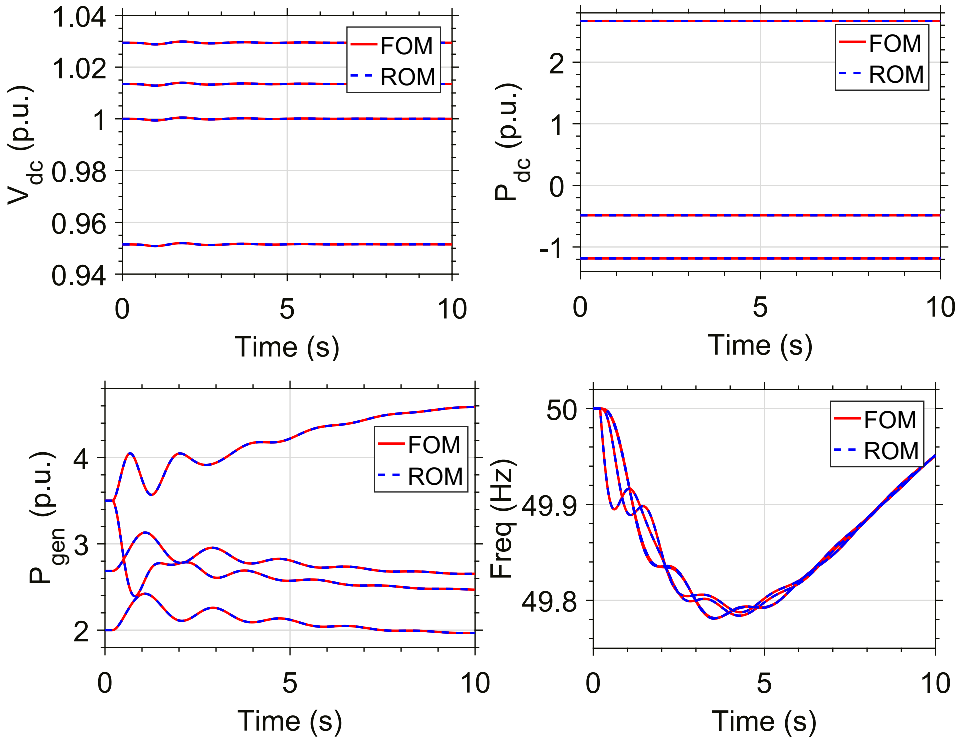

(a) Scenario CB-1: a 1.0 p.u. drop in mechanical power input of G_3

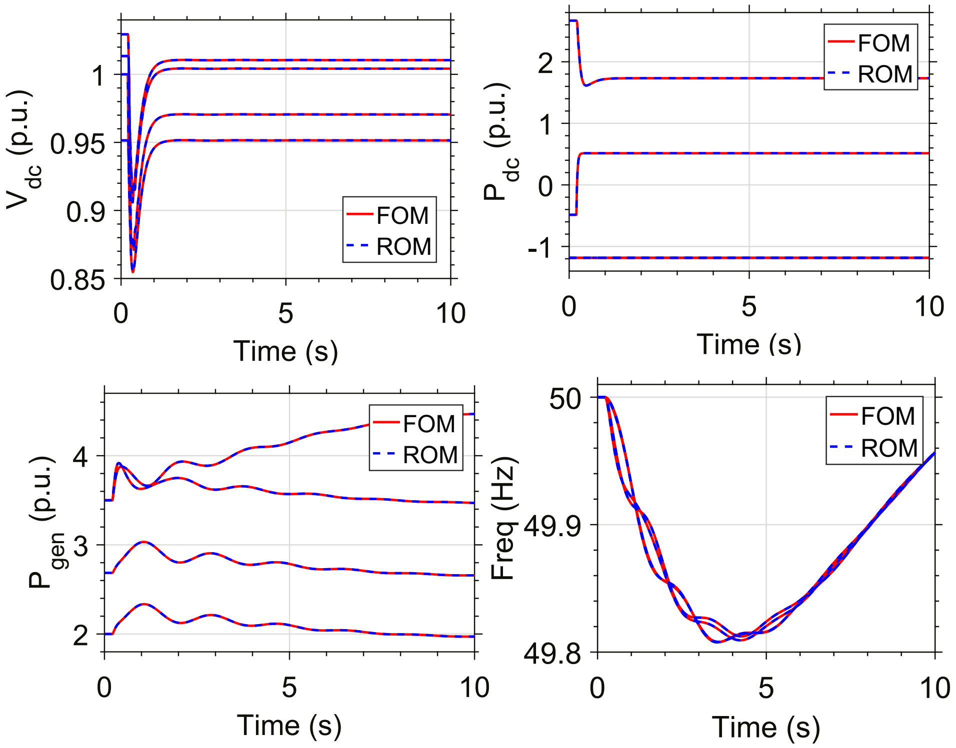

(b) Scenario CB-2: a 1.0 p.u. drop in P_s reference of converter-4

Figure 4.2: FOM vs. ROM using basic control strategy

Fig. 4.2a shows that because the mechanical input of G_3 drops by 1 p.u., the frequency of the

Table 4.1: MOR for basic control strategy

Method	Performance	Scenario 1 (CB-1)	Scenario 2 (CB-2)
FOM	Order	2929	2929
	Elapsed time	1995.76 s	1763.13 s
ROM	Order	197	197
	Elapsed time	40.63 s	55.61 s
	MSE v_{dc}	1.12×10^{-8}	2.80×10^{-6}
	MSE P_{dc}	2.96×10^{-6}	5.01×10^{-5}
	MSE P_{gen}	1.45×10^{-6}	2.31×10^{-6}
	MSE Frequency	5.41×10^{-8}	3.50×10^{-8}

two-area system decreases to around 49.8 Hz. The governor of G_4 brings back power balance in the system by increasing the mechanical input, and hence the nominal frequency is eventually restored. As is also obvious from the figure, the DC grid almost completely isolates the fault. This can be seen from the converter voltages and powers, which approximately stay unperturbed in response to the disturbance. In all cases, the ROM is able to capture this phenomenon very accurately; shown by extremely small MSE values as given in Table 4.1. Furthermore, the elapsed time of ROM to complete a 10 s simulation is only 40.63 s, which accounts for around 50 times faster than the elapsed time of FOM.

Furthermore, Fig. 4.2b shows responses of the systems when the reference of P_s at converter-4 decreases by 1.0 p.u. This leads to a change in the converter operating mode from initially injecting 48.81 MW to drawing around 50 MW from the DC bus. In response to this disturbance, the slack converter reduces power absorption from the DC grid by also around 1 p.u. (100 MW) to restore power balance DC grid, and as a result regulate the DC voltages. The two-area system detects this as shortage of generation, leading to a drop of frequency to 49.8 Hz. The governor reacts to the frequency drop by increasing the mechanical input to G_4. Finally, it is also noticed that the offshore converters can barely respond to the disturbance as power injection from both the wind farms remains constant. From Table 4.1, the ROM is able to emulate this behaviour very accurately, which is shown by small MSE values of all waveforms, at much faster simulation time.

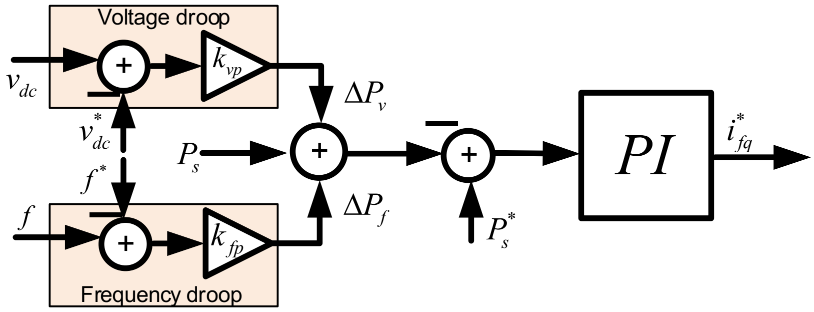

Figure 4.3: Voltage and frequency droop controller

4.2.2 Droop control strategy

From the previous discussion, one way to control the DC grid voltage is to assign an onshore converter station as the slack converter. However, in the event of a converter loss, the slack must make up the power outage to restore the power balance in the DC grid. Apart from that, the loss of the slack converter will result in a complete black-out in the MTDC system. Hence, the onshore converters are often equipped with a voltage droop controller as shown in Fig. 4.3 [103, 104]. This will lead to a more robust DC grid since all onshore converters will now be able to perform power sharing, depending on the voltage droop constant k_{vp}. In addition, the converters can also be equipped with a frequency droop controller to participate in grid frequency regulation. The frequency droop constant k_{fp} governs the participation of a controller in frequency regulation.

In this subsection, performance of the proposed reduced order model method is investigated on an MTDC system with both the voltage and frequency droop. The MTDC model given in Fig. 4.1 is slightly modified by incorporating the voltage droop controller to the converter-2 and -4, while only the converter-2 is equipped with the frequency droop controller. The k_{vp} and k_{fp} are set to 10 and -10, respectively.

The procedure to obtain ROM remains similar to the previous case where the IRKA method is used to reduce the order of wind farms from 1402 to 36, and hence the final model also has an order of 197. This system is subsequently also tested under two scenarios used in the previous study case. To avoid any confusion, CB-1 and -2 are now indicated as CD-1 and -2, respectively. Fig. 4.4 shows the time-domain simulation of both the FOM and ROM, while the detailed results are summarized in Table 4.2.

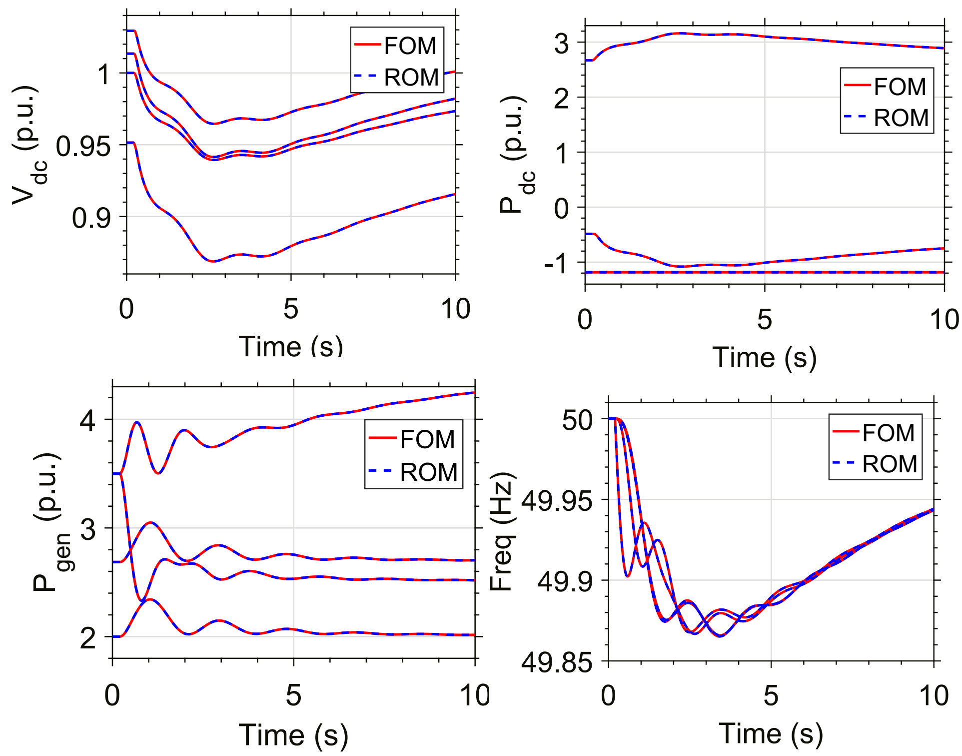

(a) Scenario CD-1: a 1.0 p.u. drop in mechanical power input of G_3

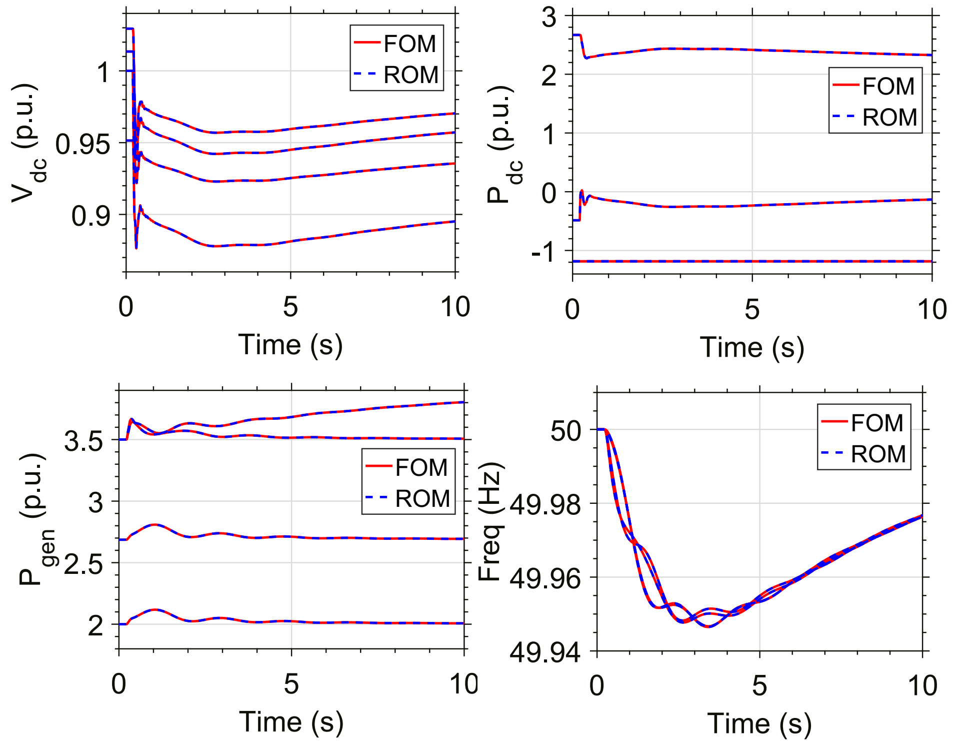

(b) Scenario CD-2: a 1.0 p.u. drop in P_s reference of converter-4

Figure 4.4: FOM vs. ROM using droop control strategy

As evident in Fig. 4.4, the ROM can reproduce accurate behaviours of the FOM in response

Table 4.2: MOR for droop control strategy

Method	Performance	Scenario 1 (CD-1)	Scenario 2 (CD-2)
FOM	Order	2929	2929
	Elapsed time	2393.69 s	1912.75 s
ROM	Order	197	197
	Elapsed time	56.03 s	61.91 s
	MSE v_{dc}	1.30×10^{-8}	1.41×10^{-5}
	MSE P_{dc}	1.83×10^{-7}	4.68×10^{-5}
	MSE P_{gen}	1.74×10^{-7}	6.67×10^{-6}
	MSE Frequency	1.98×10^{-8}	6.16×10^{-7}

to the disturbances. This is also equivalently shown in Table 4.2 where the MSE values of all waveforms for both the cases are very small. In addition, a dramatic drop in elapsed time by a factor more than 30 can also be noticed.

Specially in CD-1, the initial reduction in mechanical input of G_3 by 1 p.u. leads to a drop in the frequency of the two-area system (see Fig. 4.4a). This causes a response from the frequency droop controller at converter-2 to support the grid frequency by means of drawing more power from the DC grid, yielding a decrease in DC grid voltages. Consequently, the voltage droop controller of converter-4 reacts by injecting more power, proportional to k_{vp}, to the DC grid. Different from the earlier case, with the inclusion of the droop controllers, the disturbance is no longer completely isolated by the MTDC system. Also, in this case, the frequency only drops to around 49.87 Hz, which is smaller than that in CB-1, as the DC grid is now able to participate in the grid frequency support.

In CD-2, at the beginning the converter-4 exports power of 48.81 MW to the DC grid (see Fig. 4.4b). Afterwards, it exports only 15.00 MW. This triggers a reduction in the DC voltage, which subsequently prompts the voltage droop controller at converter-2 to inject more power, proportional to the voltage droop constant k_{vp}, to the DC system. As there is a deficit of generation in the two-area system, the frequency decreases to 49.95 Hz before the governor of G_4 eventually increases the mechanical power input to restore the frequency to 50 Hz.

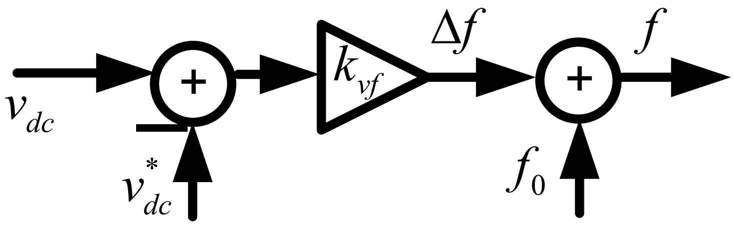

Figure 4.5: Voltage to frequency droop controller

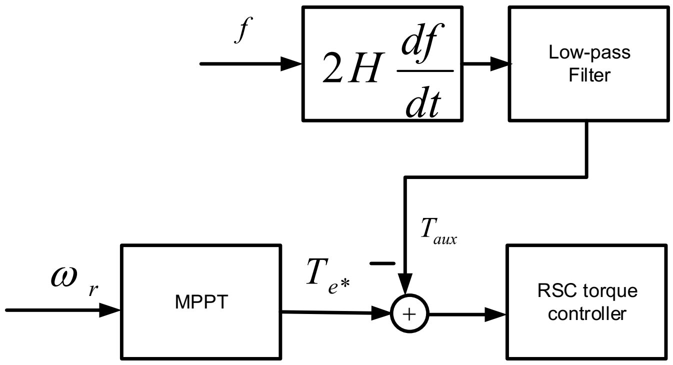

Figure 4.6: Virtual inertia controller

4.2.3 Inertia control strategy to support grid frequency

In this section, performance of the proposed ROM procedure is investigated on an MTDC system with inertia provision from offshore wind farms. From the previous case studies, it is apparent that the offshore wind farms are unaware of onshore grid frequency. A future vision of MTDC systems requires the wind farms to provide inertia support to onshore grids. This can be carried out using specific actions on converters and wind turbines as follows:

1. *Onshore converter*: the onshore converter needs to translate change in onshore grid frequency to change in DC voltage. This is done through the frequency droop controller which has been considered in Subsection 4.2.2.
2. *Offshore converter*: the offshore converter should be able to relate back change in DC grid voltage to change in offshore grid frequency. This can be carried through an analogous frequency droop controller as proposed in [104, 105]. This approach is shown in Fig. 4.5. k_{vf} is a positive constant.
3. *Wind turbines*: the wind turbines need to release the kinetic energy of rotors when change of frequency occurs. Here, a virtual inertia approach proposed in [106] is adopted. As illustrated in Fig 4.6, it uses the derivatives of frequency signal to modify the torque

command of the RSC.

With the frequency and voltage droop controllers already in place for the MTDC system in Fig. 4.1, only the offshore converter-1 and -3 need to adopt the control strategies shown in Fig. 4.5 and 4.6. The constant k_{vf} is set to 2 and H is the sum of rotor and turbine inertia constant.

The procedure to obtain ROM is given as follows. First, the IRKA is again used to reduce the order of both wind farm models from 1402 to 36, and hence the final ROM has an order of 197. Because the controllers in Figs. 4.5 and 4.6 are now considered, the *external-area* has one additional input, namely T_{aux}. The IRKA method converges in 26 and 35 iterations for wind farm 1 and 2, respectively. The accuracy of the ROM is then evaluated using the same scenarios used in the earlier case studies. In order to avoid the confusion, in this section, the scenarios are referred as CI-1 for 1 p.u. mechanical input drop and CI-2 for 1 p.u. P_s reference drop.

The results for both FOM and ROM during these scenarios are compared in Fig. 4.7 and also summarized in Table 4.3. It is obvious that the offshore converters can now participate in the grid frequency response by releasing the kinetic energy in the wind turbine rotors. This is noticeable from the increase in power injected to the DC grid through converter-1 and -3. As expected, the frequency drop is smaller than those in the previous cases. The ROM is generally able to yield an accurate estimate of this phenomenon, indicated by relatively small MSE values (see Table 4.3). There are also significant reductions in elapsed time for a 10 s simulation by factors of 325 and 347 for CI-1 and CI-2, respectively.

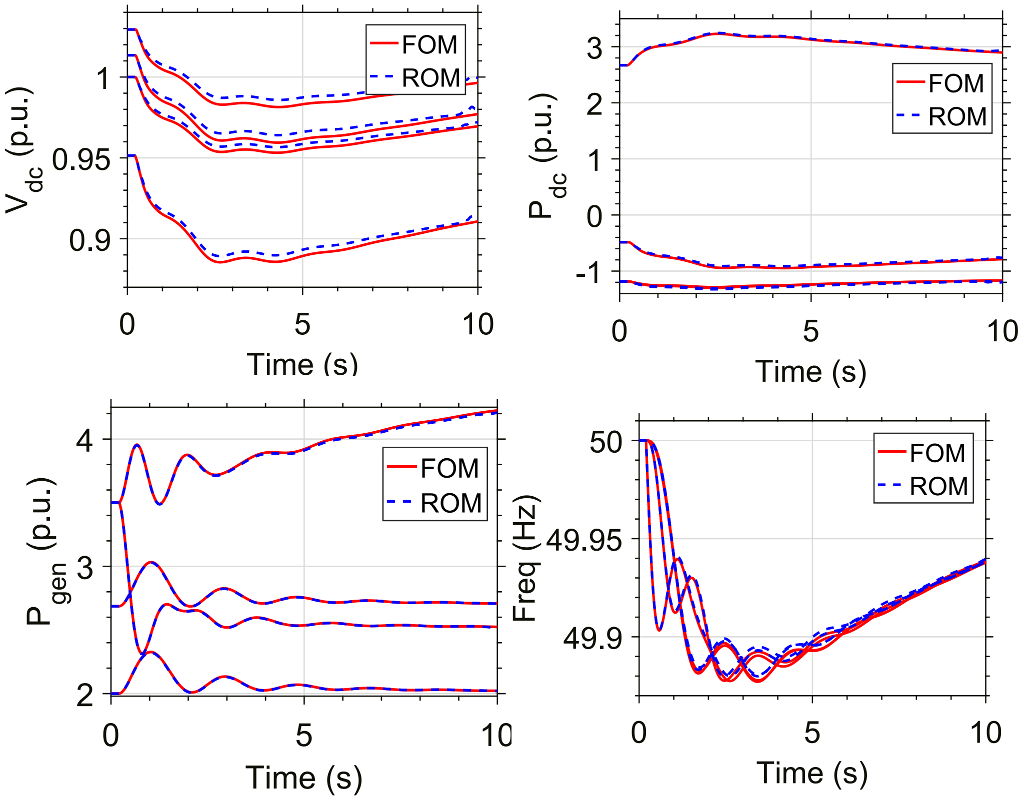

(a) Scenario CI-1: a 1.0 p.u. drop in mechanical power input of G_3

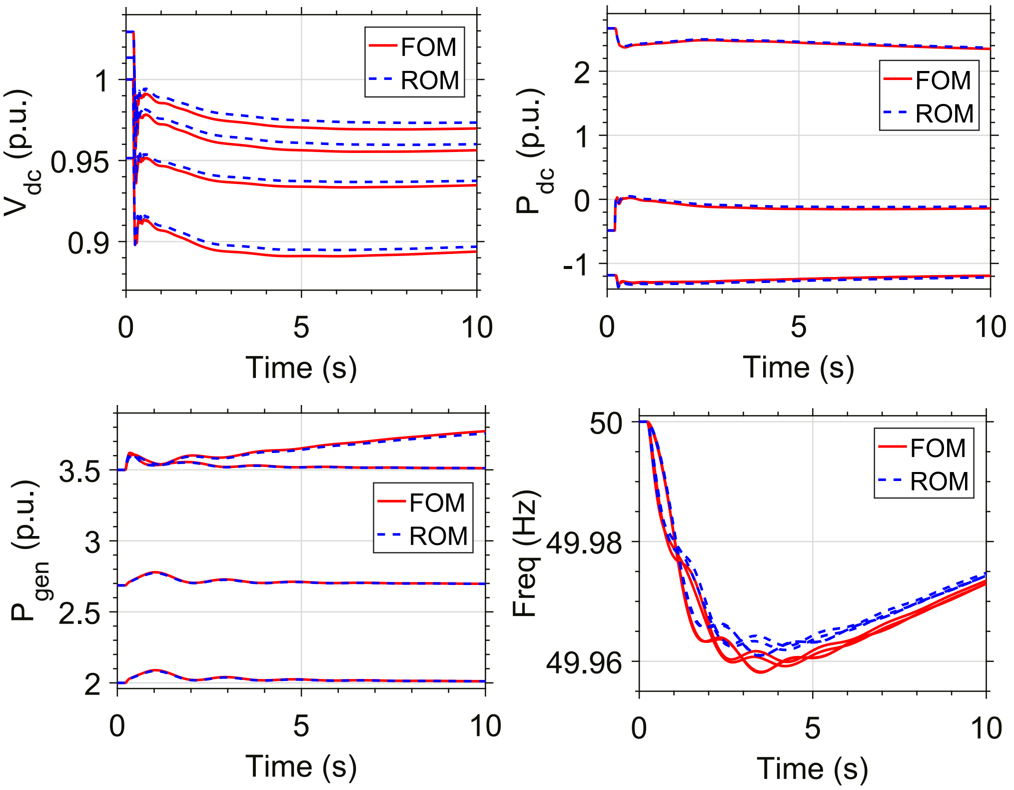

(b) Scenario CI-2: a 1.0 p.u. drop in P_s reference of converter-4

Figure 4.7: FOM vs. ROM using inertia control strategy

Table 4.3: MOR for inertia control strategy

Method	Performance	Scenario 1 (CI-1)	Scenario 2 (CI-2)
FOM	Order	2929	2929
	Elapsed time	3582.14 s	3476.23 s
ROM	Order	197	197
	Elapsed time	10.85 s	9.95 s
	MSE v_{dc}	3.20×10^{-3}	3.70×10^{-3}
	MSE P_{dc}	2.08×10^{-2}	2.40×10^{-2}
	MSE P_{gen}	5.10×10^{-3}	5.60×10^{-3}
	MSE Frequency	1.90×10^{-3}	2.10×10^{-3}

4.3 Chapter summary

This chapter has presented a comprehensive discussion on the effectiveness of the proposed MOR method applied to a four terminal MTDC system connected to two large-scale wind farms. The method has been tested under three different control configurations for the MTDC system, namely the MTDC with the slack, droop, and inertia controllers. Numerical results in all cases demonstrate that the ROMs obtained from the proposed method can accurately capture the behaviour of FOM and at the same time significantly reduce the elapsed time.

Chapter 5

Nonlinear model order reduction of wind farms

This chapter focuses on the second objective of the thesis: *To develop a nonlinear ROM of large-scale wind farm suitable for a transient or large disturbance stability study of power systems.* In Chapter 3, various linear methods have been successfully used to develop low-order models for large-scale wind farms. Chapter 4 has further extended the linear approach, namely IRKA method, to perform MOR of the wind farm models in the context of the MTDC system. However, the linearity assumption means that the model is accurate only around a predefined operating condition and to small disturbances. A natural remedy for this restriction is to use nonlinear MOR techniques to obtain an accurate ROM of wind farms.

In [107, 108], a TPWL method has been used to obtain nonlinear ROMs of integrated circuit models. The method approximates behaviour of highly nonlinear systems using a weighted combination of several linear systems, which in this thesis are called subsystems. The subsystems are obtained by linearizing the nonlinear system along a training trajectory. In [109], the method has been used to extract nonlinear macromodels of real microelectromecanical systems. In [110], an improved training scheme based on parameter sensitivity has been proposed. Further advances of TPWL method include: improved linearization point generation [111], extension to systems with nonlinear input [112], and the use of a wavelet-collocation [113].

In this chapter, the TPWL method to obtain nonlinear ROMs of DFIGs-based wind farms is proposed. Performance of linear models during a large disturbance is initially studied. Then, the TPWL model is proposed to accurately capture nonlinear behaviours of wind farms. This TPWL method uses a single training trajectory, referred to as a single TPWL method. Robustness of the single TPWL method against various types of faults is investigated to establish the extent to which the single TPWL-based ROM maintains accurate results. Finally, a new multiple TPWL method using multiple training trajectories is proposed to enhance the accuracy of the single TPWL method. This chapter is organized as follows. Sections 5.1 and 5.2 introduce a self-contained theory of single and multiple TPWL approach, respectively. This is followed by the case study on a small wind farm system in Section 5.3. Section 5.4 demonstrates the effectiveness of the TPWL method on a large-scale wind farm model. The chapter ends with conclusions in Section 5.5. The results given in this chapter have been published in the IEEE Transactions on Sustainable Energy with the title: *A Trajectory Piecewise Linear Approach to Nonlinear Model Order Reduction of Wind Farm* [114].

5.1 Trajectory piecewise linear model

This section introduces a brief narrative of the theory of TPWL approach to reduce order of the nonlinear system expressed in (3.1). A broad overview of TPWL method is given in Fig. 5.1. As can be seen, the TPWL method consists of two main stages, namely offline and online. In the offline stage, a nonlinear system response, which is called a training trajectory, is obtained by applying a disturbance to (3.1). Along this trajectory, several linearization points are selected and a set of linear subsystems are obtained at each of these points. The order of each subsystem is subsequently reduced using linear ROM techniques, such as RK [107] and BT [108], to produce initial ROMs of subsystems. This model reduction also produces the transformation matrices corresponding to each subsystem. To make the transformation matrices consistent for all subsystems, a final basis needs to be generated from them. There are two approaches for this, namely simple basis and extended basis. Using the final bases, the final ROMs of subsystems can be obtained and this process concludes the offline stage. In the online stage, the final ROMs of all subsystem are combined using weights to select the most dominant model at a particular instance t. All steps are elaborated in the subsequent

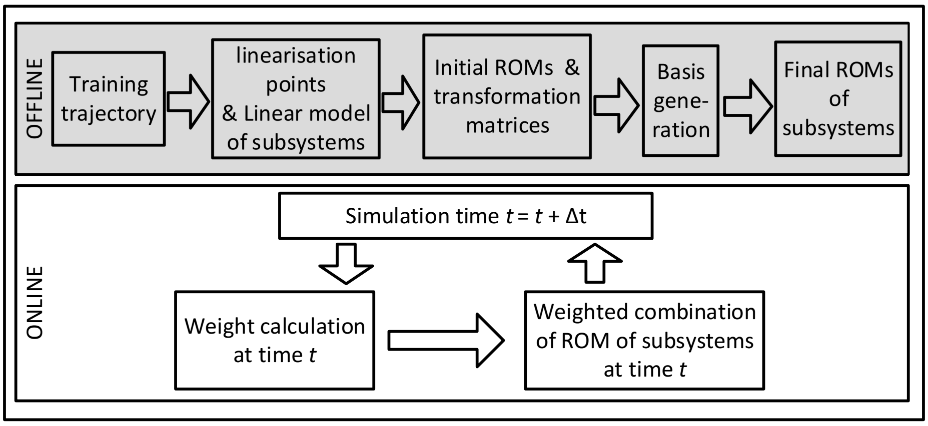

Figure 5.1: Overview of TPWL method

subsections.

5.1.1 Piecewise-linear approach

To obtain the ROM of (3.1), similar to (3.12), the states are projected onto a lower order dimensional subspace r, $r << n$, using $x(t) \approx V\hat{x}(t)$, with V satisfying $W^TV = I$. $W \in R^{n\times r}$ and $V \in R^{n\times r}$ are the transformation matrices. This yields:

$$\begin{aligned} \dot{\hat{x}}(t) &= W^T f(V\hat{x}(t), u(t)) \\ y(t) &= g(V\hat{x}(t), u(t)) \end{aligned} \tag{5.1}$$

where $\hat{x}(t)$ indicates the reduced order states. Although the states are now in the lower dimensional subspace r, $f(\cdot)$ in (5.1) is evaluated on the higher dimensional subspace n, thus it is still computationally expensive. One of remedies for this is to linearise $f(\cdot)$ and $g(\cdot)$ at the stationary points x_0 and u_0 to obtain:

$$\begin{aligned} \dot{\hat{x}}(t) &= W^T A_0 V(\hat{x}(t) - \hat{x}_0) + W^T B_0(u - u_0) \\ y(t) &= C_0 V(\hat{x}(t) - \hat{x}_0) + D_0(u(t) - u_0) \end{aligned} \tag{5.2}$$

where A_0, B_0, C_0, and D_0 represents the model of the linear system corresponding to x_0 and u_0. Although (5.2) can be evaluated efficiently, this is only valid for weak nonlinearity.

Now suppose there are s linearization points, namely $x_0 ... x_{s-1}$. Linearizing (3.1) at these points results:

$$\begin{aligned}\dot{x}(t) &= f(x_i, u_i) + A_i(x(t) - x_i) + B_i(u(t) - u_i)\\ y(t) &= g(x_i, u_i) + C_i(x(t) - x_i) + D_i(u(t) - u_i)\end{aligned} \tag{5.3}$$

Matrices $A_i,\ B_i,\ C_i$, and D_i define the linear system corresponding to x_i and in further explanations of this thesis, they will be referred as G_i for ease of referencing, i.e. $G_i \triangleq (A_i,\ B_i,\ C_i,\ D_i)$.

In the piecewise approach, the linearized systems (5.3) are combined using weights α_i to select the most dominant subsystem at the current state $x(t)$:

$$\begin{aligned}\dot{x}(t) &= \sum_{i=0}^{s-1} \alpha_i(x(t), x_i)[f(x_i, u_i) + A_i(x(t) - x_i) + B_i(u(t) - u_i)]\\ y(t) &= \sum_{i=0}^{s-1} \alpha_i(x(t), x_i)[g(x_i, u_i) + C_i(x(t) - x_i) + D_i(u(t) - u_i)]\end{aligned} \tag{5.4}$$

For numerical stability, the weights must satisfy $\sum_{i=0}^{s-1} \alpha_i(x(t), x_i) = 1$. This gives the piecewise-linear approximation of the nonlinear model in (3.1) and has an edge over the original TPWL proposed in [107], in which the system matrices B_i, C_i, D_i are constant for all x_i. Similar to (5.2), it is now possible to reduce order of (5.4) using W and V. This results:

$$\begin{aligned}\dot{\hat{x}}(t) &= \sum_{i=0}^{s-1} \alpha_i(\hat{x}(t), \hat{x}_i)[W^T f(x_i, u_i) + W^T A_i V(\hat{x}(t) - \hat{x}_i) + W^T B_i(u(t) - u_i)]\\ y(t) &= \sum_{i=0}^{s-1} \alpha_i(\hat{x}(t), \hat{x}_i)[g(x_i, u_i) + C_i V(\hat{x}(t) - \hat{x}_i) + D_i(u(t) - u_i)]\end{aligned} \tag{5.5}$$

The ROM in (5.5) can now be evaluated efficiently. It is also to be noted that from (5.5) the weights α_i are calculated from the reduced states $\hat{x}(t)$ and reduced linearization points $\hat{x}_i$, allowing more efficient weight computations.

5.1.2 Generating training trajectory and linearization points

A linearized model at x_0 remains an accurate approximation of the nonlinear system as long as the system state $x(t)$ stays sufficiently close to x_0, i.e. $\|x(t) - x_0\|_2 < \sigma$. In other words,

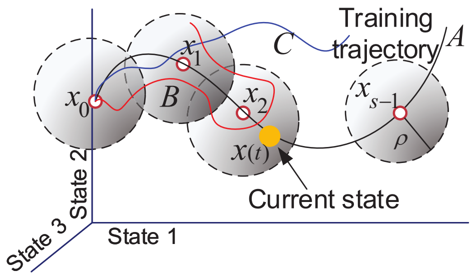

Figure 5.2: Generation of linearization points

the point x_0 should be covered by a ball with a sufficiently small radius σ. In a more general context of approximating nonlinear systems, although covering the whole space using balls may produce accurate linear system, this is essentially an impractical option and requires enormous number of linearization points.

Reference [107] suggests that the linearization points need only to be generated along a training trajectory as depicted in Fig. 5.2. Let the trajectory A be the training trajectory. A new linearization point is generated when the distance between current states $x(t)$ and all previous linearization points x_i are larger than a positive constant ρ, which basically can be selected arbitrarily small. In this way, the training trajectory is covered with balls and it is expected that the TPWL method remains accurate for any trajectory sufficiently close to the training trajectory, e.g. trajectory B. When this assumption is violated, e.g. trajectory C, the TPWL method produces incorrect dynamics of the nonlinear systems. The detailed of linearization point generation is given in Algorithm 1.

In order to generate the training trajectories, practical experience from system operators comes into consideration. The training trajectories are the nonlinear response of a system following the most common fault, severe fault, or other types of contingencies that are of particular interest for system operators. As the system is perturbed by faults of interest, the time series data is recorded. This data is the basis for generating linearization points discussed in the next subsection.

Algorithm 1: Generating linearization points

Input: Training trajectory $x^{train}(t)$, number of linearization points s, constant $\rho > 0$
Output: linearization points $x_i = [x_0 \cdots x_{s-1}]$
Initialize: $i = 0$, $x_i = x^{train}(0)$, $0 < d_k < \rho$
while $i < s - 1$ **do**
  while $d_k < \rho$ **do**
    $d_k = \min_{0 \le j \le i} \|x^{train}(k) - x_j\|_2 / \|x_j\|_2$
    $k = k + 1$
  end while
  $x_i = [x_i \;\; x^{train}(k)]$
  $k = 0$, $0 < d_k < \rho$, $i = i + 1$
end while

$x^{train}(t) = [x^{train}(0),\ x^{train}(1),\ \cdots]$ is a time series of the training trajectory.

5.1.3 Linearization and basis generation

Linearization of (3.1) is performed at linearization points to obtain subsystems as in (5.3). Again, due to the fact that order of wind farm is extremely high, this step is performed numerically by using *linearize* command in Matlab® as already given in Section 3.1.

The subsequent step is to reduce the orders of subsystems and to generate the final basis, V and W, as given in (5.5). There are two approaches for this, namely simple basis and extended basis. Both methods construct the matrices from transformation matrices corresponding to all subsystems, i.e. V_i and W_i, however the latter has a richer basis, and hence produces more accurate results. The details are elaborated as follows.

Having obtained the subsystems G_i from (3.2), their respective orders are firstly reduced using IRKA method [76, 88]:

$$[\hat{A}_i, \hat{B}_i, \hat{C}_i, \hat{D}_i, V_i, W_i] = \mathrm{IRKA}(A_i, B_i, C_i, D_i), \tag{5.6}$$

where $\hat{A}_i = W_i^T A_i V_i$, $\hat{B}_i = W_i^T B_i$, $\hat{C}_i = C_i V_i$, $\hat{D}_i = D_i$. $\hat{G}_i \triangleq (\hat{A}_i,\ \hat{B}_i,\ \hat{C}_i,\ \hat{D}_i)$ is the ROM of subsystem G_i with the corresponding transformation matrices V_i and W_i. Equation (5.6) represents the iterative procedure of IRKA method in Algorithm 6 (see Appendix A). This is a novel approach compared to [107, 108] in which the RK and BT method have been respectively used. The RK used in [107] only approximates the system at low frequency ranges. This may lead to incorrect results in the case of wind farm due to the fact that the dominant dynamics of a typical wind farm are often located at medium frequency ranges [57]. Although the BT method [108] can overcome this problem, this would lead to extremely expensive computations for wind farm application as previously demonstrated in Chapter 3. Hence, the IRKA is preferred since it is able to provide more accurate ROM around the frequency of dominant modes at much lower computational cost than the BT. A brief discussion on the IRKA method is given in Subsection 3.2.7.

In the extended basis, the matrices V_i and W_i are firstly augmented column-wise as follows:

$$\begin{aligned} V_{\text{aug}} &= [V_0 \; V_1 \; \cdots V_{s-1}] \\ W_{\text{aug}} &= [W_0 \; W_1 \; \cdots W_{s-1}] \end{aligned} \tag{5.7}$$

The columns of V_{aug} and W_{aug} which are nearly linearly dependent should be removed with the aim to enhance numerical conditioning. This is readily done through singular value decomposition (SVD) of V_{aug} and W_{aug} as shown below:

$$\begin{aligned} [U_v, \Sigma_v, V_v] &= \text{SVD}(V_{\text{aug}}) \\ [U_w, \Sigma_w, V_w] &= \text{SVD}(W_{\text{aug}}) \end{aligned} \tag{5.8}$$

The new matrices V_{new} and W_{new} are taken from the columns of U_v and U_w corresponding to sufficiently large singular values of Σ_v and Σ_w, respectively. Suppose there are r large singular values, then the first r columns of U_v and U_w are selected as follows:

$$\begin{aligned} V_{\text{new}} &= U_v(1:r,:) \\ W_{\text{new}} &= U_w(1:r,:) \end{aligned} \tag{5.9}$$

The last step is to biorthogonalize V_{new} and W_{new} using:

$$\begin{aligned} [U_{\text{bior}}, \Sigma_{\text{bior}}, V_{\text{bior}}] &= \text{SVD}(W_{\text{new}}^T V_{\text{new}}) \\ V &= V_{\text{new}} V_{\text{bior}} \Sigma_{\text{bior}}^{-1/2} \\ W &= W_{\text{new}} U_{\text{bior}} \Sigma_{\text{bior}}^{-1/2} \end{aligned} \tag{5.10}$$

It is obvious from (5.10) that $W^T V = I$.

On the other hand, the simple basis is obtained by only using the V_0 and W_0 in (5.7):

$$\begin{aligned} V &= V_0, \\ W &= W_0 \end{aligned} \tag{5.11}$$

Since V_0 and W_0 from the IRKA method are already biorthogonal, step (5.8) to (5.10) can be skipped.

5.1.4 Weight calculation

The weights $\alpha_i(\cdot)$ select the closest subsystem $\hat{G}_i$ to the current states $x(t)$ by measuring the euclidean distances between the current state $x(t)$ and the linearization points x_i. The weight calculation is part of online stage of the algorithm and it is recalculated for every time step during the course of simulation, see Fig. 5.1. The detail calculation is given in Algorithm 2.

It can be readily seen that when x_i is the closest point to $x(t)$, the corresponding weight $\alpha_i(\cdot)$ immediately becomes close to unity, while the weights of other points are approximately zero. This transition behaviour is governed by β, which is set to 25 in this thesis [107]. The weight calculations in Algorithm 2 can be performed efficiently, thus adds up only negligible cost of computation for overall TPWL algorithm.

Algorithm 2: Weight calculation

Input: current state $x(t)$ and linearization points x_i

Output: Weights α_i

1: Calculate the minimum distance,
$m = \min\ d_i = \min\ \|x(t) - x_i\|_2, i = 0 \cdots s-1$

2: Calculate the weights,
$\alpha_i = \hat{\alpha}_i / \sum_{j=0}^{s-1} \hat{\alpha}_j$, where $\hat{\alpha}_i = e^{-\beta d_i/m}, \beta = 25$

5.2 Multiple TPWL method

The single TPWL approach presented in the previous section is obtained by using a single training trajectory. As it will be demonstrated in Subsection 5.3.4, when a fault differs significantly from the one used to generate the training trajectory, the single TPWL may often produce inaccurate results.

In order to enhance performance of the single TPWL, this section proposes the multiple TPWL method obtained from multiple training trajectories. This approach is illustrated in Fig. 5.3. Let M be the number of training trajectory. First for each training trajectory, the linearization points are generated according to Algorithm 1. Assume that there are in total j linearization points for all trajectories ($j = s_1+s_2+...+s_M$ with s_i = the number of linearization points along the training trajectory i). It might be possible that some linearization points from different training trajectories become close to each other. Thus, they can be represented by a single point, see the shaded region in Fig. 5.3. The k-means clustering offers a simple way to find these imminent linearization points using a silhouette value [115]:

$$S_i = \frac{b_i - a_i}{\max\{a_i, b_i\}}, \text{ with } -1 \leq S_i \leq 1, \; i = 1, 2, ...j. \tag{5.12}$$

where S_i is the silhouette value for the linearization point x_i, a_i denotes the average distance between x_i and other points within the same cluster as x_i, and b_i is the minimum average distance between point x_i and all other points which are not in the same cluster as x_i. If a_i is small (S_i is close to 1), then x_i is assigned to a correct cluster. Likewise if b_i is small (S_i is

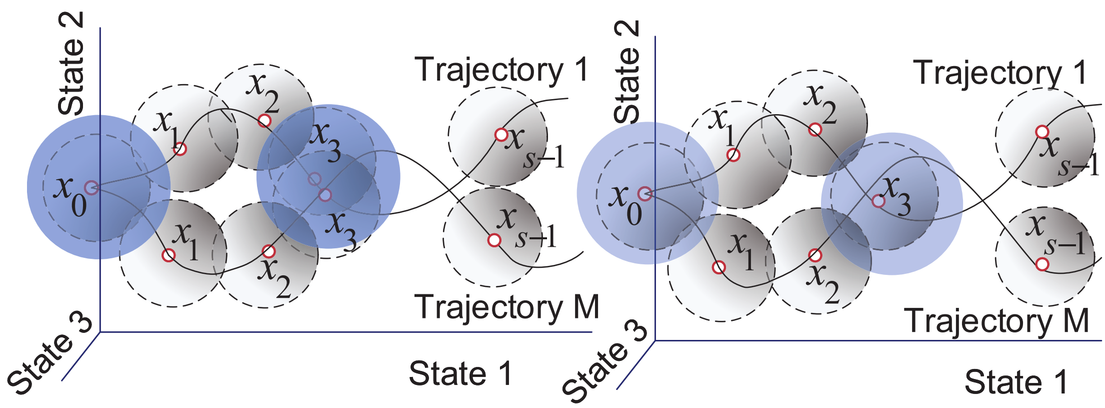

Figure 5.3: Multiple TPWL method

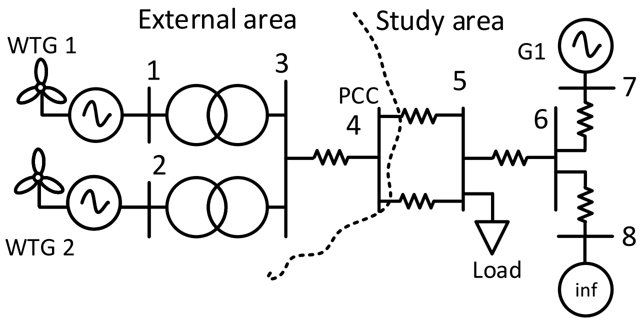

Figure 5.4: Small wind farm connected to external grid

close to -1), then x_i should be assigned to other cluster. Hence, by investigating the silhouette value, a proper number of cluster can be selected. Once a group of imminent points are found, they are replaced with a single point closest to its centroid/centre, so reducing the number of linearization points.

5.3 Case study on a small wind farm model

This section is devoted to study the effectiveness of TPWL method to obtain a nonlinear ROM of a small wind farm model. The section is divided into five subsections. First, the wind farm system and ROM approach are described in Subsection 5.3.1. Subsection 5.3.2 presents a step-by-step procedure of obtaining a ROM using the TPWL method using the simple basis and compares its performance with those from linear models following a large disturbance. Subsection 5.3.3 investigates accuracy of TPWL method using the simple and extended basis. Robustness of the TPWL method against various types of faults is examined in Subsection 5.3.4. Finally, accuracy of the multiple TPWL method proposed in Section 5.2 is studied in Subsection 5.3.5.

5.3.1 ROM approach

Fig. 5.4 illustrates the small wind farm system used to investigate the effectiveness of TPWL method to obtain the nonlinear ROM. As can be seen, it is a 2×5 MW doubly-fed induction generator (DFIG)-based wind farm connected to an external grid, which mainly consists of a synchronous generator represented using a transient model, load, and infinite bus. The DFIG is modeled using a 22^{nd} order model and network components such as transformers, lines, and cables are represented using a fourth order model as given in Section 2.1. This system has a total order of 84 and is modelled in Matlab/ Simulink®. Parameters of the system are provided in Appendix C. It is to be noted that this system is oversimplified and only used to demonstrate performance of the TPWL method.

To obtain a nonlinear ROM, the wind farm in Fig. 5.4 is divided into two areas, namely *study-area* and *external-area*. The wind farm is considered as the *external-area* and the *study-area* consists of the rest of components such as the load, generator, and infinity bus as illustrated in Fig. 5.4. It turns out that the orders of the *external-area* and *study-area* are 60 and 24, respectively. The former is then reduced using the TPWL method, while the latter is maintained using the original nonlinear equations. The real and imaginary components of the PCC voltage (V_q^{pcc} and V_d^{pcc}) and PCC current (I_q^{pcc} and I_d^{pcc}) are respectively selected as the inputs and outputs of the *external-area*, while the opposite variables, namely PCC current (I_q^{pcc} and I_d^{pcc}) and PCC voltage (V_q^{pcc} and V_d^{pcc}), are respectively used as the inputs and outputs of the *study-area*. The validation is carried out by comparing the PCC real and reactive power obtained from FOM and ROM following a disturbance at the *study-area*. The accuracy of the ROM is measured using a mean squared error (MSE) as given in (3.3).

5.3.2 Performance of TPWL method during a large disturbance

This subsection investigates performance of the TPWL method following a large disturbance. Responses of this method are compared to those obtained from the nonlinear FOM. To more clearly appreciate the effectiveness of the TPWL method, responses from linear FOM and ROM using IRKA method are also given.

The linear FOM is obtained by linearizing the *external-area* at the stationary point using *linearize* command, while the ROM using IRKA is produced from order reduction of linear FOM using the IRKA method. As in Subsection 3.2.8, an appropriate order of IRKA is found by trying several different orders and comparing their accuracy to the linear FOM. Three cases of ROMs, namely orders 10, 16, and 26, are tested. The triplet $\{\sigma_j, r_j, l_j\}$ in Appendix A.4 are initialized randomly for all ROMs and ϵ is set to 1.0×10^{-3}. With these parameters, the IRKA

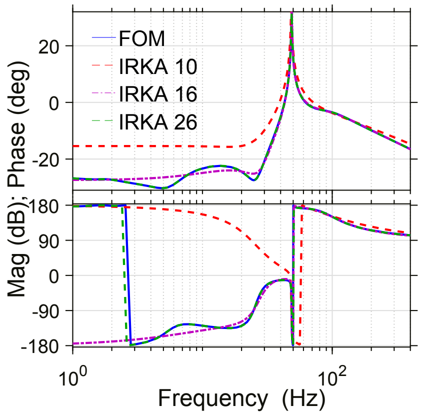

Figure 5.5: Bode plot of *external-area* from V_q^{pcc} to I_q^{pcc}: FOM vs. ROMs using IRKA

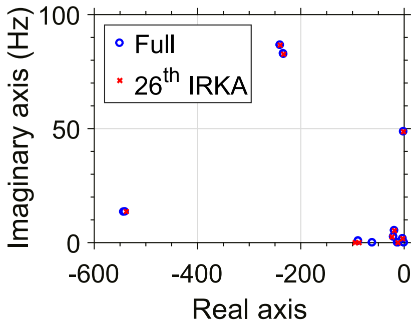

Figure 5.6: Mode preservation of the *external-area* using the 26$^{\text{th}}$ order IRKA

converges after 89, 23, and 27 iterations for orders 10, 16, and 26, respectively. The results are depicted in Fig. 5.5. It is obvious that although all ROMs can capture the significant peak of Bode magnitude plot at around 48.66 Hz, only the 26$^{\text{th}}$ order can produce a more accurate response over wider spectrum. Hence, it is used for further analysis.

Fig. 5.6 shows that mode preservation by the 26$^{\text{th}}$ order IRKA. All modes with relatively low damping factors are retained in the ROM. These modes are mostly related to the PLL controller and LCL filter states. There is also preservation of the critical mode at 48.66 Hz, which coincides the significant peak of Bode magnitude plot in Fig. 5.5. The modes with higher damping factors can also be captured by increasing the order of IRKA method.

To execute the TPWL method, the procedure in Fig. 5.1 is followed. Firstly, the wind farm is perturbed with a 5% step change in the excitation voltage reference of G1 at $t = 0.02$ s to generate the training trajectory and the simulation is performed for 2 s. The constant ρ in Algorithm 1 is set to 3×10^{-5}, which consequently generates 5 linearization points at $t = 0$ s, 0.11 s, 0.22 s, 0.38 s, and 0.65 s. The wind farm model is linearized at these points to obtain

Table 5.1: Linear vs. nonlinear model

Model	Order	MSE P_{PCC}	MSE Q_{PCC}
Linear FOM	84	1.33×10^{-5}	3.66×10^{-6}
Linear IRKA	50	1.35×10^{-5}	3.79×10^{-6}
TPWL	50	1.01×10^{-6}	8.55×10^{-7}

the subsystems. For easy reference, the subsystem is indicated by a subscript corresponding to the time of linearization. For example, G_0 and $\hat{G}_{0.11}$ denote FOM of subsystem obtained at t=0 s and ROM of subsystem obtained at t=0.11 s, respectively. G_0 corresponds to the stationary point, and hence is exactly the same as the linear FOM. Following this, the IRKA method is used to reduce the orders of all subsystems, which based on the previous observation, are set to 26. The last step in the offline stage is the basis generation. Here, it is carried out by the simple basis, which means that the transformation matrices V and W are taken from the matrices corresponding to the subsystem at t= 0 s, namely V_0 and W_0, as given in (5.11). All FOM of subsystems are then reduced using V and W as indicated in (5.5). The final ROMs of subsystems are combined using different weight distribution during simulation, and hence the order of the final model of TPWL is also 26. In the form of the weighted state-space in (5.5), the final TPWL model is given as follows:

$$\begin{aligned}\dot{\hat{x}}(t) &= \sum_{i=0}^{4} \alpha_i(\hat{x}(t), \hat{x}_i)[\hat{f}(x_i, u_i) + \hat{A}_i(\hat{x}(t) - \hat{x}_i) + \hat{B}_i(u(t) - u_i)] \\ y(t) &= \sum_{i=0}^{4} \alpha_i(\hat{x}(t), \hat{x}_i)[g(x_i, u_i) + \hat{C}_i(\hat{x}(t) - \hat{x}_i) + \hat{D}_i(u(t) - u_i)]\end{aligned} \tag{5.13}$$

where index i = 0, 1, 2, 3, and 4 corresponds to t= 0 s, 0.11 s, 0.22 s, 0.38 s, and 0.65 s, respectively.

Once all representations of the *external-area* are obtained, they are reconnected to the *study-area*. The orders of overall systems with linear FOM, ROM using IRKA, and ROM using TPWL are 84, 50 and 50, respectively (see Table 5.1). The time-domain simulation is performed by perturbing the systems with the same fault used to generate the training trajectory. The responses of P_{pcc} and Q_{pcc} are shown in Fig. 5.7. It is obvious that although shortly after the fault, the linear FOM is able to capture the initial oscillations of the nonlinear FOM, its

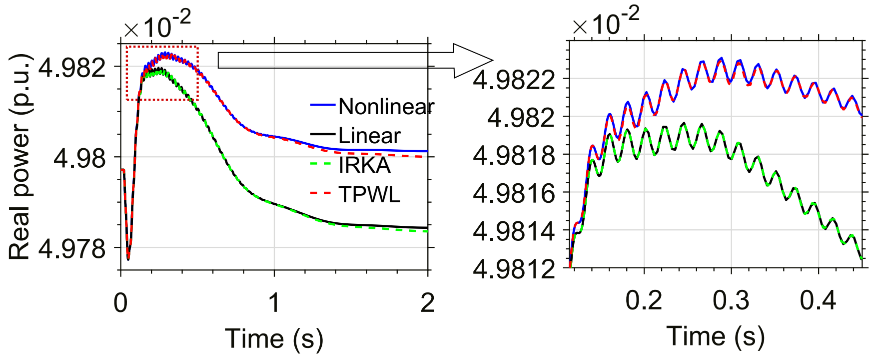

(a) Active power at PCC

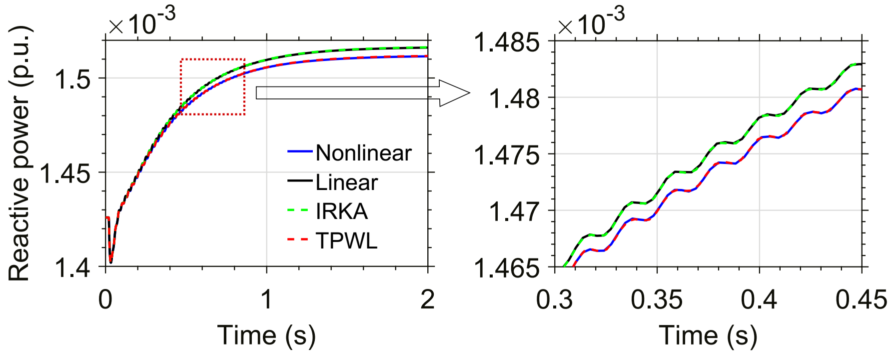

(b) Reactive power at PCC

Figure 5.7: Performance of the several models during a large disturbance

response deteriorates and eventually becomes inaccurate. It is because the operating condition deviates further away from the stationary point where the linear FOM is obtained from the nonlinear FOM. The ROM using IRKA derived from this model will consequently carry forward the errors. As given in Table 5.1, the corresponding MSE values of P_{pcc} for the linear FOM and ROM using IRKA are 1.33×10^{-5} and 1.35×10^{-5}, respectively, while the MSE values of Q_{pcc} for the linear FOM and ROM using IRKA are 3.66×10^{-6} and 3.79×10^{-6}, respectively.

Fig. 5.7 also demonstrates that the TPWL method with the simple basis produces a more accurate estimate of the nonlinear FOM responses. The corresponding MSE values for this model as listed in Table 5.1 are 1.01×10^{-6} and 8.55×10^{-7} for P_{pcc} and Q_{pcc}, respectively, which are smaller than those from the linear-based models. The superior performance of the TPWL method stems from the fact that the dominant subsystems are given higher values of weights as the system dynamic evolves, whereas less dominant subsystems have weights close to zero. To see this, the trajectories of all weights during the course of simulation are depicted in Fig. 5.8. From $t = 0$ s to $t = 0.1$ s the first weight α_0 related to $\hat{G}_0$ has unity value, while others

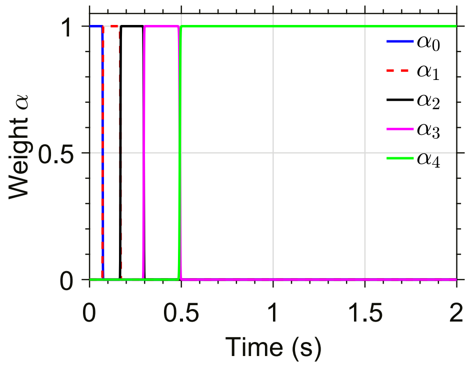

Figure 5.8: Trajectory of all weights during the simulation

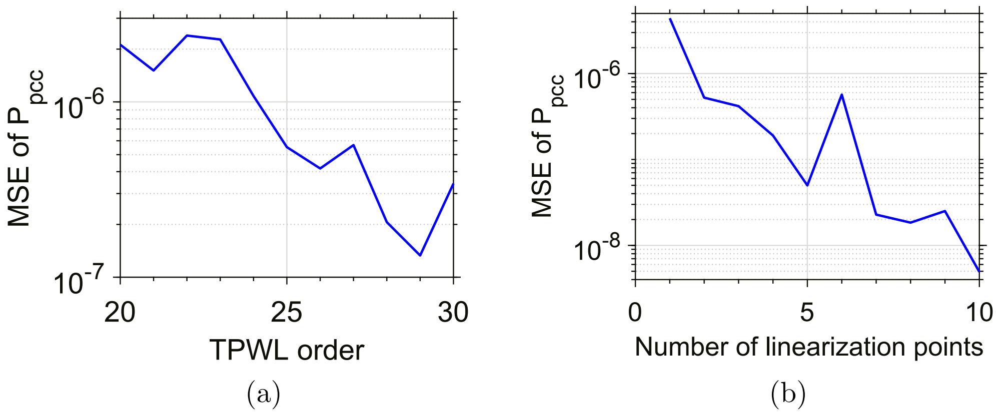

Figure 5.9: TPWL-based accuracy due to: (a) system order and (b) number of linearization points

are zeros, implying that the subsystem obtained at stationary point is dominant during this period. This explains the reason for the linear-based methods maintaining accurate responses for a short period of time after the fault. After $t = 0.1$ s, α_0 drops to zero, and α_1 to α_4 increase alternately to unity until the end of simulation, indicating that both $\hat{G}_{0.11}$ and $\hat{G}_{0.65}$ are dominant in this interval.

Furthermore, to study the impact of TPWL order and number of linearization points on the accuracy of TPWL, these factors are varied and the MSE of P_{pcc} is calculated. The results are depicted in Fig. 5.9. It is apparent that both factors affect the accuracy of TPWL method, although the number of linearization points has a significantly more appreciable impact. More specifically, from Fig. 5.9a as the order is varied from 20 to 30, the MSE drops slightly by a factor of around 10, whereas Fig. 5.9b shows that there is a considerable drop in the MSE by a factor of around 1000 when the order is varied from 1 to 10. It is also noticeable that when both factors are increased, the error sometime goes up; which is expected as the IRKA solves only suboptimal solution of (3.31). However the general trend indicates that there is reduction in the error as these factors are increased.

5.3.3 Simple versus extended basis

This subsection compares performances of the TPWL method obtained using two approaches to construct the transformation matrices, V and W, namely the simple and extended basis. For this purpose, the training trajectory is now produced by perturbing the system with a 40% voltage drop at the infinite bus and the constant ρ is set to 2.5×10^{-3}, which produces 30 linearization points. Following this, the subsystems are obtained by linearizing the nonlinear system at these points and each subsystem is reduced using the IRKA method. Recall from Subsection 5.1.3, the main difference between the simple and extended basis is the construction of V and W. The former constructs V and W from V_0 and W_0, which are associated with the subsystem at the stationary point G_0. Again, the IRKA of order 26 is used, and therefore the order of TPWL model is also 26. In contrast, the latter uses all matrices corresponding to all subsystems and performs calculations (5.7) to (5.10) to construct V and W. In (5.9), r is set to 32; hence this produces a TPWL model of order 32.

To study their performance in the time domain, the systems are perturbed with the same fault used to excite the training trajectory. The responses of P_{pcc} and Q_{pcc} are depicted in Fig. 5.10. As also evident from Table 5.2, the accuracy of extended basis (MSE of $P_{\text{pcc}}= 3.66\times10^{-4}$ and MSE of $Q_{\text{pcc}}= 2.15\times10^{-4}$) is higher than in the simple basis (MSE of $P_{\text{pcc}}= 1.11\times10^{-3}$ and MSE of $Q_{\text{pcc}}= 4.05\times10^{-3}$). This increase in accuracy is a consequence of using richer transformation matrices V and W.

It is extremely essential to discuss the stability preservation of TPWL method. It is noted based on the experiments that by using the simple basis, the TPWL method is always stable when all ROMs of the subsystems are stable. However, whenever the extended basis is used, an unstable TPWL model is sometimes found out of stable ROMs of subsystems. This problem can often be resolved by varying the order of TPWL, i.e. r, in (5.9). Specially, the order r is initially set to the order of ROMs of subsystems. The stability of all ROMs of subsystems is then checked. If an unstable subsystem is found, r is increased until all subsystems are stable.

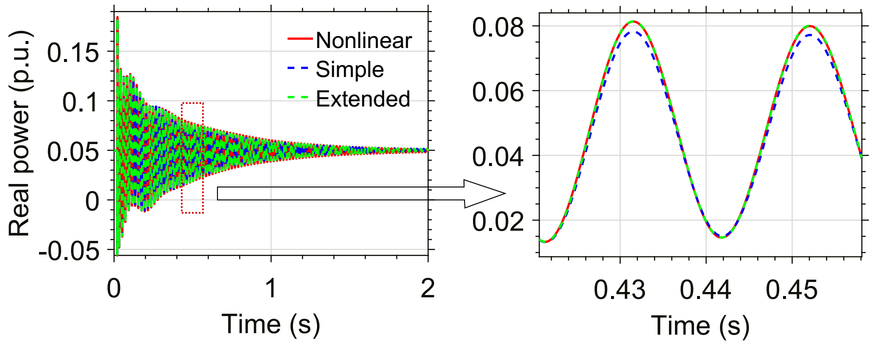

(a) Active power at PCC

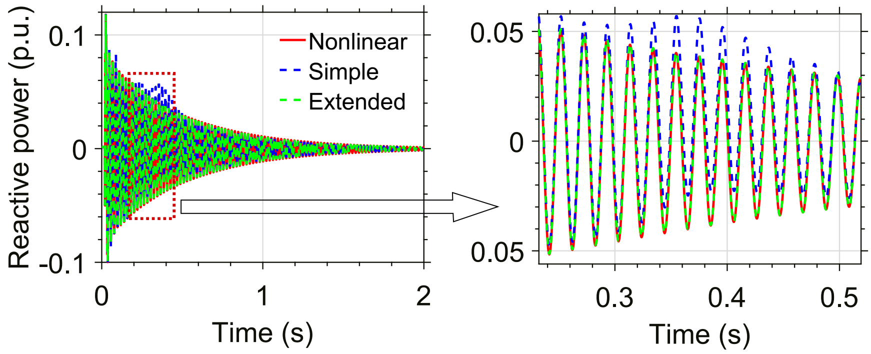

(b) Reactive power at PCC

Figure 5.10: Comparison between simple and extended basis

Table 5.2: Simple vs. extended basis

Model	Order	MSE P_{PCC}	MSE Q_{PCC}
TPWL simple	50	1.11×10^{-3}	4.05×10^{-3}
TPWL extended	56	3.66×10^{-4}	2.15×10^{-4}

5.3.4 Robustness against different type of faults

From Subsections 5.3.2 and 5.3.3, one may notice that the approach has an obvious concern, namely the training trajectory is only generated from a single fault. Furthermore, the fault considered to examine performance of the TPWL method is exactly the same as the one used to generate the training trajectory. Hence, it raises a question: *how robust is the TPWL method when subjected to faults which are different from the one used to generate the training trajectory?* It is natural to have this question since in practice any type of fault might happen. The answer to this question provides the extend to which the results from TPWL method remain reliable.

To investigate this, the previous TPWL models used in Subsection 5.3.3, both the simple (order

Table 5.3: Fault scenario for single TPWL method

Case	Fault
CS-1	1.0% step in infinite bus voltage
CS-2	39% drop in infinite bus voltage
CS-3	60% drop in infinite bus voltage
CS-4	5.0% step in excitation voltage reference of G1

26) and extended basis (order 32), are again considered. Recall that the training trajectory is obtained from the 40% voltage drop in the infinite bus voltage. Four scenarios of faults given in Table. 5.3 are arranged to test robustness of the method. The CS-1 studies accuracy of the TPWL model when the system is perturbed with a 1% step in the infinite bus voltage, which is close to the stationary point, whereas in the CS-2, the TPWL models are subjected by a drop of 39%, which is very similar to the training trajectory. CS-3 and CS-4 simulate the models when the faults are significantly different from conditions in both the training trajectory and stationary point.

Fig. 5.11 illustrates the results of P_{pcc} in all cases. It is noticeable that the ROM obtained from the TPWL method predicts accurately the responses of FOM in CS-1 and CS-2, in which the faults are similar to the one to excite the training trajectory and close to the stationary point.

According to Table 5.4, the MSE values for simple and extended basis in CS-1 are 1.68×10^{-3} and 1.31×10^{-3}, respectively, whereas the MSE values for simple and extended basis in CS-2 are 1.15×10^{-3} and 5.54×10^{-4}, respectively. The erroneous results, nonetheless, are produced when the TWPL method is subjected to a fault which is very different from that is used to generate the training trajectory or far away from the stationary point as respectively given in CS-3 and CS-4. Specially, in CS-3, the simple basis basically becomes unstable approximately after $t = 0.15$ s. The MSE value in CS-3 is 7.75×10^{-3} for the extended basis, while the MSE values in CS-4 are 1.35×10^{-5} and 1.33×10^{-5} for the simple and extended basis, respectively.

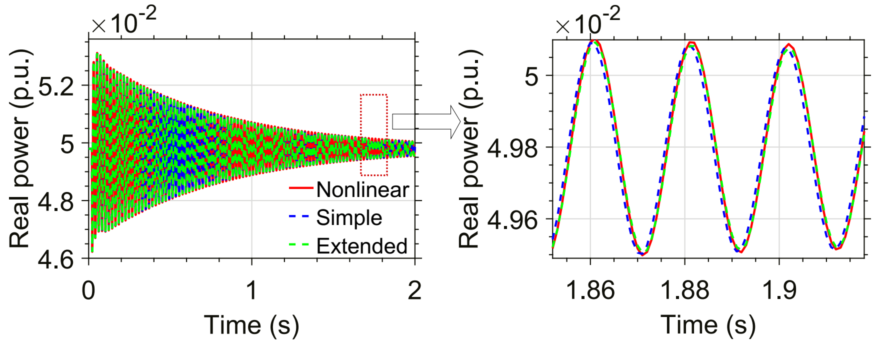

(a) Real power at PCC in CS-1

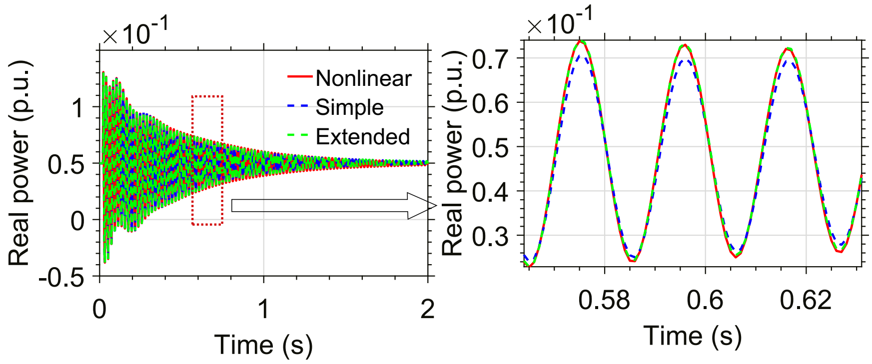

(b) Real power at PCC in CS-2

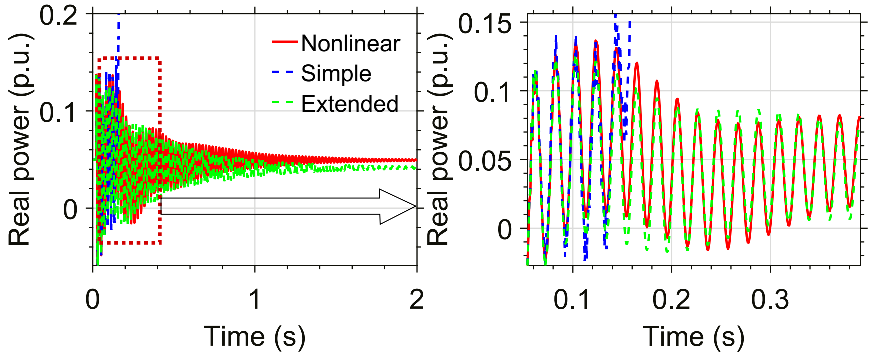

(c) Real power at PCC in CS-3

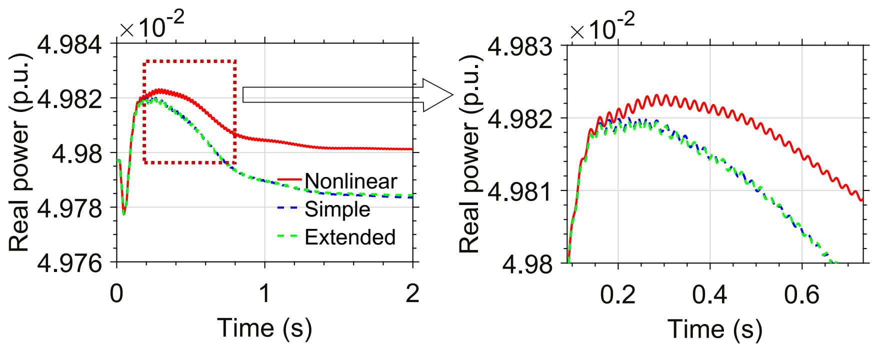

(d) Real power at PCC in CS-4

Figure 5.11: Robustness of single TPWL method

Table 5.4: Robustness of TPWL method

Case	Method	Order	MSE P_{PCC}
CS-1	Simple	50	1.68×10^{-3}
	Extended	56	1.31×10^{-3}
CS-2	Simple	50	1.15×10^{-3}
	Extended	56	5.54×10^{-4}
CS-3	Simple	50	unstable
	Extended	56	7.75×10^{-3}
CS-4	Simple	50	1.35×10^{-5}
	Extended	56	1.33×10^{-5}

5.3.5 Performance of multiple TPWL method

As evident from Subsection 5.3.4, accurate results of the single TPWL method are obtained only during two conditions of faults, namely close to the training trajectory and stationary point. These conditions are restricted for a practical use because a fault may be completely different from both conditions. This section addresses this problem to enhance the performance of TPWL method using the multiple TPWL method proposed in Section 5.2.

In order to generate multiple training trajectories, the system is subjected with step faults at the infinite bus voltage with the magnitudes of ±30% and ±40%, and at the excitation voltage reference of G1 with the magnitudes of ±10%. The values of ρ are set to 2.5×10^{-3} and 3.0×10^{-5} for the faults at the infinite bus and excitation voltage reference of G1, respectively. This generates a total of 102 linearization points, which are subsequently reduced to 97 points using k-means clustering. An appropriate number of clusters is obtained by using the silhouette value in (5.12). It is found that a further reduction below 97 points affects accuracy of the TPWL method. Once the linearization points are obtained, the nonlinear FOM is linearized at these points. The orders of subsystems are then reduced to 26 using the IRKA method. The final basis is constructed by using the extended basis and r in (5.9) is set to 32, which yields the final multiple TPWL model with an order of 32.

To see the advantages of multiple TPWL, three different cases as given in Table 5.5 are studied. The faults in all cases are not used to generate the training trajectory. The responses of P_{PCC} obtained using multiple TPWL and IRKA methods for CM-1 to CM-3 are given in Fig. 5.12.

Table 5.5: Fault scenario for multiple TPWL method

Case	Fault
CM-1	50% step in infinite bus voltage
CM-2	−50% drop in infinite bus voltage
CM-3	5.0% faults in excitation voltage reference of G1

Table 5.6: Performance of multiple TPWL

Case	Method	Order	MSE P_{PCC}
CM-1	IRKA	50	7.54×10^{-1}
	Multiple TPWL	56	3.30×10^{-3}
CM-2	Simple	50	1.41×10^{-2}
	Extended	56	2.80×10^{-3}
CM-3	Simple	50	1.35×10^{-5}
	Extended	56	5.54×10^{-7}

One can see that although the faults to test the ROM are not used to generate the training trajectory, the multiple TPWL method gives accurate estimates of the P_{PCC} responses in all cases, while IRKA method produces more erroneous waveforms. This indicates the fact that the multiple TPWL method can be valid for wider range of faults. The MSE values are 3.30×10^{-3}, 2.80×10^{-3}, and 5.54×10^{-7} for CM-1, CM-2, and CM-3, respectively (see Table 5.6).

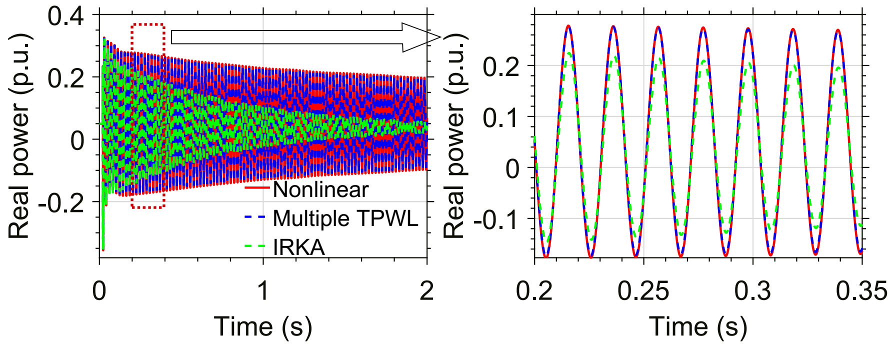

(a) Real power at PCC in CM-1

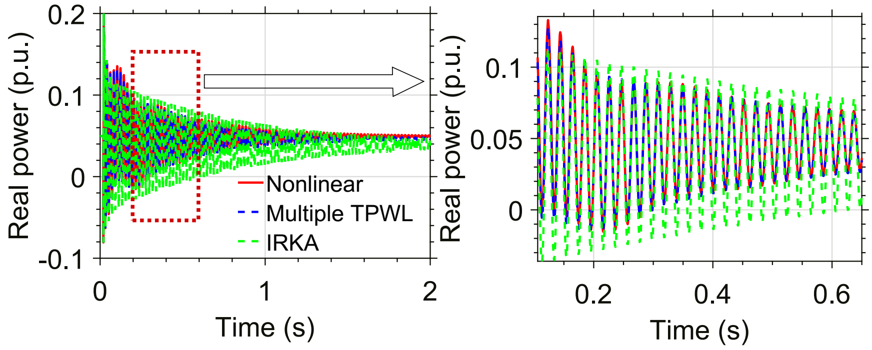

(b) Real power at PCC in CM-2

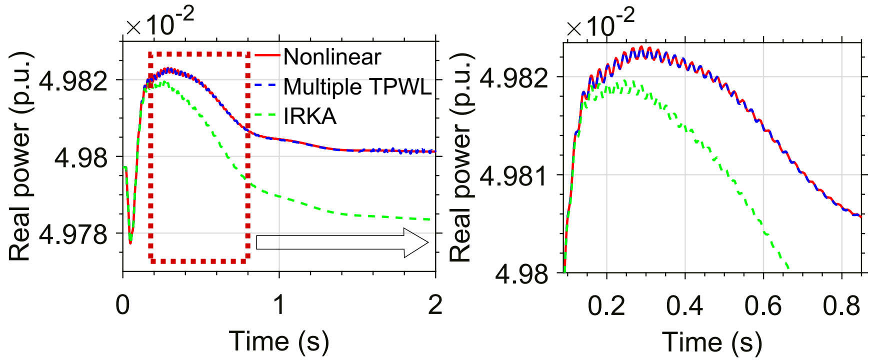

(c) Real power at PCC in CM-3

Figure 5.12: Robustness of multiple TPWL method

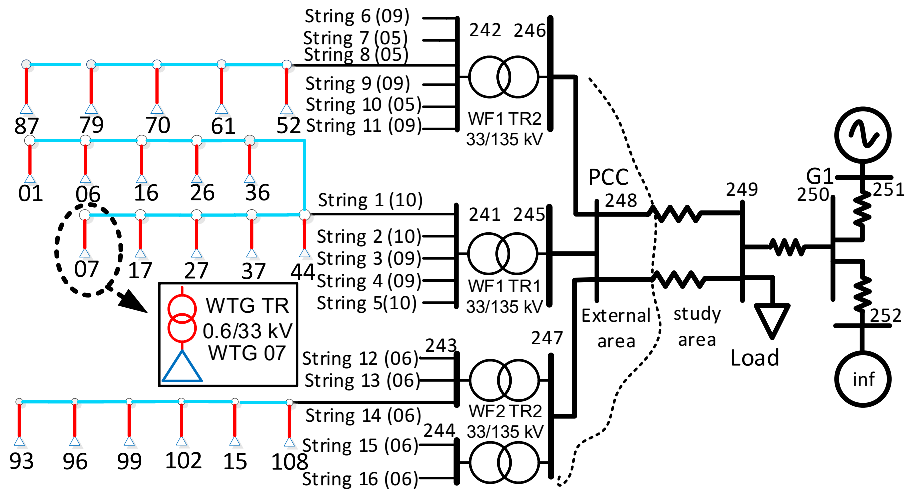

Figure 5.13: Large-scale wind farm with 120 DFIGs connected to external grid

5.4 Case study on a large-scale wind farm model

In this section, the robustness of the multiple TPWL method to obtain a ROM of a large-scale wind farm is investigated. To do this, the *external-area* of Fig. 5.4 is replaced with the wind farm consisting of 120 DFIGs as shown in Fig. 3.1, while the *study-area* from the previous study is retained. The modified test system is illustrated in Fig. 5.13. With this new configuration, the order of *external-area* becomes 3868, while the order of *study-area* is identical to that in the previous case, i.e. 24. The incoming free wind speed and direction for the wind farm is respectively set to 14 m/s and 0° (see Section 3.1).

The multiple training trajectories are generated by perturbations at the infinite bus and excitation voltage reference of G1. The types of perturbations, values of ρ, and number of linearization points for each trajectory are given in Table 5.7. As can be seen, the total of linearization points is 168, which is then reduced to 163 using the k-means clustering. A further reduction below

Table 5.7: Multiple training trajectory generation

Fault		ρ	Number of linearization points
Type	Location		
-1.0% and 1.0%	Exc. of G1	2.00×10^{-4}	14 and 11
-10.0% and 10.0%	Inf. bus	3.50×10^{-4}	33 and 27
-20.0% and 20.0%	Inf. bus	6.00×10^{-4}	51 and 32

Table 5.8: Fault scenario for a large wind farm

Case	Fault
CL-1	−20% step in infinite bus voltage
CL-2	Line trip between bus 248 and 249
CL-3	−25% step in infinite bus voltage

163 points degrades the performance of TPWL method. The nonlinear system is linearized at these points to generate the subsystems and the IRKA method is used to reduce the order of the subsystems from 3868 to 36. The constant r in (5.9) is set to 36, yielding a reduced model with an order of 36.

The multiple TPWL method is tested under three scenarios, CL-1 to CL-3, as indicated in Table 5.8. It is to be noted that CL-2 and CL-3 use the faults that are not utilized to generate the training trajectories. The P_{PCC} responses from TPWL method are compared with the nonlinear model responses in Fig. 5.14. The P_{PCC} from the linear-based MOR obtained using 36^{th} order IRKA are also given to see advantage of the proposed method. Generally, it is obvious that the multiple TPWL method is able to produce accurate responses of the nonlinear system. The MSE values of P_{PCC} as listed in Table 5.9 are 4.74×10^{-3}, 3.12×10^{-2}, and 9.37×10^{-3} for CL-1, CL-2, and CL-3, respectively. On the other hand, the 36^{th} order IRKA are more erroneous in virtually all cases with the MSE values 7.83×10^{-2}, 1.12×10^{-1}, and 1.05×10^{-1} for CL-1, CL-2, and CL-3, respectively.

Lastly, the elapsed times for a 2 s simulation as evident from Table 5.9 are: CL-1 = 223.17 s and 26.7 s, CL-2 = 273.34 s and 44.41 s, and CL-3 = 247.18 s and 36.13 s for the nonlinear and multiple TPWL method, respectively. This indicates that the proposed method allows a significant reduction in the simulation time by a factor more than 6, while at the same time accurately predicts the nonlinear behaviours of the large-scale wind farm model.

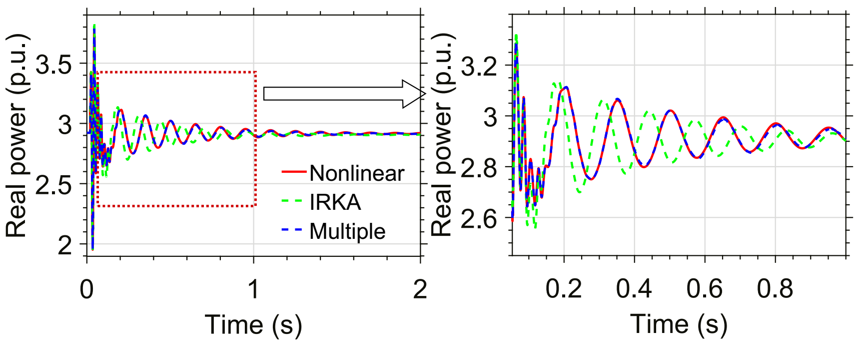

(a) Real power at PCC in CL-1

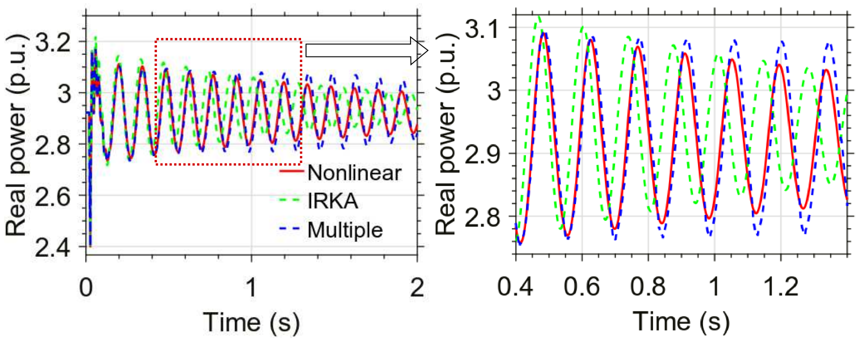

(b) Real power at PCC in CL-2

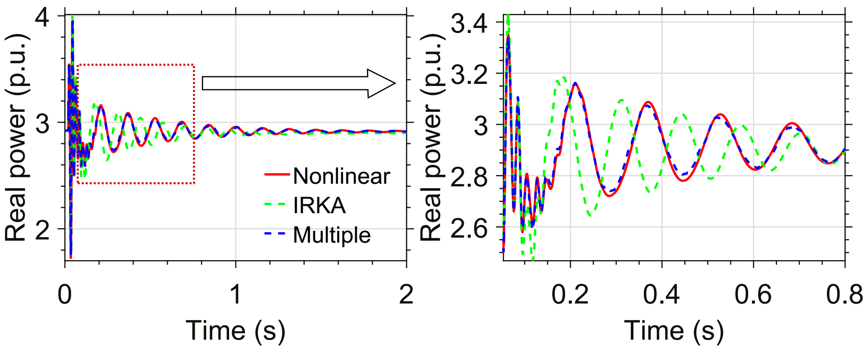

(c) Real power at PCC in CL-3

Figure 5.14: Robustness of multiple TPWL method on a large-scale wind farm

Table 5.9: Multiple TPWL for a large wind farm

Case	Method	Order	Elapsed time	MSE P_{PCC}
CL-1	Nonlinear	3892	223.17 s	-
	IRKA	60	2.69 s	7.83×10^{-2}
	Multiple	60	26.7 s	4.74×10^{-3}
CL-2	Nonlinear	3892	273.34 s	-
	IRKA	60	2.60 s	1.12×10^{-1}
	Multiple	60	44.41 s	3.12×10^{-2}
CL-3	Nonlinear	3892	247.18 s	-
	IRKA	60	2.78 s	1.05×10^{-1}
	Multiple	60	36.13 s	9.37×10^{-3}

5.5 Chapter summary

In this chapter, it has been demonstrated that the TPWL method is able to accurately capture the nonlinear oscillations in wind farm responses during large disturbances. The effectiveness of single TPWL method, using the simple and extended basis, to outperform the linear-based approaches has been demonstrated. The robustness of the method has also been studied for different types of faults and it is concluded that its accuracy is limited to certain types of faults. To enhance performance of the single TPWL method, this thesis has also proposed the multiple TPWL method which is based on multiple training trajectories. To reduce the number of linearization points, k-means clustering is deployed; however it is found that only a marginal reduction is achievable. A case using a large number of training trajectories could be more appropriate for k-means clustering, but it has not been demonstrated in this thesis.

Chapter 6

Conclusions and future work

6.1 Conclusions

This thesis has presented methods to develop simple, accurate, and manageable ROMs of large-scale wind farms to provide faster assessment of power system stability during small and large disturbances. In particular, the following conclusions can be drawn:

1. The application of BT method on large-scale wind farm models has been investigated. Different from [51] where very simplified wind farm models were used, in this study, the wind farms have been modelled in a great detail. It has been shown that the application of BT method to the wind farm models is limited by the computational time to extract the ROMs, which stems from solving the Lyapunov equations. Despite this difficulty, the ROM is able to capture the dynamics of wind farm FOMs, which has been shown in the frequency- and time-domain comparisons. It has also been demonstrated that the BT method preserves stability of FOMs.
2. The computational time problem in BT method to obtain the ROM is overcome by using ADI method, which performs an iterative procedure to solve the Lyapunov equations. It has been demonstrated that the ROM using ADI iteration is able to attain the accuracy of the BT at much lower computation cost, enabling the use of ADI-based BT for large-scale wind farms. In addition, having been tested on different orders of wind farm models, the ADI-based BT always produces stable ROMs.

3. A computationally efficient RK method has been successfully applied to reduce a high order wind farm model. A set of interpolation points should be carefully selected in order to obtain an accurate and stable reduced order model. It has been observed that the selection of interpolation points becomes increasingly difficult as the order of wind farm model increases.
4. The IRKA has been successfully applied to obtain a ROM of wind farm which is locally optimal with regard to H_2 norm. This method performs an iterative procedure to calculate a set of interpolation points and the corresponding tangential interpolation until the error is locally minimized. This overcomes the previous problem of interpolation point selections in the RK method. The IRKA method has also been successfully utilized to simplify the model of multi-terminal direct current (MTDC) system connected to two practical-sized wind farms. From the experiments, it is concluded that the IRKA method is able to outperform the RK method in all cases. In term of stability preservation, this method like RK method also does not preserve the stability of the FOM.
5. The important modes of FOMs of wind farms have been successfully extracted using the SAMDP algorithm. Different from other methods, the system matrix needs to be preconditioned since it explicitly calculates the eigenvalues of the wind farm models. After the preconditioning, the SAMDP method is successfully able to obtain ROMs of wind farms. It is also observed that the ROM obtained using SAMDP has always a much higher dimension than those obtained from the previous methods. This problem can be alleviated by utilizing SAMDP algorithm as the intermediate technique to produce a medium-sized wind farm model with order around 200. This model is then further reduced using the BT method to much lower order model. The SAMDP and hybrid SAMDP-BT methods are guaranteed to produce a stable ROM.
6. The nonlinear ROM of wind farms suitable for transient stability studies has been successfully obtained using the TPWL method. First, the effectiveness of the single TPWL method, which uses one training trajectory, has been investigated under various fault conditions and it is concluded that the accuracy of the method is limited to certain types of faults. Based on this, the multiple TPWL method based on multiple training trajectories has been proposed to enhance the performance of the single TPWL method on a more general scenario. Furthermore, k-means clustering algorithm has been used to reduce the

number of linearization points in the multiple TPWL method.

6.2 Future work

Although this thesis has mainly addressed the problem of developing simple, accurate, and manageable ROMs of large-scale wind farms, future work will focus on:

1. *Considering other types of WTG.* All results presented in this thesis consider only DFIG-type wind farms. Other technology such as PMSG has been overlooked. PMSG-based wind farms are in particular completely decoupled from the grid due to the full converter configuration; which might suggest that even smaller order of wind farms can be expected. Future research direction may consider performing MOR on a PMSG-type or mixed technology-type wind farm.
2. *Controller tuning using ROM.* As previously mentioned in Chapter 1, one of the reasons to perform MOR is to simplify control tuning process. However, obtaining a simple controller using ROM of wind farm has not been demonstrated in this thesis. Further research should explore the effectiveness of ROM to yield a simple and effective wind farm level controller, e.g. inertia controller.
3. *Obtaining nonlinear MOR for MTDC systems.* Although Subsections 4.2.1 and 4.2.2 have demonstrated that a linear MOR method can be effectively used to obtain ROM of an MTDC systems, Subsection 4.2.3 shows that the ROM becomes more erroneous when the wind farm behaves nonlinearly. In such a case, a more appropriate approach is to deploy nonlinear MOR methods to enhance the accuracy of ROMs of wind farms in the context of MTDC systems.
4. *MOR based on system identification.* All ROM methods used in this thesis assume that wind farm models are accurately known. However, this is often unrealistic in practice as accurate models are unavailable due to unreliable parameters or simplistic modelling assumptions. This will in turn affect the accuracy of ROMs. Future work will focus on developing a ROM method based on measurements, hence eliminating the requirement of accurate FOMs of wind farms.

Appendix A

Model order reduction algorithms

A.1 BT algorithm

Algorithm 3: Balanced truncation

Input: A, B, C

Output: Reduced system $\hat{A}_{11}, \hat{B}_1, \hat{C}_1$

1: Solve Lyapunov equations:
$AP + A^T P + BB^T = 0$ and $A^T Q + QA + C^T C = 0$

2: Find Cholesky factor of $P = R^T R$

3: Calculate SVD of $RQR^T = U\Sigma^2 U^T$

4: Calculate the transformation matrix and its inverse: $T = R^T U \Sigma^{1/2}$ and $T^{-1} = RU\Sigma^{-1/2}$

5: Transform system to balanced coordinate: $\hat{A} = T^{-1}AT$, $\hat{B} = T^{-1}B$, $\hat{C} = CT$, $\hat{D} = D$

6: Partition $\hat{G}(s)$ according to partition of HSV Σ as in (3.19)

7: Obtain the reduced system: $\hat{A}_{11}, \hat{B}_1, \hat{C}_1$

A.2 ADI-based BT algorithm

Algorithm 4: ADI-based balanced truncation

Input: A, B, C, D, and shift parameters η_i
Output: $P = RR^{\mathrm{T}}$ that solves $AP + A^T P + BB^T = 0$

$R = 0$
$W_0 = B$
$V_1 = \sqrt{-2\mathrm{Re}\alpha_1}(A + \eta_1 I)^{-1}B$
k=2
while $\left\|W_{k-1}W_{k-1}^T\right\| > \epsilon$ or $k \leq$ iter_max **do**
    $V_k = \sqrt{\mathrm{Re}\eta_k/\mathrm{Re}\eta_{k-1}}(V_{k-1} - (\eta_k + \overline{\eta_{k-1}})(A + \eta_1 I)^{-1}V_{k-1})$
    $R_k = [R_{k-1}V_k]$
    $W_k = W_{k-1} - 2\mathrm{Re}(\eta_k)V_k$
    $k = k + 1$
end while

A.3 RK algorithm

Algorithm 5: Rational Krylov subspace

Input: A, B, C, D and interpolation point σ
Output: **Reduced system** $\hat{A}, \hat{B}, \hat{C}, \hat{D}$

Calculate Krylov subspace V and W using Arnoldi or Lanczos algorithm.
Reduce the original system: $\hat{A} = WAV$, $\hat{B} = WB$, $\hat{C} = CV$, $\hat{D} = D$

A.4 IRKA algorithm

Algorithm 6: Iterative rational Krylov algorithm

Input: $A, B, C, \sigma_i^0, l_i^0, r_i^0$ for $i = 1, \ldots, r$, and tolerance ϵ

Output: Reduced system $\hat{A}, \hat{B}, \hat{C}$

Construct V and W using σ_i^0, l_i^0, r_i^0.

Reduced model: $\hat{A} = WAT$, $\hat{B} = WB$, $\hat{C} = CV$, $\hat{D} = D$

while err_1 and $\mathrm{err}_2 > \epsilon$ **do**

    $k = k + 1$

    Solve: $\hat{A}\hat{X} = \hat{X}\mathrm{diag}(\hat{\lambda}_1, ..., \lambda_r)$

    Set $\sigma_i^k = -\hat{\lambda}_i, l_i^k = \hat{C}\hat{X}\hat{e}_i$ and $r_i^k = (\hat{e}_i^T \hat{X}^{-1} B)^T$

    Construct V and W using σ_i^k, l_i^k, r_i^k.

    $\mathrm{err}_1 = \|\sigma_i^k - \sigma_i^{k-1}\|_2$, $\mathrm{err}_2 = \left\| G^k(s) - \hat{G}^k(s) \right\|_2$

end while

Reduced model: $\hat{A} = WAV$, $\hat{B} = WB$, $\hat{C} = CV$, $\hat{D} = D$

A.5 SAMDP algorithm

Algorithm 7: Subspace accelerated MIMO dominant pole algorithm

```
Input: A, B, C, D, number of wanted poles r, and initial value of pole s_1
Output: Reduced system Â, B̂, Ĉ
k=1, r_found = 0, X = Y = Λ = V = W = []
Reduced model: Â = WAT, B̂ = WB, Ĉ = CV, D̂ = D
while r_found < r do
    Calculate the smallest eigentriplet (μ_min, u, v) of (C^T (s_k I − A)^{-1} B + D)^{-1}
    Solve x = (s_k I − A)^{-1} Bu
    Solve y = ((s_k I − A)^*)^{-1} Cv
    Using a modified Gram-Schmidt (MGS) [116], incorporate x and y into X and Y,
    respectively.
    Compute G = Y * X and T = Y * AX
    Compute eigentriplets of (T, G): (λ̃_i, x̃_i^u, ỹ_i^u, i = 1, ..., k)
    Estimate eigentriplets of A: (λ̂_i = λ̃_i, x̂_i^u = X x̃_i^u, ŷ_i^u = Y ỹ_i^u, i = 1, ..., k)
    Select eigentriplet of A with the largest ratio of ||R̂_i||_2 / |Re(λ̂_i)|, i.e.
    (λ̂_largest, x̂_largest^u, ŷ_largest^u)
    if ||A x̂_largest^u − λ̂_largest x̂_largest^u||_2 < ε then
        Deflate (λ̂_largest, x̂_largest^u, ŷ_largest^u) from eigenspace of A
        Construct: V = [V  x̂_largest^u] and W = [W  ŷ_largest^u]
    end if
    s_{k+1} = λ̂_largest
    k = k + 1
end while
Reduced model: Â = WAV, B̂ = WB, Ĉ = CV, D̂ = D
```

The algorithm is a simplified version of the one presented in [78]. The interested readers are requested to review the reference for a more detailed presentation.

Appendix B

Solving linear equations using ADI iteration

Let define a linear system of equations [84, 85]:

$$Ax = b \tag{B.1}$$

where A is a symmetric positive definite matrix. So A can be factorized as a sum of two positive definite matrices, namely L and R. As a result, (B.1) can be rewritten as follows:

$$Lx + Rx = b \tag{B.2}$$

This equation can be solved using ADI iteration by performing the following routines:

$$\begin{aligned} (L + \eta_i I_n)x_{i-\frac{1}{2}} &= (\eta_i I_n - R)x_{i-1} + b \\ (R + \eta_i I_n)x_i &= (\eta_i I_n - R)x_{i-\frac{1}{2}} + b \end{aligned} \tag{B.3}$$

where η_i are the ADI shift parameters. A careful selection of these parameter is critical for ADI iteration to converge to the solution x.

Appendix C

System parameters

1. **WTG p.u. in $S_{\mathbf{base}} = 5$ MVA and $V_{\mathbf{base}} = 600\ V$**: $R_s = 0.005$, $R_r 0.0055$, $L_m = 4$, $L_{ss} = 4.04$, $L_{rr} = 4.0602$, $H_t = 4$, $H_g = 0.4$, $k = 0.03$, $c = 0.01$, $\omega_s = 1$, $\omega_{elB} = 314.15$ rad/s. RSC: $K_{p11} = 0$, $K_{i11} = -60$, $K_{p12} = -0.23$, $K_{i12} = -3$, $K_{p21} = 0$, $K_{i21} = 90$, $K_{p22} = -0.23$, $K_{i22} = -3$. GSC: $K_{p14} = -22.5$, $K_{i14} = -870$, $K_{p13} = 0.3$, $K_{i13} = 200$, $K_{p24} = 0$, $K_{i24} = -62$, $K_{p23} = 0.3$, $K_{i23} = 200$. LCL filter: $L_c = 0.16$, $R_c = 0$, $C_f = 0.015$, $R_{cf} = 0.74$, $R_g = 0$, $L_g = 0.0033$.

2. **WTG transformers p.u. in $S_{\mathbf{base}} = 100$ MVA and $V_{\mathbf{base}} = 600\ V$**: $R = 0.15$, $L = 1.33$, $C = 3.4 \times 10^{-6}$.

3. **33 kV cables p.u. in $S_{\mathbf{base}} = 100$ MVA**: $R = 0.0048$, $L = 0.008$, $C = 9.8 \times 10^{-4}$.

4. **Wind farm transformers p.u. in $S_{\mathbf{base}} = 100$ MVA**: $R = 0.0008$, $L = 0.0611$, $C = 7.5 \times 10^{-5}$.

5. **High voltage cables p.u. in $S_{\mathbf{base}} = 100$ MVA**: $R = 0.0033$, $L = 0.0139$, $C = 0.4529$.

6. **MTDC used in Chapter 4 p.u. in $S_{\mathbf{base}} = 100$ MVA**: $R_{dc} = 0.08$, $L_{dc} = 1.56$, $C_{dc} = 9$. RL filter: $R_f = 0.0101$, $L_f = 0.1332$. VSC controller: inner-loop= $K_p = 0.8$, $K_i = 20$. Outer-loop for offshore converter for $d-$ and $q-$axis: $K_p = 15$, $K_i = 100$. Outer-loop for slack converter: $d-$axis=$K_p = -0.29$, $K_i = -300$, $q-$axis=$K_p = 0$, $K_i = 36$ .Outer-loop for onshore converter: $d-$axis=$K_p = 15$, $K_i = 100$,$q-$axis=$K_p = 15$, $K_i = 100$.

7. **Synchronous generator p.u. in $S_{\mathbf{base}} = 100$ MVA**: $x_l = 0.022$, $R_a = 2 \times 10^{-4}$, $x_d = 0.2$, $x'_d = 0.033$, $T'_{do} = 8$, $x_q = 0.19$, $x'_q = 0.016$, $T'_{qo} = 0.4$, $H = 54$, $D = 0.1$.

8. **Two-area system parameters used in Chapter 4**: adopted from [117].

9. ***Study-area* used in Chapter 5 p.u. in $S_{\mathbf{base}} = 100$ MVA**: line 4-5=$R = 0.0001$, $L = 0.001$, $C = 0.00175$, line 5-6=$R = 0.0002$, $L = 0.002$, $C = 0.0035$, line 6-7=6-8=$R = 0.00015$, $L = 0.0015$, $C = 0.002625$

Appendix D

Copyright clearance

Copyright Clearance Center RightsLink®

Home | Create Account | Help

IEEE
Requesting permission to reuse content from an IEEE publication

Title: Model Order Reduction of Wind Farms: Linear Approach

Author: Husni Rois Ali; Linash Puthenpurayil Kunjumuhammed; Bikash Chandra Pal; Andrzej Adamczyk; Konstantin Vershinin

Publication: Sustainable Energy, IEEE Transactions on

Publisher: IEEE

Date: Dec 31, 1969

LOGIN

If you're a copyright.com user, you can login to RightsLink using your copyright.com credentials.

Already **a RightsLink user** or want to learn more?

Thesis / Dissertation Reuse

The IEEE does not require individuals working on a thesis to obtain a formal reuse license, however, you may print out this statement to be used as a permission grant:

Requirements to be followed when using any portion (e.g., figure, graph, table, or textual material) of an IEEE copyrighted paper in a thesis:

1) In the case of textual material (e.g., using short quotes or referring to the work within these papers) users must give full credit to the original source (author, paper, publication) followed by the IEEE copyright line © 2011 IEEE.
2) In the case of illustrations or tabular material, we require that the copyright line © [Year of original publication] IEEE appear prominently with each reprinted figure and/or table.
3) If a substantial portion of the original paper is to be used, and if you are not the senior author, also obtain the senior author's approval.

Requirements to be followed when using an entire IEEE copyrighted paper in a thesis:

1) The following IEEE copyright/ credit notice should be placed prominently in the references: © [year of original publication] IEEE. Reprinted, with permission, from [author names, paper title, IEEE publication title, and month/year of publication]
2) Only the accepted version of an IEEE copyrighted paper can be used when posting the paper or your thesis on-line.
3) In placing the thesis on the author's university website, please display the following message in a prominent place on the website: In reference to IEEE copyrighted material which is used with permission in this thesis, the IEEE does not endorse any of [university/educational entity's name goes here]'s products or services. Internal or personal use of this material is permitted. If interested in reprinting/republishing IEEE copyrighted material for advertising or promotional purposes or for creating new collective works for resale or redistribution, please go to http://www.ieee.org/publications_standards/publications/rights/rights_link.html to learn how to obtain a License from RightsLink.

If applicable, University Microfilms and/or ProQuest Library, or the Archives of Canada may supply single copies of the dissertation.

BACK | CLOSE WINDOW

Copyright Clearance Center RightsLink®

Home | Create Account | Help

IEEE Requesting permission to reuse content from an IEEE publication

Title: A Trajectory Piecewise-Linear Approach to Nonlinear Model Order Reduction of Wind Farms

Author: Husni Rois Ali

Publication: Sustainable Energy, IEEE Transactions on

Publisher: IEEE

Date: Dec 31, 1969

LOGIN

If you're a copyright.com user, you can login to RightsLink using your copyright.com credentials.

Already **a RightsLink user** or want to learn more?

Thesis / Dissertation Reuse

The IEEE does not require individuals working on a thesis to obtain a formal reuse license, however, you may print out this statement to be used as a permission grant:

Requirements to be followed when using any portion (e.g., figure, graph, table, or textual material) of an IEEE copyrighted paper in a thesis:

1) In the case of textual material (e.g., using short quotes or referring to the work within these papers) users must give full credit to the original source (author, paper, publication) followed by the IEEE copyright line © 2011 IEEE.
2) In the case of illustrations or tabular material, we require that the copyright line © [Year of original publication] IEEE appear prominently with each reprinted figure and/or table.
3) If a substantial portion of the original paper is to be used, and if you are not the senior author, also obtain the senior author's approval.

Requirements to be followed when using an entire IEEE copyrighted paper in a thesis:

1) The following IEEE copyright/ credit notice should be placed prominently in the references: © [year of original publication] IEEE. Reprinted, with permission, from [author names, paper title, IEEE publication title, and month/year of publication]
2) Only the accepted version of an IEEE copyrighted paper can be used when posting the paper or your thesis on-line.
3) In placing the thesis on the author's university website, please display the following message in a prominent place on the website: In reference to IEEE copyrighted material which is used with permission in this thesis, the IEEE does not endorse any of [university/educational entity's name goes here]'s products or services. Internal or personal use of this material is permitted. If interested in reprinting/republishing IEEE copyrighted material for advertising or promotional purposes or for creating new collective works for resale or redistribution, please go to http://www.ieee.org/publications_standards/publications/rights/rights_link.html to learn how to obtain a License from RightsLink.

If applicable, University Microfilms and/or ProQuest Library, or the Archives of Canada may supply single copies of the dissertation.

BACK | CLOSE WINDOW

Bibliography

[1] "Global wind report; annual market update," *Global Wind Energy Council*, 2018.

[2] "[online:]," *http://cdm-en.ccchina.gov.cn.* , Accessed 16/04/2019.

[3] "SeaTitan 10 MW wind turbine [online:]," *http://www.amsc.com/documents/seatitan-10-mw-wind-turbine-data-sheet/*, Accessed 16/04/2019.

[4] J. Adams, C. Carter, and S.-H. Huang, "ERCOT experience with sub-synchronous control interaction and proposed remediation," in *PES T&D 2012*, pp. 1–5, IEEE, 2012.

[5] S.-H. Huang, J. Schmall, J. Conto, J. Adams, Y. Zhang, and C. Carter, "Voltage control challenges on weak grids with high penetration of wind generation: Ercot experience," in *2012 IEEE Power and Energy Society General Meeting*, pp. 1–7, IEEE, 2012.

[6] "Wasted wind energy solving the problem of bad grid connections." http://www.power-technology.com/features/featurewasted-wind-energy-grid-connections-turbines/. Accessed: 16/04/2019.

[7] H. Liu, X. Xie, J. He, T. Xu, Z. Yu, C. Wang, and C. Zhang, "Subsynchronous interaction between direct-drive PMSG based wind farms and weak AC networks," *IEEE Transactions on Power Systems*, vol. 32, no. 6, pp. 4708–4720, 2017.

[8] C. Buchhagen, C. Rauscher, A. Menze, and J. Jung, "Borwin1-first experiences with harmonic interactions in converter dominated grids," in *Die Energiewende-Blueprints for the new energy age International ETG Congress 2015*, pp. 1–7, VDE, 2015.

[9] "Bard 1 transmission problems continue." http://www.windpoweroffshore.com/article/1297004/bard-1-transmission-problems-continue/. Accessed: 16/04/2019.

[10] M. Green and D. J. Limebeer, *Linear robust control*. Courier Corporation, 2012.

[11] D.-W. Gu, P. Petkov, and M. M. Konstantinov, *Robust control design with MATLAB®*. Springer Science & Business Media, 2005.

[12] K. Zhou and J. C. Doyle, *Essentials of robust control*, vol. 180. Prentice hall Upper Saddle River, NJ, 1998.

[13] J. Rose and I. A. Hiskens, "Estimating wind turbine parameters and quantifying their effects on dynamic behavior," in *2008 IEEE Power and Energy Society General Meeting-Conversion and Delivery of Electrical Energy in the 21st Century*, pp. 1–7, IEEE, 2008.

[14] J. H. Chow and P. V. Kokotovic, "Time scale modeling of sparse dynamic networks," *IEEE Transactions on Automatic Control*, vol. 30, no. 8, pp. 714–722, 1985.

[15] E. Zhou, "Power oscillation flow study of electric power systems," *International Journal of Electrical Power & Energy Systems*, vol. 17, no. 2, pp. 143–150, 1995.

[16] J. Y. Ruan, Z. X. Lu, Y. Qiao, and Y. Min, "Analysis on applicability problems of the aggregation-based representation of wind farms considering DFIGs LVRT behaviors," *IEEE Transactions on Power Systems*, vol. 31, pp. 4953–4965, Nov 2016.

[17] J. Zou, C. Peng, Y. Yan, H. Zheng, and Y. Li, "A survey of dynamic equivalent modeling for wind farm," *Renewable and Sustainable Energy Reviews*, vol. 40, pp. 956 – 963, 2014.

[18] V. Akhmatov and H. Knudsen, "An aggregate model of a grid-connected, large-scale, offshore wind farm for power stability investigations importance of windmill mechanical system," *International Journal of Electrical Power & Energy Systems*, vol. 24, no. 9, pp. 709–717, 2002.

[19] J. Slootweg and W. Kling, "Aggregated modelling of wind parks in power system dynamics simulations," in *2003 IEEE Bologna Power Tech Conf Proc*, vol. 3, pp. 6–11, IEEE, 2003.

[20] D. N. Hussein, M. Matar, and R. Iravani, "A wideband equivalent model of type-3 wind power plants for emt studies," *IEEE Transactions on Power Delivery*, vol. 31, pp. 2322–2331, Oct 2016.

[21] D. N. Hussein, M. Matar, and R. Iravani, "A type-4 wind power plant equivalent model for the analysis of electromagnetic transients in power systems," *IEEE Transactions on Power Systems*, vol. 28, no. 3, pp. 3096–3104, 2013.

[22] Y. Jin, P. Ju, F. Wu, X. Pan, Q. Chen, L. Sun, C. Qin, and C. Cai, "Equivalent modeling of wind farm in frequency domain," in *2014 IEEE PES General Meeting — Conference Exposition*, pp. 1–5, July 2014.

[23] W. Li, P. Chao, X. Liang, D. Xu, and X. Jin, "An improved single-machine equivalent method of wind power plants by calibrating power recovery behaviors," *IEEE Transactions on Power Systems*, vol. 33, no. 4, pp. 4371–4381, 2018.

[24] M. Chowdhury, W. Shen, N. Hosseinzadeh, and H. Pota, "A novel aggregated DFIG wind farm model using mechanical torque compensating factor," *Energy conversion and management*, vol. 67, pp. 265–274, 2013.

[25] H. Liu and Z. Chen, "Aggregated modelling for wind farms for power system transient stability studies," in *2012 Asia-Pacific Power and Energy Engineering Conference*, pp. 1–6, March 2012.

[26] M. Ali, J. Milanović, I.-S. Ilie, and G. Chicco, "Comparison of wind farm aggregate models for transient stability studies," in *Proc. 17th Power System Computation Conf.(PSCC)*, 2011.

[27] A. Perdana, S. Uski-Joutsenvuo, O. Carlson, and B. Lemström, "Comparison of an aggregated model of a wind farm consisting of fixed-speed wind turbines with field measurement," *Wind Energy*, vol. 11, no. 1, pp. 13–27, 2008.

[28] H. Li, C. Yang, B. Zhao, H. Wang, and Z. Chen, “Aggregated models and transient performances of a mixed wind farm with different wind turbine generator systems,” *Electric Power Systems Research*, vol. 92, pp. 1–10, 2012.

[29] I. Erlich, F. Shewarega, C. Feltes, F. Koch, and J. Fortmann, “Determination of dynamic wind farm equivalents using heuristic optimization,” in *2012 IEEE Power and Energy Society General Meeting*, pp. 1–8, IEEE, 2012.

[30] Y. Wang, C. Lu, L. Zhu, G. Zhang, X. LI, and Y. Chen, “Comprehensive modeling and parameter identification of wind farms based on wide-area measurement systems,” *Journal of Modern Power Systems and Clean Energy*, vol. 4, no. 3, pp. 383–393, 2016.

[31] Y. Zhou, L. Zhao, and W. Lee, “Robustness analysis of dynamic equivalent model of DFIG wind farm for stability study,” *IEEE Transactions on Industry Applications*, pp. 1–1, 2018.

[32] X. Cheng, W. Lee, M. Sahni, Y. Cheng, and L. K. Lee, “Dynamic equivalent model development to improve the operation efficiency of wind farm,” *IEEE Transactions on Industry Applications*, vol. 52, pp. 2759–2767, July 2016.

[33] M. Poller and S. Achilles, “Aggregated wind park models for analyzing power system dynamics,” in *In 4th International Workshop on Large-Scale Integration of Wind Power and Transmission Networks for Offshore Wind Farms, Billund, Denmark*, October 2003.

[34] L. M. Fernández, F. Jurado, and J. R. Saenz, “Aggregated dynamic model for wind farms with doubly-fed induction generator wind turbines,” *Renewable energy*, vol. 33, no. 1, pp. 129–140, 2008.

[35] M. Mercado-Vargas, D. Gómez-Lorente, O. Rabaza, and E. Alameda-Hernandez, “Aggregated models of permanent magnet synchronous generators wind farms,” *Renewable Energy*, vol. 83, pp. 1287–1298, 2015.

[36] K. Rudion, Z. A. Styczynski, A. Orths, and O. Ruhle, “Mawind - tool for the aggregation of wind farm models,” in *2008 IEEE Power and Energy Society General Meeting - Conversion and Delivery of Electrical Energy in the 21st Century*, pp. 1–8, July 2008.

[37] K. Rudion, “Reduction of wind farm models using the coherency approach,” in *Proc. Power Systems Computational Conference 2008, Glasgow*, 2008.

[38] T. Sun, X. Mou, and Z. Li, “A practical clustering method of DFIG wind farms based on dynamic current error,” in *2015 IEEE Power Energy Society General Meeting*, pp. 1–5, July 2015.

[39] W. Li, P. Chao, X. Liang, J. Ma, D. Xu, and X. Jin, “A practical equivalent method for dfig wind farms,” *IEEE Transactions on Sustainable Energy*, vol. 9, pp. 610–620, April 2018.

[40] J. Huo, A. Xue, Q. Wang, T. Bi, and C. Li, “Research on clustering algorithm for dynamic equivalence of doubly-fed wind farms,” in *2014 International Conference on Power System Technology (POWERCON)*, pp. 775–781, IEEE, 2014.

[41] M. Ali, I. S. Ilie, J. V. Milanovic, and G. Chicco, “Probabilistic clustering of wind generators,” in *IEEE PES General Meeting*, pp. 1–6, July 2010.

[42] M. Ali, I.-S. Ilie, J. V. Milanovic, and G. Chicco, "Wind farm model aggregation using probabilistic clustering," *IEEE Transactions on Power Systems*, vol. 28, no. 1, pp. 309–316, 2013.

[43] J. Zou, C. Peng, H. Xu, and Y. Yan, "A fuzzy clustering algorithm-based dynamic equivalent modeling method for wind farm with DFIG," *IEEE Transactions on Energy Conversion*, vol. 30, pp. 1329–1337, Dec 2015.

[44] W. Teng, X. Wang, Y. Meng, and W. Shi, "Dynamic clustering equivalent model of wind turbines based on spanning tree," *Journal of Renewable and Sustainable Energy*, vol. 7, no. 6, p. 063126, 2015.

[45] P. Wang, Z. Zhang, Q. Huang, N. Wang, X. Zhang, and W. Lee, "Improved wind farm aggregated modeling method for large-scale power system stability studies," *IEEE Transactions on Power Systems*, pp. 1–1, 2018.

[46] C. Huang, K. Zhang, X. Dai, and W. Wang, "Model reduction of power systems based on the balanced residualization method," in *2012 IEEE Power and Energy Society General Meeting*, pp. 1–7, IEEE, 2012.

[47] H. A. Pulgar-Painemal and P. W. Sauer, "Towards a wind farm reduced-order model," *Electric Power Systems Research*, vol. 81, no. 8, pp. 1688–1695, 2011.

[48] H. A. Pulgar-Painemal and P. W. Sauer, "Reduced-order model of type-c wind turbine generators," *Electric Power Systems Research*, vol. 81, no. 4, pp. 840–845, 2011.

[49] Y. Ni, Z. Du, C. Li, and G. Zhang, "Cross-gramian-based dynamic equivalence of wind farms," *IET Generation, Transmission Distribution*, vol. 10, no. 6, pp. 1422–1430, 2016.

[50] R. M. Castro and J. F. De Jesus, "A wind park reduced-order model using singular perturbations theory," *IEEE Transactions on Energy Conversion*, vol. 11, no. 4, pp. 735–741, 1996.

[51] S. Ghosh and N. Senroy, "Balanced truncation based reduced order modeling of wind farm," *International Journal of Electrical Power & Energy Systems*, vol. 53, pp. 649–655, 2013.

[52] S. Ghosh, N. Senroy, and S. Kamalasadan, "Reduced order modeling of wind farms for inclusion in large power system simulations for primary frequency response application," in *2014 North American Power Symposium (NAPS)*, pp. 1–6, IEEE, 2014.

[53] H. A. Pulgar Painemal, *Wind farm model for power system stability analysis*. PhD thesis, University of Illinois at Urbana-Champaign, 2011.

[54] D.-E. Kim and M. A. El-Sharkawi, "Dynamic equivalent model of wind power plant using an aggregation technique," *IEEE Transactions on Energy Conversion*, vol. 30, no. 4, pp. 1639–1649, 2015.

[55] D. E. Kim and M. A. El-Sharkawi, "Dynamic equivalent model of wind power plant using parameter identification," *IEEE Transactions on Energy Conversion*, vol. 31, pp. 37–45, March 2016.

[56] F. González-Longatt, P. Regulski, P. Wall, and V. Terzija, "Procedure for estimation of equivalent model parameters for a wind farm using post-disturbance on-line measurement data," in *2011 2nd IEEE PES International Conference and Exhibition on Innovative Smart Grid Technologies (ISGT Europe*, pp. 1–7, Dec 2011.

[57] L. P. Kunjumuhammed, B. C. Pal, C. Oates, and K. J. Dyke, "Electrical oscillations in wind farm systems: Analysis and insight based on detailed modeling," *IEEE Transactions on Sustainable Energy*, no. 1, pp. 51–62, 2016.

[58] N. Jensen, "A note on wind generator interaction, risø-m no. 2411 risø national laboratory roskilde, 1–16," 1983.

[59] F. Mei, *Small-signal modelling and analysis of doubly-fed induction generators in wind power applications*. PhD thesis, Imperial College London, 2008.

[60] "Recommended phasor diagram for synchronous machines," *IEEE Transactions on Power Apparatus and Systems*, vol. PAS-88, pp. 1593–1610, Nov 1969.

[61] L. P. Kunjumuhammed, B. C. Pal, R. Gupta, and K. J. Dyke, "Stability analysis of a PMSG-based large offshore wind farm connected to a VSC-HVDC," *IEEE Transactions on Energy Conversion*, vol. 32, no. 3, 2017.

[62] S. Cole, J. Beerten, and R. Belmans, "Generalized dynamic VSC MTDC model for power system stability studies," *IEEE Transactions on Power Systems*, vol. 25, no. 3, pp. 1655–1662, 2010.

[63] S. Kuenzel, *Modelling and control of an ACDC system with significant generation from wind*. PhD thesis, Imperial College London, 2014.

[64] D. Pullaguram, S. Mishra, N. Senroy, and M. Mukherjee, "Design and tuning of robust fractional order controller for autonomous microgrid VSC system," *IEEE Transactions on Industry Applications*, vol. 54, no. 1, pp. 91–101, 2017.

[65] A. Yogarathinam and N. R. Chaudhuri, "Stability-constrained adaptive droop for power sharing in AC-MTDC grids," *IEEE Transactions on Power Systems*, vol. 34, no. 3, pp. 1955–1965, 2019.

[66] D. Xu, M. Han, and A. M. Gole, "Propagation of AC background harmonics in MMC HVDC multiterminal systems due to resonances and mitigation measures," *IEEE Transactions on Power Delivery*, vol. 33, no. 1, pp. 229–238, 2017.

[67] S. Kuenzel, L. P. Kunjumuhammed, B. C. Pal, and I. Erlich, "Impact of wakes on wind farm inertial response," *IEEE Transactions on Sustainable Energy*, vol. 5, no. 1, pp. 237–245, 2014.

[68] J. F. Ainslie, "Calculating the flowfield in the wake of wind turbines," *Journal of Wind Engineering and Industrial Aerodynamics*, vol. 27, no. 1-3, pp. 213–224, 1988.

[69] M. Soleimanzadeh, R. Wisniewski, and S. M. Shakeri, "Wind deficit model in a wind farm using finite volume method," in *2010 American Control Conference (ACC)*, pp. 4343–4348, IEEE, 2010.

[70] J. Cleve, M. Greiner, P. Enevoldsen, B. Birkemose, and L. Jensen, “Model-based analysis of wake-flow data in the nysted offshore wind farm,” *Wind Energy*, vol. 12, no. 2, pp. 125–135, 2009.

[71] B. C. Moore, “Principal component analysis in linear systems: Controllability, observability, and model reduction,” *IEEE Transactions on Automatic Control*, vol. 26, no. 1, pp. 17–32, 1981.

[72] A. C. Antoulas, *Approximation of large-scale dynamical systems*, vol. 6. Siam, 2005.

[73] F. D. Freitas, J. Rommes, and N. Martins, “Gramian-based reduction method applied to large sparse power system descriptor models,” *IEEE Transactions on Power Systems*, vol. 23, no. 3, pp. 1258–1270, 2008.

[74] M. Heinkenschloss, D. C. Sorensen, and K. Sun, “Balanced truncation model reduction for a class of descriptor systems with application to the oseen equations,” *SIAM Journal on Scientific Computing*, vol. 30, no. 2, pp. 1038–1063, 2008.

[75] E. J. Grimme, *Krylov Projection Methods for Model Reduction.* PhD thesis, University of Illinois at Urbana-Champaign, 1997.

[76] S. Gugercin, C. Beattie, and A. Antoulas, “Rational Krylov methods for optimal H_2 model reduction,” *Proceedings of the 17th International Symposium on Mathematical Theory of Networks and Systems*, vol. 2006, no. 7, pp. 1665–1667, 2006.

[77] S. Gugercin and A. Antoulas, “An H_2 error expression for the Lanczos procedure,” in *Proceedings. 42nd IEEE Conference on Decision and Control, 2003*, vol. 2, pp. 1869–1872, IEEE, 2003.

[78] J. Rommes and N. Martins, “Efficient computation of multivariable transfer function dominant poles using subspace acceleration,” *IEEE Transactions on Power Systems*, vol. 21, no. 4, pp. 1471–1483, 2006.

[79] H. R. Ali, L. Puthenpurayil Kunjumuhammed, B. C. Pal, A. Adamczyk, and K. Vershinin, “Model order reduction of wind farms: Linear approach,” *IEEE Transactions on Sustainable Energy*, pp. 1–1, 2018.

[80] J. Glass, *Simulink Control Design User’s Guide.* MathWorks, The MathWorks, Inc. 3 Apple Hill Drive Natick, MA 01760-2098, 5.2 ed., Sept. 2018.

[81] J. H. Chow, *Power system coherency and model reduction.* Springer, 2013.

[82] C.-T. Chen, *Linear system theory and design.* Oxford Univ Press,Inc., 1995.

[83] K. Glover, “All optimal Hankel-norm approximations of linear multivariable systems and their L_∞ error bounds,” *International Journal of Control*, vol. 39, no. 6, pp. 1115–1193, 1984.

[84] P. Kürschner, *Efficient Low-Rank Solution of Large-Scale Matrix Equations.* PhD thesis, Shaker Verlag Aachen, 2016.

[85] E. W. Sachs, *Efficient numerical solution of large scale algebraic matrix equations in PDE control and model order reduction.* PhD thesis, Chemnitz University of Technology, 2009.

[86] T. Penzl, "A cyclic low-rank Smith method for large sparse Lyapunov equations," *SIAM Journal on Scientific Computing*, vol. 21, no. 4, pp. 1401–1418, 1999.

[87] E. L. Wachspress, *The ADI model problem.* Springer, 2013.

[88] A. Castagnotto, M. C. Varona, L. Jeschek, and B. Lohmann, "sss & sssMOR: Analysis and reduction of large-scale dynamic systems in MATLAB," *at-Automatisierungstechnik*, vol. 65, no. 2, pp. 134–150, 2017.

[89] D. Chaniotis and M. Pai, "Model reduction in power systems using krylov subspace methods," *IEEE Transactions on Power Systems*, vol. 20, no. 2, pp. 888–894, 2005.

[90] G. Strang, "Krylov subspaces and conjugate gradients." Lecture note.

[91] K. Gallivan, A. Vandendorpe, and P. Van Dooren, "Model reduction of MIMO systems via tangential interpolation," *SIAM Journal on Matrix Analysis and Applications*, vol. 26, no. 2, pp. 328–349, 2004.

[92] "[online:]," *http://w3.onera.fr/more/?q=teaching*, Accessed: 16/04/2019.

[93] P. Van Dooren, K. A. Gallivan, and P.-A. Absil, "H_2-optimal model reduction of MIMO systems," *Applied Mathematics Letters*, vol. 21, no. 12, pp. 1267–1273, 2008.

[94] S. L. Varricchio, F. D. Freitas, and N. Martins, "Hybrid modal-balanced truncation method based on power system transfer function energy concepts," *IET Generation, Transmission & Distribution*, vol. 9, no. 11, pp. 1186–1194, 2015.

[95] N. Chaudhuri, B. Chaudhuri, R. Majumder, and A. Yazdani, *Multi-terminal Direct-current Grids: Modeling, Analysis, and Control.* John Wiley & Sons, 2014.

[96] D. Van Hertem and M. Ghandhari, "Multi-terminal VSC HVDC for the european super-grid: Obstacles," *Renewable and sustainable energy reviews*, vol. 14, no. 9, pp. 3156–3163, 2010.

[97] H. Rao, "Architecture of nan'ao multi-terminal VSC-HVDC system and its multi-functional control," *CSEE Journal of Power and Energy Systems*, vol. 1, no. 1, pp. 9–18, 2015.

[98] J. Binkai and W. Zhixin, "The key technologies of VSC-MTDC and its application in China," *Renewable and Sustainable Energy Reviews*, vol. 62, pp. 297–304, 2016.

[99] S. Gordon, "Supergrid to the rescue [electricity supply security]," *Power Engineer*, vol. 20, no. 5, pp. 30–33, 2006.

[100] J. Blau, "Europe plans a north sea grid," *IEEE spectrum*, vol. 47, no. 3, pp. 12–13, 2010.

[101] J. Beerten, S. Cole, and R. Belmans, "Generalized steady-state VSC MTDC model for sequential AC/DC power flow algorithms," *IEEE Transactions on Power Systems*, vol. 27, no. 2, pp. 821–829, 2012.

[102] J. Beerten, S. Cole, and R. Belmans, "A sequential AC/DC power flow algorithm for networks containing multi-terminal VSC HVDC systems," in *IEEE PES General Meeting*, pp. 1–7, IEEE, 2010.

[103] S. Akkari, *Control of a multi-terminal HVDC (MTDC) system and study of the interactions between the MTDC and the AC grids.* PhD thesis, Université Paris-Saclay, 2016.

[104] I. M. Sanz, B. Chaudhuri, and G. Strbac, "Inertial response from offshore wind farms connected through DC grids," *IEEE Transactions on Power Systems*, vol. 30, no. 3, pp. 1518–1527, 2015.

[105] Y. Phulpin, "Communication-free inertia and frequency control for wind generators connected by an HVDC-link," *IEEE Transactions on Power Systems*, vol. 27, no. 2, pp. 1136–1137, 2012.

[106] J. Ekanayake and N. Jenkins, "Comparison of the response of doubly fed and fixed-speed induction generator wind turbines to changes in network frequency," *IEEE Transactions on Energy conversion*, vol. 19, no. 4, pp. 800–802, 2004.

[107] M. Rewienski and J. White, "A trajectory piecewise-linear approach to model order reduction and fast simulation of nonlinear circuits and micromachined devices," *IEEE Transactions on Computer-Aided Design of Integrated Circuits and Systems*, vol. 22, no. 2, pp. 155–170, 2003.

[108] D. Vasilyev, M. Rewienski, and J. White, "A TBR-based trajectory piecewise-linear algorithm for generating accurate low-order models for nonlinear analog circuits and mems," in *Proceedings of the 40th annual Design Automation Conference*, pp. 490–495, ACM, 2003.

[109] D. Vasilyev, M. Rewienski, and J. White, "Macromodel generation for biomems components using a stabilized balanced truncation plus trajectory piecewise-linear approach," *IEEE Transactions on Computer-Aided Design of Integrated Circuits and Systems*, vol. 25, no. 2, pp. 285–293, 2006.

[110] B. N. Bond and L. Daniel, "A piecewise-linear moment-matching approach to parameterized model-order reduction for highly nonlinear systems," *IEEE Transactions on Computer-Aided Design of Integrated Circuits and Systems*, vol. 26, no. 12, pp. 2116–2129, 2007.

[111] Y. Liu, W. Yuan, and H. Chang, "A global maximum error controller-based method for linearization point selection in trajectory piecewise-linear model order reduction," *IEEE Transactions on Computer-Aided Design of Integrated Circuits and Systems*, vol. 33, pp. 1100–1104, July 2014.

[112] S. A. Nahvi, M. Nabi, and S. Janardhanan, "Piece-wise quasi-linear approximation for nonlinear model reduction," *IEEE Transactions on Computer-Aided Design of Integrated Circuits and Systems*, vol. 32, pp. 2009–2013, Dec 2013.

[113] K. Zong, F. Yang, and X. Zeng, "A wavelet-collocation-based trajectory piecewise-linear algorithm for time-domain model-order reduction of nonlinear circuits," *IEEE Transactions on Circuits and Systems I: Regular Papers*, vol. 57, pp. 2981–2990, Nov 2010.

[114] H. R. Ali, L. Kunjumuhammed, B. C. Pal, A. Adamczyk, and K. Vershinin, "A trajectory piecewise-linear approach to nonlinear model order reduction of wind farms," *IEEE Transactions on Sustainable Energy*, pp. 1–1, 2019.

[115] L. Kaufman and P. J. Rousseeuw, *Finding groups in data: an introduction to cluster analysis*, vol. 344. John Wiley & Sons, 2009.

[116] G. H. Golub and C. F. Van Loan, *Matrix computations*, vol. 3. JHU press, 2012.

[117] P. Kundur, *Power system stability and control*, vol. 7.